The Imperial College of Science, Technology and Medicine
Department of Aeronautics

Enabling Technologies for Precise Aerial Manufacturing with Unmanned Aerial Vehicles

Pisak Chermprayong

Supervisor: **Dr Mirko Kovac**

This thesis is submitted for consideration for the degree of
Doctor of Philosophy, April 2019

Acknowledgements

First, I would like to start with my sponsor, the Royal Thai Government and Ministry of Science and Technology, who have provided my scholarship throughout A-level, Bachelors, Masters and PhD degree. I would like to thank only for the financial support they provided but also for many other things that they did to help me settle smoothly in the UK since 2009.

I would like to thank my supervisor, Dr Mirko Kovac, for his support and guidance since I have joined the lab as a summer internship student and carried on as a PhD student. His vision allows me to explore many exciting opportunities, in which I truly enjoy.

I would also like to thank to Talib Alhinai, Robert Siddall, Pooya Sareh, Ketao Zhang, Maxime Bouyssou, who participated with me on the two occasions of Drones for Good competitions in Dubai, UAE, especially to Talib Alhinai and his family, for being an excellent host during our first competition in 2016.

Contributing to a significant part of my time as a PhD student, I have pleasure working alongside many colleagues in Aerial ABM project, with special thanks go to Feng Xiao and Ketao Zhang, and achieving many great results. I have gained valuable experience, and Im grateful for that.

To Aerial Robotics Laboratory members, past and present, it has been a great fun with you all during my time here. I have enjoyed this wonderfully supportive community and wish the best for all of you.

For all other friends, here and elsewhere, thank you for making my experience enjoyable and for your support, with special thanks go to Natty, who helped me cope with my first year as a PhD student, and all of my flatmates, especially Shen, Maew and Yim, for their support during difficult times.

Finally, I would like to thank my parents. I would not be able to come this far without them.

Declaration

This thesis has not been submitted for any other degree other than this purpose. I declare that the contents in this thesis is my own work except parts that formed jointly-authored publications. My contributions and of those other authors to this work are stated below.

1. The work presented in chapter 2 was previously published in *IEEE Robotics & Automation Magazine* with the title "An Integrated Delta Manipulator for Aerial Repair: A New Aerial Robotic System" by Pisak Chermprayong (author of this thesis), Ketao Zhang, Feng Xiao, Mirko Kovac (who supervised this thesis). The concept of using a delta manipulator was conceived by Mirko Kovac and his students before I joined the lab, and early prototypes have been developed for simple manual motion control by a joystick. Ketao Zhang worked on mechanical design and manufacturing of the delta manipulator and the extrusion mechanism. Ketao Zhang and I worked together on material characteristics experiments. Feng and I worked together on modification and integration of the flight controller and trajectory generation. I worked on the self-aligning inverse kinematics of the delta manipulator, onboard electronics, AR-tag tracking, data processing, data visualisation and implementation of the delta manipulator and extrusion mechanism controller. Ketao Zhang, Feng Xiao and I worked together on flight tests and demonstrations. [1]

2. The work presented in chapter 3 was previously published in *Science Robotics* with the title "Rotorigami: A rotary origami protective system for robotic rotorcraft" by Pooya Sareh, Pisak

Chermprayong (author of this thesis), Marc Emmanuelli, Haris Nadeem and Mirko Kovac (who supervised this thesis). Pooya Sareh and Mirko Kovac conceived the concept of using an origami pattern as an aerial robot protection structure. Pooya worked on origami pattern design and analysis, with some contribution from Marc Emmanuelli. Pooya and I worked on the mechanical design of the protection ring. I worked on aerial platform selection, datalogging system, data processing and data visualisation. Pooya and I worked together on the experiments of this study, with minor contribution from Haris Nadeem during early stage experiments. [2, 3, 4]

3. The work presented in chapter 4 was previously published in *Journal of Field Robotics* with the title "Bioinspired design of a landing system with soft shock absorbers for autonomous aerial robots" by Ketao Zhang, Pisak Chermprayong (author of this thesis), Dimos Tzoumanikas, Wenbin Li, Marius Grimm, Mariusz Smentoch, Stefan Leutenegger, Mirko Kovac (who supervised this thesis). Mirko Kovac and Ketao Zhang have conceived the concept of this study. Ketao Zhang worked on the mechanical design and fabrication of the landing mechanism. Ketao Zhang also worked on FEA analysis with minor contribution from Mariusz Smentoch. I worked on aerial platform integration, datalogging system, actuator controller, data processing and data visualisation. Dimos Tzoumanikas, Wenbin Li, Marius Grimm, Stefan Leutenegger contributed into the flight controller algorithm. Ketao Zhang, Dimos Tzoumanikas, Wenbin Li, Marius Grimm and I contributed to the experiments of this study. [5]

4. The work presented in chapter 5 was previously published in *IEEE/RSJ International Conference on Intelligent Robots and Systems (IROS)* with the title "SpiderMAV: Perching and stabilizing micro aerial vehicles with bio-inspired tensile anchoring systems" by Ketao Zhang, Pisak Chermprayong (author of this thesis), Talib Alhinai, Robert Siddall and Mirko Kovac (who supervised this thesis). Mirko Kovac conceived the concept of this study. Ketao Zhang performed geometric and static analysis and fabricated the mechanical components of the module. I developed the controller of the actuation system, worked on aerial platform integration and processed the data. Ketao Zhang and I worked together on the experiments of this study. [6]

5. The work presented in chapter 6 is in the preparation stage for submission. This work is part of Aerial ABM EPSRC funded project, which has the following collaborators. Aerial Robotics Laboratory at Imperial College London, led by Mirko Kovac, focuses on aerial platform design, mechatronic system and precise aerial material deposition. University College London, led

by Vijay Pawar, Robert Stuart-Smith and Sebastian Kay, focuses on swarm control, multi-agent coordination and the planning algorithm. University of Bath, led by Chris Williams, Paul Shepherd, Richard Ball and Barrie Dams, focuses on material technology and structure design. Smart Robotics Lab at Imperial College London, led by Stefan Leutenegger, Wen Bin and Dimos Tzoumanikas, focuses on Model-Predictive-Controller (MPC) of the UAVs. Mirko Kovac conceived the idea of aerial additive manufacturing. I have developed and implemented the controller for the self-aligning delta manipulator and material extrusion mechanism. Ketao Zhang, Feng Xiao, Barrie Dams, Dimos Tzoumanikas and Sebastian Kay worked together on the experiments and demonstrations shown in this chapter.

Abstract

The construction industry is currently experiencing a revolution with automation techniques such as additive manufacturing and robot-enabled construction. Additive Manufacturing (AM) is a key technology that can offer productivity improvement in the construction industry by means of off-site prefabrication and on-site construction with automated systems. The key benefit is that building elements can be fabricated with less materials and higher design freedom compared to traditional manual methods.

Off-site prefabrication with AM has been investigated for some time already, but it has limitations in terms of logistical issues of components transportation and due to its lack of design flexibility on-site. On-site construction with automated systems, such as static gantry systems and mobile ground robots performing AM tasks, can offer additional benefits over off-site prefabrication, but it needs further research before it will become practical and economical. Ground-based automated construction systems also have the limitation that they cannot extend the construction envelope beyond their physical size. The solution of using aerial robots to liberate the process from the constrained construction envelope has been suggested, albeit with technological challenges including precision of operation, uncertainty in environmental interaction and energy efficiency.

This thesis investigates methods of precise manufacturing with aerial robots. In particular, this work focuses on stabilisation mechanisms and origami-based structural elements that allow aerial robots to operate in challenging environments. An integrated aerial self-aligning delta manipulator has been utilised to increase the positioning accuracy of the aerial robots, and a Material Extrusion (ME) process has been developed for Aerial Additive Manufacturing (AAM). A 28-layer tower has been additively manufactured by aerial robots to demonstrate the feasibility of AAM. Rotorigami and a bioinspired landing mechanism demonstrate their abilities to overcome uncertainty in environmental interaction with impact protection capabilities and improved robustness for UAV. Design principles using tensile anchoring methods have been explored, enabling low-power operation and explores possibility of low-power aerial stabilisation.

The results demonstrate that precise aerial manufacturing needs to consider not only just the robotic aspects, such as flight control algorithms and mechatronics, but also material behaviour and environmental interaction as factors for its success.

Dedication

To my parents.

Contents

List of Tables

List of Figures

Chapter 1

Introduction

1.1 Additive Manufacturing in The Construction Industry

The construction industry is a major drive of the world economy, though it still mainly relies on traditional fabrication methods that are energy intensive, slow and dangerous to operators [7]. In combination with a shortage of skilled workforce and wasteful fabrication methods, the growth of the construction industry and the global economy is being threatened.

Global average labour-productivity growth is also lacking behind, at about 1% over the past two decades compared to the global economy growth of 2.8%. Another interesting pattern is that, not all countries have positive labour-productivity growth. The United States, for example, have a negative growth when compared to the country's data from 1968 [8].

Advanced automation, new materials and digital technology have been proposed as possible productivity boosters among other ideas including, regulation improvement, better supply chain management and workforce re-skilling. One particular technology, additive manufacturing, has garnered interest from both industry and academia with its promising features that could enable construction processes to be more complex, more environmentally friendly, less labour intensive and cheaper when compared to traditional construction methods. The first promising feature is that it could produce difficult and complex geometries that would be cost-prohibitive for conventional methods [9, 10, 11]. It could also have a smaller impact on the environment by removing the need to use formwork in construction processes, which could also be cost-saving. With the bulk of labour-intensive tasks handed over to the automated construction workflow, labour related challenges in the construction industry, such as aging population that leads to scarcity of labour, decline in productivity and safety of on-site construction workers, could potentially be solved by increasing productivity with automated additive manufacturing. Better

efficiency will lead to cost saving construction processes and by combining all the potential benefits listed previously, additive manufacturing shows a promising way for kick-starting the construction industry into a new phase of growth.

We start with the definition of additive manufacturing. According to a jointly published document from the American Society for Testing and Materials (ASTM) and the International Organization for Standardization (ISO) [10, 12], additive manufacturing or AM process can be divided into 7 categories below.

1. Vat Photopolymerization (VP) is the process of selective curing, layer by layer, of photopolymer resin with UV light in a vat. The hardened part from curing process will form a structure that can be built upon.

2. Material Jetting (MJ) is the process of depositing (jetting) drops of material in a manner similar to typical inkjet printer. The jetted drops will be deposited on a build surface and solidified to form a structure.

3. Binder Jetting (BJ) is the process of depositing powder of materials onto a build surface and then adding liquid binding agent onto each layer to bind deposited powder together to form a structure.

4. Material Extrusion (ME) is the process of extruding materials through a nozzle onto a build surface. The most common ME process is Fuse Deposition Modelling (FDM) and it is trademarked by Stratasys. The method, which is a basis for most consumer grade 3D printers, will heat, extrude and deposit the materials, layer by layer. However, ME processes may not require heating on the extruded materials and achieve liquefy/solidify by other means.

5. Powder Bed Fusion (PBF) uses a laser or electron beam to melt and fuse a layer of powder of materials together to form a structure. Example processes in this category include Selective Laser Sintering (SLS) which uses a laser beam and requires a building chamber filled with inert gas like nitrogen and Electron Beam Melting (EBM) which relies on a high-energy electron beam to fuse powder of materials in a vacuum building chamber.

6. Sheet Lamination (SL) involves shaping and bonding sheets of materials to form a structure. SL-based manufacturing methods include Ultrasonic Additive Manufacturing (UAM) which uses ultrasonic welding to bond sheets of metal together and Laminated Object Manufacturing (LOM) which bonds sheets of paper with adhesive.

7. Direct Energy Deposition (DED) create a structure from focusing thermal energy not only on materials as they are being deposited but also on a substrates melting pool. Thermal energy sources usually come from a laser or electron beam. Example processes are Laser Engineered Net Shaping (LENS) and Electron Beam Freeform Fabrication (EBF). LENS utilises a laser beam and an inert gas building chamber, and EBF utilises an electron beam with a vacuum

building chamber. Another promising DED-based method is from MX3D which utilises an arc welding technique to print extruding metallic structures into the air without the need of additional support structures [13].

There is a variety of pioneering works which utilise AM technologies in the construction industry with different materials and different AM processes, which are summarised in Table 1.1 below.

System Name	Developer	AM process	Materials	Material Delivery System	Mobiliy	Off/On-site
Contour Crafting	University of Southern California	ME	Concrete	Gantry	Static	Off-site
Concrete Printing	Loughborough University	ME	Concrete	Gantry	Static	Off-site
D-shape	D-Shape Enterprises L.L.C.	BJ	Concrete	Gantry	Static	On-site
Apis Cor	Apis Cor	ME	Concrete	Apis Cor robotic arm	Mobile	On-site
Winsun	Winsun	ME	Concrete	Gantry	Static	Off-site
TotalKustom	TotalKustom	ME	Concrete	Gantry	Static	On-site
3DCP	Eindhoven University of technology	ME	Concrete	Gantry	Static	Off-site
XtreeE	XtreeE	ME	Concrete	Industrial robotic arm	Static	Off-site
BAAM	Oak Ridge National Laboratory	ME	Thermoplastic	Gantry	Static	Off-site
Qingdao Unique Products Develop	Qingdao Unique Products Develop	ME	Concrete	Gantry	Static	On-site
KamerMaker	3D Print Canal House	ME	Thermoplastic	Gantry	Static	Off-site
FreeFAB™ WAX	Engineering Excellence Group Sydney	ME	Wax	Gantry	Static	On-site
Cybe	CyBE Construction	ME	Concrete	Industrial robotic arm	Mobile	On-site
WASP	WASP	ME	Concrete	Crane, Delta robot	Static	On-site
MX3D	MX3D	DED	Stainless steel	Industrial robotic arm	Mobile	Off-site
MiniBuilders	The Institute for Advanced Architecture of Catalonia	ME	Concrete	Mobile ground robots	Mobile	On-site
Team of mobile robots	Singapore Centre for 3D Printing	ME	Concrete	Multiagent mobile ground robots	Mobile	On-site
DCP	MIT Media Lab, Massachusetts Institute of Technology	ME	Polyurethane foam	Mobile platform with compound arm system	Mobile	On-site

Table 1.1: Summary of existing works in additive manufacturing for the construction industry [14, 9, 15, 16, 17, 18, 19, 20, 21, 22, 23, 24, 25, 13, 26, 27, 7]

A significant number systems listed in Table 1.1 can be considered as off-site manufacturing. This is because many AM processes are developed mainly for controlled environments and can mostly perform small-scale manufacturing. Currently, off-site prefabricated components have been the norm and the construction industry has already benefited from processes like precast concrete block in off-site and controlled fabrication environment [7].

One particular combination, ME process and cementitious materials (aggregate-based materials), has emerged as a favourite among other choices. The reasoning behind this is quite clear: traditional construction material is concrete (cement plus aggregate) and the extra amount of research needed to develop materials that have good buildability and are also suitable for AM processes may be less than inventing new construction materials from scratch. Depositing cementitious materials does not require a complex build environment/chamber or special treatment from chemical agents, which can make the process complex and cost-prohibitive.

One notable example of off-site AM with cementitious materials has been developed by company Winsun [17] which 3D printed concrete components off-site and then assembled them on-site.

Even though off-site prefabrication, including off-site AM, benefits from a highly controlled fabrication environment that may lead to higher quality outputs, it does have limitations in component transportation, assembly process and limited on-site customisability [7]. Unlike raw materials, moving prefabricated parts to building sites may require higher volumetric transport and creates increased road congestion [7]. For structures being built in remote or hard to access locations, information regarding local environments may be limited or even incorrect, leading to problems such as limited abilities to plan the construction [7] and incorporate last-minute design changes [Camacho]. With on-site AM, worker safety and process control can be improved and last-minute design changes will also be possible [7]. Recent works on AM in the construction industry agree that to fully benefit from AM technology, on-site AM techniques need to be further developed [Keating, Camacho, Zhang]

Existing works that explore the use of on-site AM techniques include Apis Cor [25], D-shape [15], TotalKustom [18] and Qingdao Unique Products Develop [17], with the first two utilising static delta manipulator platforms and the last three using large gantry systems for 3D printing with cementitious materials.

Another approach for on-site AM is 3D printing of construction formwork. The concept has been demonstrated by FreeFAB^{TM} WAX [23], which utilises a gantry system with 3D printable wax and DCP [7] which utilises a mobile platform combined with compound arm system with 2-part polyurethane foam.

Compared to mobile material delivery platforms, static systems will generally be simpler and easier to operate [7], but their construction envelopes will be bounded to the size of their fixed workspaces. With its mobility, mobile platforms will enable scalability but potentially at a cost of increased complexity.

All of existing works on mobile material delivery system in AM are ground-based systems [7, 27, 24, 26] that aim to extend construction envelop in lateral direction, however, their coverage along the vertical direction is still limited.

Aerial robots have potential to extend construction envelopes beyond current capabilities of ground-based systems. Research community has been exploring the use of aerial-based systems for various construction-related applications, including tensile structure building with Unmanned Aerial Vehicles (UAVs) [28] and brick laying with UAVs [29], though the research is still in its infancy and far from being utilised in actual construction works. One work introduced a concept of using UAV for aerial 3D printing, which can be considered as Aerial Additive Manufacturing (AAM), with 2-part expanding polyurethane foam [30], but there are multiple challenges that need solving in order to realise AAM.

Unlike ground robots, typical multirotor UAVs are underactuated and do not have full controllability in all available degree of freedoms. In other word, it cannot follow arbitrary trajectories

in 3-dimensional space, hence require relatively complicated controllers. Another challenge related to the control aspect of UAVs is localisation because accurate information of positions of the robot is required for successful navigation. Most commercial UAVs rely on GPS for absolute position estimate, however, accuracy of GPS can vary from 10 metres in typical consumer-grade GPS systems to an a few centimetres in RTK-GPS [31]. A localisation accuracy of few centimetres on the surface of the earth may already be an incredible feat, but for AAM to be achievable a much more precise source of position estimate is required. Even if the accuracy of GPS is significantly improved, there will be outages of GPS signals in GPS-denied environments. There are alternatives, including, but not limited to, external motion capture systems, ultra-wideband (UWB) and visual-inertial sensors, which we will discuss later in this thesis.

One major disadvantages of UAVs is that they require constant propulsion, and hence constantly use significant amount of energy to stay aloft in the air. The heavier the payload of the UAVs, the more power is required to maintain the necessary thrust. This limits operational time of UAVs and requires frequent batteries recharging.

Multirotor UAVs are inherently unsafe with their fast spinning propellers, not only to themselves, if these propellers hit something and crash the UAVs, but also to their surroundings. Especially when operating in harsh conditions, on a windy offshore oil rig for example, serious accidents could occur if relevant safety issues are unattended.

Strictly speaking, Unmanned Aerial Vehicles normally refers to two types of systems: unmanned fixed wing system and unmanned multirotor system. This thesis will focus only on unmanned multirotor systems and the term UAVs will refer to this.

Apart from using AM in construction processes, another potential important benefit is that it could be used for in-situ repair [10]. A framework that autonomously scan buildings, detect repair-needed areas and carry on repair tasks with AM has been suggested. However, no research has attempted to combine both AM and automation for repair tasks in construction yet [10].

1.2 Challenges for Aerial Additive Manufacturing

Four common research themes [32] required for technological enablers of AAM can be categorised as the following.

1. Methods, mechanisms and materials: Physical implementations of AAM are required to demonstrate its feasibility beyond theoretical speculation. Manufacturing methods, robotic platforms and suitable materials must be developed, characterised and evaluated.

2. Structure and design: This theme includes structure design and specification, life cycle management and architectural applications possible with AAM.

3. Planning: Effective planning and coordination of manufacturing processes and construction agents are required for AAM to be successful.

4. Metrics: Common benchmarks for performance evaluation are required for quantitative analysis of robotic systems in construction applications, though with a wide range of systems and applications, these benchmarks are not straightforward to define.

Inspired by the research themes above, various challenges involved in realising AAM are characterised into two categories by the author: primary challenges dealing with direct technological enablers for AAM and secondary challenges dealing with technological enhancers for aerial robots in AM applications and beyond.

Primary challenges

1. Precise material deposition with UAVs: Like normal additive manufacturing, the material must be processed and delivered to desired locations, as precise as the application requirements, which can depend on the types of material used and geometry of the structures. The actual implementation of AAM system must satisfy these accuracy requirements.

2. Materials technology: Performance criteria for AAM materials must be determined and suitable materials must be developed according to the applications.

3. High-level planning and coordination: Algorithms must be designed to effectively control AAM processes and behaviour of agents.

4. Structure design: Suitable structures must be designed and evaluated not only in just theoretical study but also in practical implementation with AAM system.

Secondary challenges

1. Limited operation time: Apart from an obvious long-term solution but difficult to achieve of simply making a breakthrough in energy technology for UAV, maximising UAV operation time with current battery technology can be potential short-term solutions.

2. Ability to navigate within complex environments: What can be improved from commercial rigid protection frames already available? What factors matter when designing protection strategies?

This thesis is part of Aerial Additive Building Manufacturing (Aerial ABM), which is a UK EPSRC funded research focusing on an aerial robotic construction system with multiple project collaborators. Primary challenges 2, 3 and 4, are responsible by other project collaborators, and

they are not main focuses of this thesis. Only primary challenge 1 and all secondary challenges will be discussed in detail.

1.3 Outline of this thesis

Responding to these challenges, this PhD thesis explores solutions that could be exploited in a quest to realise AAM and beyond. Chapter 2 shows a first step towards AAM with an integrated delta manipulator for aerial material deposition, with a case study of aerial repair with monolithic construction and repair materials. The main concept in this chapter is on the design and control of aerial delta manipulator that add extra degree-of-freedoms to compensate for positional errors that arise from UAV's deviation from its desired setpoint. Chapter 3 and 4 explore two novel concepts aiming to improve robustness of UAV, the first being a lightweight rotary origami-based protective system, Rotorigami, that improves navigation in cluttered environments and the second being a bio-inspired adaptive landing system for UAV that enables dynamic landing in various structures, weather conditions and impact speeds. Chapter 5 discusses an investigation of UAV operational time extension with bio-inspired tensile anchoring system: SpiderMAV. The prototypes demonstrate low-power perching mode and stabilising mode and could also potentially enable a flight-tensile hybrid locomotion. Chapter six addresses the primary challenge of precise aerial deposition for AAM with cementitious materials and other primary challenges pursued by Aerial ABM project collaborators. The last chapter describes overall achievements and discusses what would be further steps required for advancing AAM technologies.

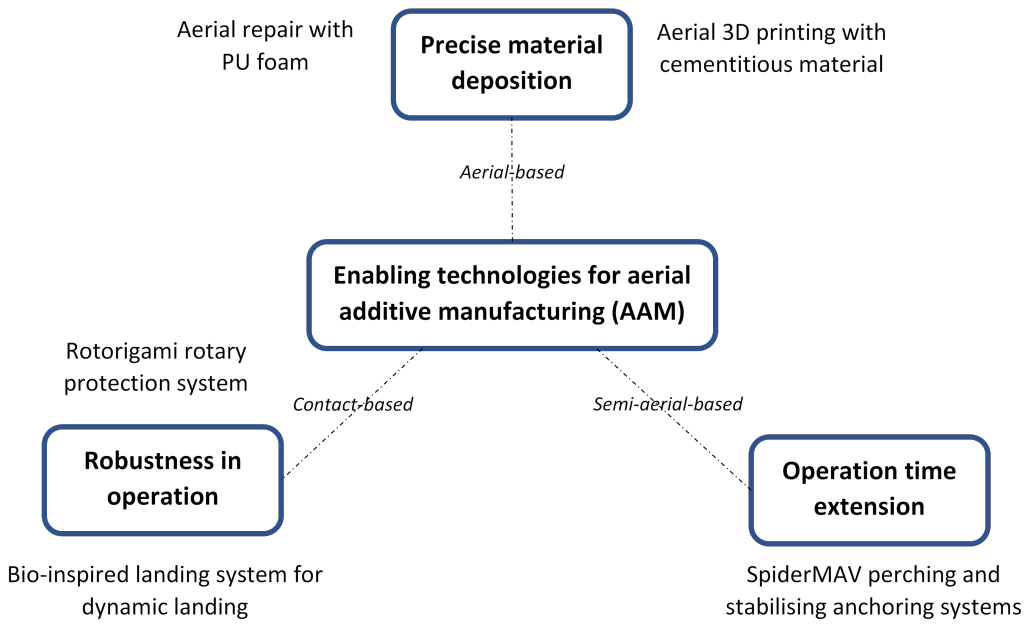

Figure 1.1: Solutions towards technological challenges for aerial additive manufacturing

Chapter 2

AAM: Aerial Repair with An Integrated Aerial Delta Manipulator

2.1 Introduction

The work in this chapter was previously published in *IEEE Robotics & Automation Magazine* with the title "An Integrated Delta Manipulator for Aerial Repair: A New Aerial Robotic System" [1]

Unlike ground robots[33], multirotor UAVs are still very limited in their ability to hold their spacial position precisely in windy conditions or close to infrastructure elements. This dramatically limits their usability in applications such as aerial manipulation and aerial repair. In order to expand the current capabilities of multirotor UAVs to applications that require precise aerial station-holding, these issues must be addressed. An on-going research theme is to equip flying agents with additional degrees of freedom by integrating robotic manipulators [34, 35, 36, 37].

Given the limited payload of most aerial robots, particularly multirotor UAVs, low-complexity and light-weight grippers were developed for grasping [38, 39, 40], perching and transporting payloads [41]. Due to the low-complexity of these grippers, a relatively simple control system can be effective for manipulator control. Since the grippers in these examples are mounted directly onto the UAVs , they cannot compensate for undesired movement of the aerial platform. UAVs therefore require extremely precise flight control for accurate operations.

In comparison to rigid connections, adding a serial manipulator between the gripper and the UAV platform allows the gripper to be controllable and relatively flexible [42, 43, 44]. However, the position and orientation of each joint on the aerial-serial link cause substantial disturbance to the dynamics of the UAV due to the out-of-balance masses.

In contrast to the serial manipulators, parallel manipulators in general have a high power-to-weight ratio and can drive the end-effector at high velocity and acceleration [45, 46]. Errors in the joint positioning of this type of manipulator become averaged rather than accumulated in serial manipulator cases. This type of manipulator therefore can yield better accuracy than serial manipulators [47]. Furthermore, the actuators for a parallel robot are fixed at its base, which can be mounted directly on the UAV frame, reducing disturbance to the dynamics of the UAV.

An integrated parallel manipulator can enable new applications for UAVs, such as aerial object manipulation [48] and aerial repair [49, 30].

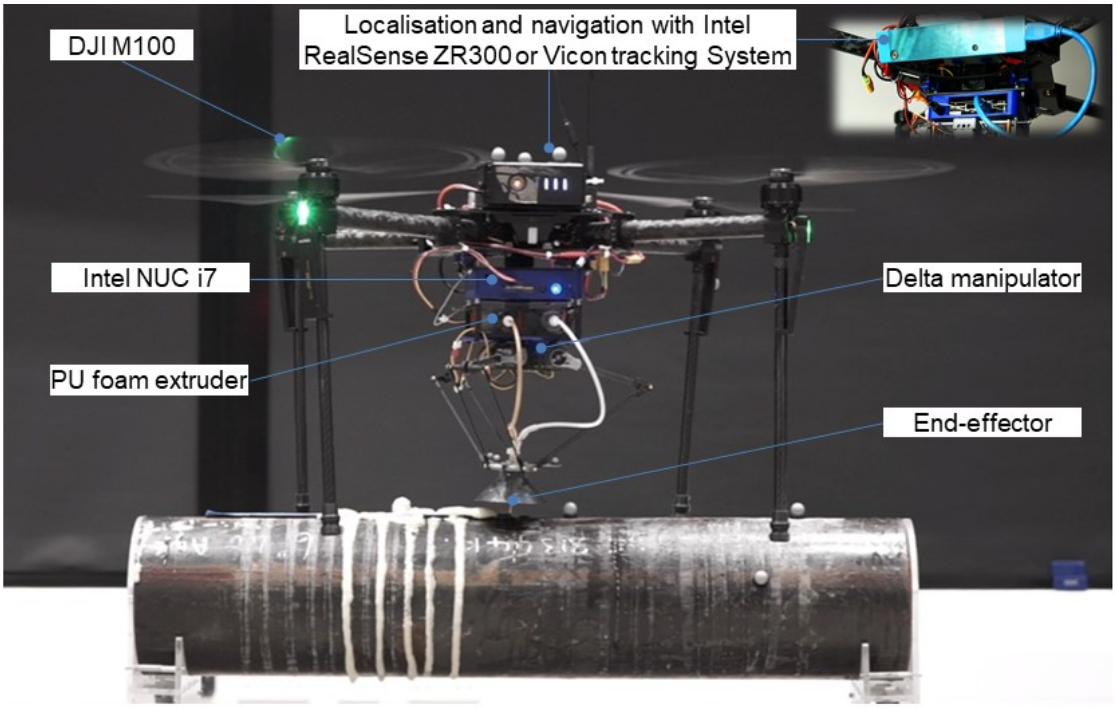

Figure 2.1: [1] The autonomous aerial robot with onboard Intel RealSense VI sensor, Intel NUC i7 processor and integrated Delta manipulator for aerial repair tasks.

Focusing on the implementation of high-precision tasks for parallel manipulators in real-world application for aerial repair, this paper presents a new aerial robotic system that integrates a Delta manipulator [50, 51] and a quadrotor UAV (Fig.6.12).

In this work, we propose a control architecture for the integrated aerial robotic system and verify the control algorithm to be effective for autonomous aerial repair. We quantitatively analyse the controller performance with experimental results obtained using a motion capture system for ground truthing, showing that the proposed aerial robot is capable of performing high-precision operations with the integrated Delta manipulator and extrusion system. The contributions of this paper are the following:

1. To the best of our knowledge, this work presents the first aerial robot capable of depositing liquid expansion foam using a high-precision and light-weight 3-DOF Delta manipulator for aerial repair work.

2. Characterisation of the end-effector accuracy and the improvement that is achieved by compensating the quadrotor fluctuations with the Delta arm manipulator.

3. Development of a light-weight extrusion system for extrusion of liquid expansion foam for aerial repair.

4. A demonstration of aerial pipeline repair using visual-inertial (VI) odometry-aided navigation.

2.2 System description

2.2.1 The Matrice 100 platform

In this work we use DJI Matrice 100 (M100) as the quadrotor platform. It has a kerb weight of 2.431 kg with a TB48D battery, a maximum take-off weight of 3.6 kg, a diagonal wheelbase of 650 mm and a hovering time of 16 minutes with 1kg payload when the TB48D battery is in use. This allows for 1.169 kg of payload before the UAV reaches its maximum take-off weight. The detailed specs and CAD model of the M100 quadrotor is documented and available from the official website.

2.2.2 The Delta manipulator

The employed Delta manipulator, which is capable of 3-DOF pure translational motion, is one of the most used parallel robot in production. The parallel robot has three identical limbs, as seen in Fig. 2.2, and employs only revolute joints. The revolute joints connecting the three limbs to the base and platform are located at B_i and D_i (i = 1, 2 and 3),which are vertices of the two virtual equilateral triangles and define the geometrical parameters of the base and platform respectively. Each limb contains an upper arm B_iC_i and a lower parallelogram 4R linkage C_iD_i.

The base and platform are defined by the circumradius R and r of the virtual equilateral triangles $\triangle B_1B_2B_3$ and $\triangle D_1D_2D_3$. The design parameters for the upper and lower arms are denoted by L and l as illustrated in Fig. 2.2.

The three revolute joints connected to the base at points B_i are actuated by three servos, and the angular inputs θ_i are measured from the base plane to the upper arm B_iC_i.

A coordinate frame $\{A\}$ for the Delta manipulator is set with its origin A attached to the geometric centre of the base. The x_A- and z_A-axis are located in the base plane with z_A-axis parallel to line B_2B_3, Whilst y_A-axis is perpendicular to the base plane and forms a right-handed coordinate frame.

Forward kinematics

The forward kinematics of the Delta manipulator can be solved using a geometrical method [52]. As the base and end-effector always remain in the same orientation, it only allows the end-effector to move in translational motion. The point C_i of each limb traces an virtual sphere with the centre located at D_i and radius l. By offsetting these spheres towards the centre of

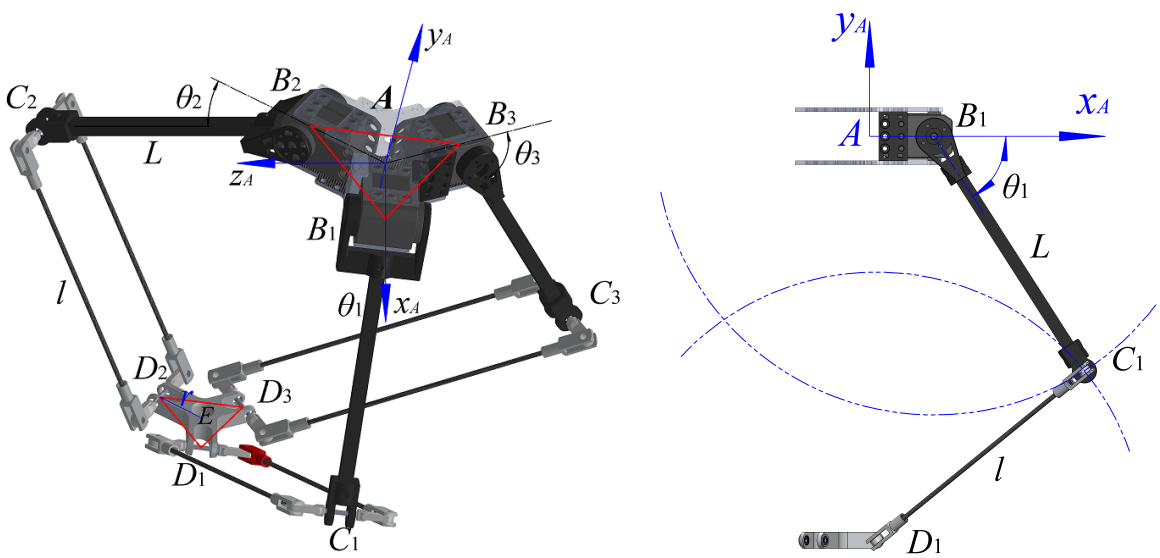

Figure 2.2: [1] 3D model of the Delta manipulator employs purely revolute joints.

the manipulator, in the same plane that is defined by its upper and lower limb, we get three spheres at known centres and known radii. The intersection point, $E_0(x_t, y_t, z_t)$, can be found by solving three intersecting quadratic sphere equations given by

$$(x_t - x_i)^2 + (y_t - y_i)^2 + (z_t - z_i)^2 = l^2 \tag{2.1}$$

where i = 1,2,3 and (x_i,y_i,z_i) is the centre of ith sphere and l is the length of the lower arm, parallelogram 4R linage.

If all these spheres intersect tangentially, it yields one solution. However, it will not yield any solutions if these spheres do not intersect. Geometrically, a system of three intersecting spheres can yield two solutions. From the fact that the Delta manipulator in Fig. 2.2 always has its end-effector positioned below its base, solutions that give the end effector position above its base are eliminated.

Inverse kinematics

The inverse kinematics of the Delta manipulator is to derive the angular inputs θ_i from the position of a given configuration of the end-effector. In each limb of the Delta manipulator, the parallelogram 4R linkage together with the two revolute joints at point C_i and D_i are equivalent to a UU chain. It implies that point C_i is moving on a sphere with the centre D_i and radius l as illustrated in Fig. 2.2(b). Taking this geometric property of the Delta manipulator, a geometric method [53] is used for solving the inverse kinematics. The angular input θ_1 required to configure the end-effector to a given position vector $E_0 = [x_t, y_t, z_t]^T$ is calculated by

$$\theta_1 = arctan(z_{c1})/(y_{b1} - y_{c1}) \tag{2.2}$$

in which z_{c1}, y_{b1} and z_{b1} are the elements of the position vector of points B_1 and C_1 in the reference frame $A - x_1 y_1 z_1$ and can be derived by solving

$$z_{c1}{}^2 = L^2 - (y_{c1} + R)^2 \tag{2.3}$$

and

$$l^2 - x_0{}^2 = (y_{c1} - (y_0 - r))^2 + (z_{c1} - z_0)^2 \tag{2.4}$$

The other two angular inputs θ_2 and θ_3 can also be calculated independently with the same method as above.

Reachable and executed workspace

With the solution for kinematics as outlined above, the reachable workspace of the Delta manipulator is analysed with the design parameters then determined by enabling the Delta manipulator to compensate for the fluctuation of the aerial platform, with DJI M100 employed in this work.

Given the errors between the reference and actual trajectory of the DJI M100 during autonomous flight reported in [54], the reachable workspaces with various values for design parameters are analysed and compared to the trajectory fluctuations of M100 and the selected values for these parameters of $R = 37$ mm, $r = 20.5$ mm, $L = 101.5$ mm and $l = 150.5$ mm. With these values selected for the design parameters, Fig. 2.3 illustrates both the reachable workspace computed for forward kinematics and executable workspace to compensate the UAV's fluctuation.

Inverse kinematics-based method for compensating the UAV's fluctuations

As illustrated in Fig. 6.12, the Delta arm base is fixed to the floating UAV frame while the end-effector is capable of 3-DOF translational motion with respect to the UAV frame. A simplified schematic model of the system is illustrated in Fig.2.4. The body frame $\{O\}$ of the aerial robot is attached at the geometric center of the UAV with X-axis pointing in the forward direction of the UAV, the Z-axis is perpendicular to the UAV frame and Y-axis points to the left-hand slide to form a right-handed frame. The local frame $\{A\}$ of Delta manipulator is parallel to the

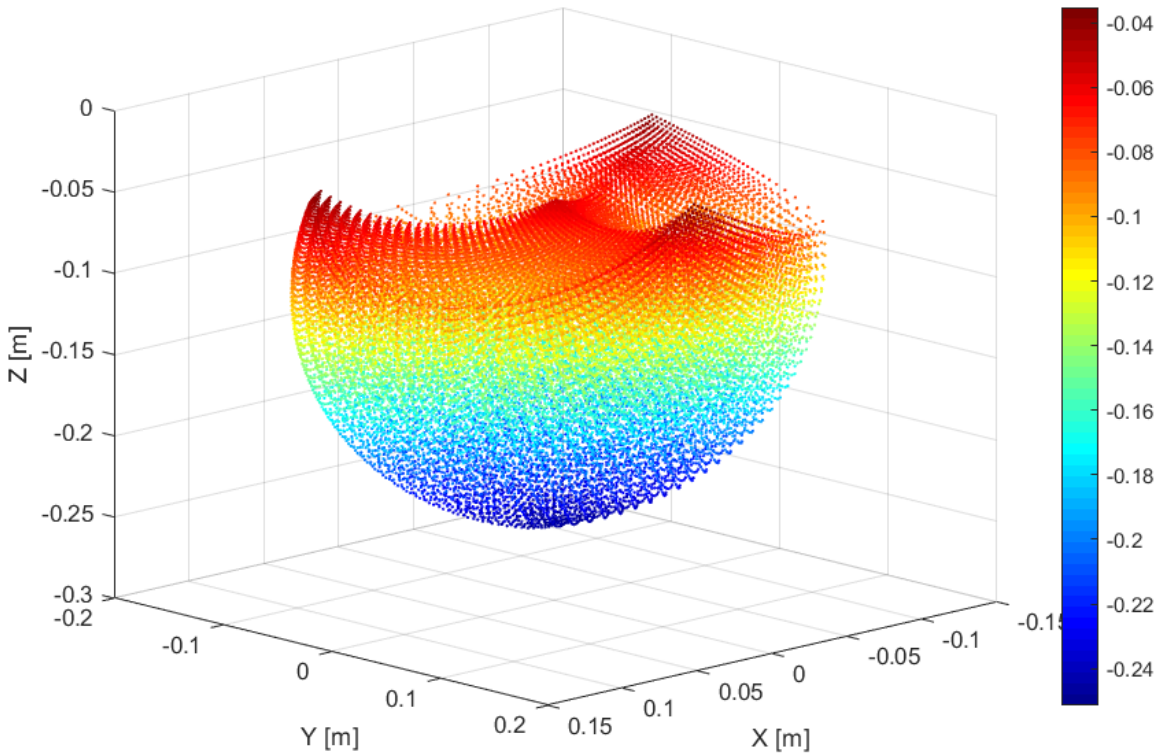

Figure 2.3: [1] Reachable workspace of the Delta manipulator. The colour-bar shows distances in Z-axis between the base of the Delta manipulator to reachable end effector location.

body frame $\{O\}$ with its origin attached at the center A of Delta manipulator base. The offset between the two centres O and A is denoted by b. At the other end of the Delta manipulator, the end-effector with centre T is directly mounted underneath the moving platform of Delta manipulator and the distance between centres E and T is denoted by f.

With the coordinate systems in Fig. 2.4, a unit-vector quaternion representing rotation from world frame $\{W\}$ to the body frame $\{O\}$ of the UAV is given by $\mathbf{Q}_O = [w_o, x_o, y_o, z_o]^T = [1, 0, 0, 0]^T$, in which w_o is the real part and x_o, y_o and z_o are the vector part of the quaternion.

In order to position the centre T precisely at a target point, the optimized solution is to hover the UAV directly above the target point so that ET is vertically aligned with Z-axis.

However, a flying UAV in real world scenarios is a floating platform with both translation and orientation offsets from the optimized solution. In such cases, the moving platform of the Delta manipulator has to move correspondingly with respect to the body frame $\{O\}$ to allow the the centre T of the end-effector to be at the target point, thereby compensating the offset of the UAV platform.

When the UAV platform drifts to the position at O' (Fig.2.4) with a purely translation offset, the position vector of centre A in the frame $\{O'\}$ is expressed as $\overline{O'A'} = [0, 0, -b]$. With further

orientation offset of the UAV frame at position O', centre A moves to point A''. The new position vector $\overline{O'A''}$ is calculated as

$$\overline{O'A''} = \mathbf{Q}_{O'}\ \overline{O'A'}\ \overline{\mathbf{Q}}_{O'} \tag{2.5}$$

where $\overline{\mathbf{Q}}_{O'}$ is a conjugate of quaternion $\mathbf{Q}_{O'}$.

Given the capability of the pure translation of the moving platform with respect to the base of the Delta manipulator, it derives

$$\overline{E''T} = \mathbf{Q}_{O'}\ \overline{ET}\ \overline{\mathbf{Q}}_{O'}. \tag{2.6}$$

Thus, the vector $\overline{A''E''}$ is calculated as

$$\overline{A''E''} = \overline{A''O'} + \overline{O'O} + \overline{OF} + \overline{FT} + \overline{TE'} \tag{2.7}$$

in which $\overline{OO'}$ is the position vector of the UAV and $\overline{OF}$ is the position vector of the material deposition target, in respect to the global coordinate frame $\{O\}$.

In order to control the motion of the moving platform in respect to the base of the Delta manipulator, the position vector $\overline{A''E''}$ has to be expressed in its local frame at position A'', which can be calculated as

$$\overline{A''E''}_{A''} = \overline{\mathbf{Q}}_{O'}\ \overline{A''E''}\ \mathbf{Q}_{O'} \tag{2.8}$$

By using the kinematics solver and the position vector $\overline{A''E''}$ as derived above, the required input angles of the servos for the Delta manipulator can be computed. These computed servo angles are used to control the servos of the Delta manipulator such that its end-effector are positioned at the target point to compensate for the UAV's offset.

This is a novel approach to compensating the UAV's offset in flight by using the advantages of a dexterous Delta manipulator.

2.2.3 The extrusion mechanism for material deposition

LD40 is a general-purpose two component PU form used in a wide range of applications. In light of properties of the material (LD40), it was adopted for this application due to its expansion ratio of approx 20 times to it original volume. This relatively large volume change

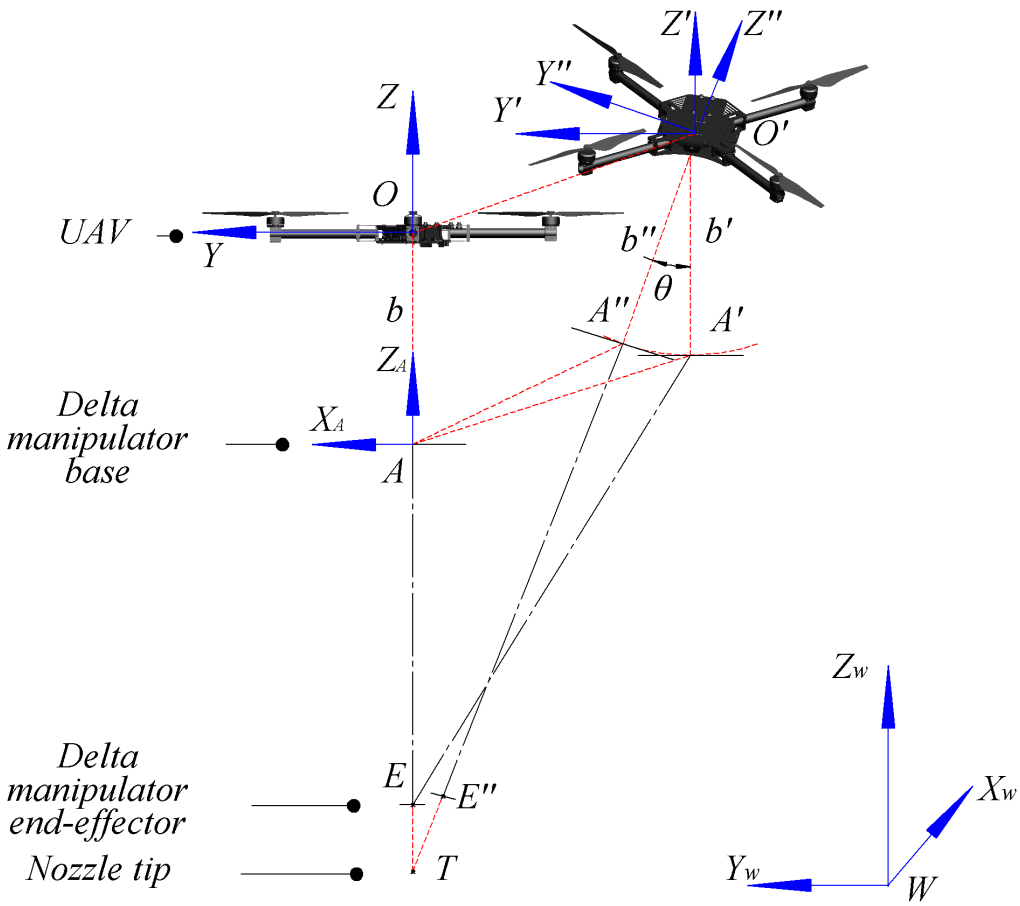

Figure 2.4: [1] The schematic drawing of the method for compensating UAV fluctuation using the integrated Delta manipulator.

is advantageous for sealing purposes because the expansion can alleviate potential imprecision in the application process.

The extrusion mechanism consists of two 20 ml syringes for storing the two-part liquid components, a 3D printed mounting frame and laser machined spur gears for the power transmission. The syringes are modified by fixing the rubber plunger to the front tip of a lead-screw running through the centre of the syringe. The lead-screw is fixed with a captive nut embedded in the spur gear. The Dynamixel servo XL320 is selected for driving the spur gear train that will extrude the two components of the foam with the lead screw motion transmission mechanism.

An epoxy mixer nozzle, with 15 acetal mixing elements and a total of 2.86 ml volume, is connected to two flexible tubes with a Y-junction as shown in Fig. 2.5. A 3D printed conical wind shield is attached to the mixer nozzle to prevent the downwash wind affecting the foam flow.

A control algorithm is then implemented to extrude materials and estimate the flow rate based on the angular velocity of the servo. By reversing the rotating direction of the servo, it allows the mechanism to refill the syringes with liquid PU foam material.

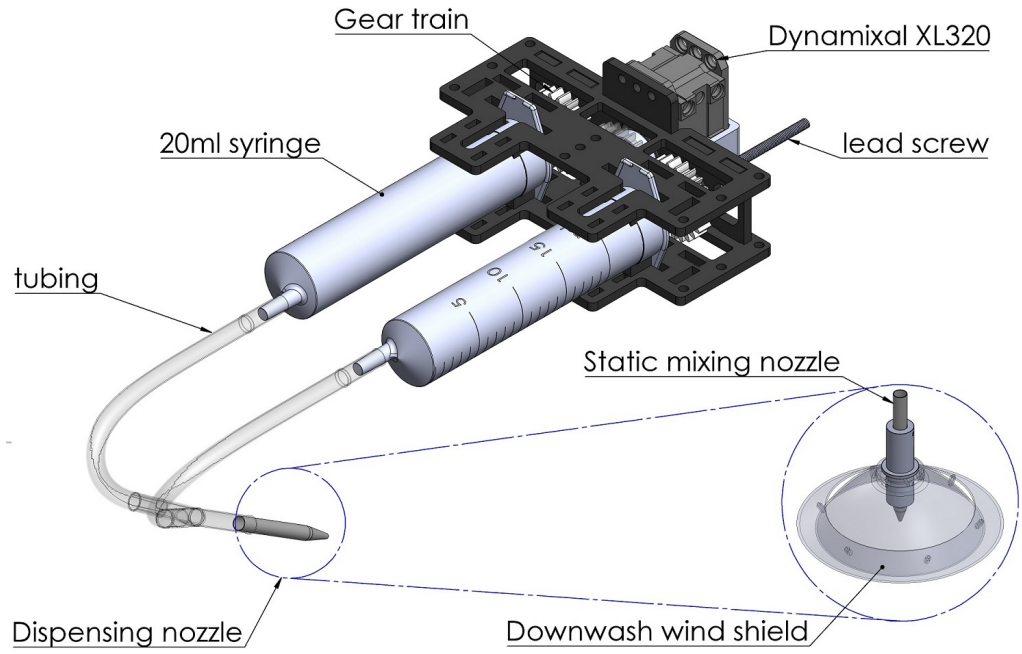

Figure 2.5: [1] The repairing kit with two-part PU foam material extruder and a static mixing nozzle.

2.3 Control architecture

2.3.1 M100 control system

The Robot Operating System (ROS) has been chosen as our robotic middlware framework due to its widespread adoption in the robotics community, the features available and its ease of use. All of the packages mentioned below are either open-source ROS packages or implemented in ROS by us.

In terms of programming and controlling the UAV (DJI M100), DJI offers an open source software library called the DJI onboard SDK that allows users to communicate with its flight controller. In addition to this, we implemented a Model Predictive Controller(MPC) package from [54] to enable high-precision position control of the quadrotor UAV. A Multi Sensor Fusion(MSF) package from [55] has been used for the state estimation of the quadrotor UAV. This can follow position updates as input from either the motion capture system or the robot onboard VI odometry[56], outputing the position, orientation, velocity, angular velocity and linear and angular acceleration of the quadotor UAV that the MPC needs.

The motion capture system can generate a fixed inertial frame so that a fixed pose(position and orientation) setpoint can be used as the reference for the MPC position controller. However, when using VI odometry, the inertial frame shifts over time due to the lack of an online loop closure so that when a fixed setpoint is published to MPC, the quadrotor UAV still drifts

slightly in its ground truth. To improve this, we used ARTag, which is a fiduciary marker system that supports augmented reality. An ARTag tracker package[57] is integrated to keep updating the ARTag position and orientation within the inertial frame. A trajectory publisher package is additionally implemented to update the pose setpoints that keep a constant position vector to the ARTag, enabling the ARTag to act as an anchor to stop the drift of M100.

2.3.2 Delta manipulator control system

The control flow diagram of the aerial robot with integrated Delta manipulator is illustrated in Fig. 2.6. Two ROS nodes have been programmed; (*i*) for inverse kinematic computation for the light-weight Delta manipulator as described in section II-B and (*ii*) for transmitting/receiving data packets with servo motors used in the joints of the Delta manipulator. We have implemented a modified Dynamixel SDK software system based on [58] to serve this purpose. To compensate for the UAV's offset from a desired trajectory, the real-time pose of the UAV, either from external motion capture system or VI odometry, and its trajectory command references are feed into ROS node for inverse kinematics computation. The controller for the Delta manipulator is running alongside the MPC controller for the UAV.

2.3.3 Extrusion mechanism control system

In the extrusion system, an actuator is implemented to control the extrusion speed. The chosen motor (Dynamixel XL320) is a lightweight smart servo that has the suitable features and characteristics to perform as a joint in the Delta manipulator. However, it does not have a speed controller feature directly available. A closed-loop PID speed controller based on the encoder position data has been developed to resolve this issue.

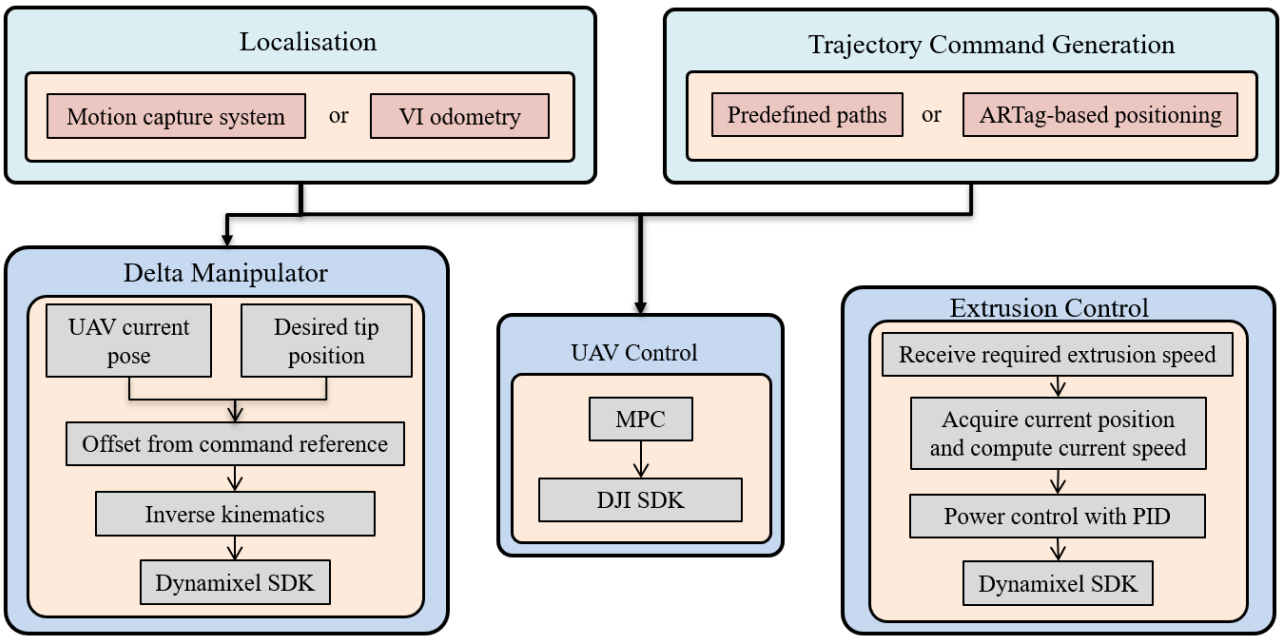

Figure 2.6: [1] Control diagram for the complete aerial robot with integrated Delta manipulator, material extrusion mechanism and VI sensor.

2.4 Prototypes and experimental validation for enhanced stability

2.4.1 Hardware setup

A DJI M100 quadrotor platform is used carrying a Intel®NUC7i7BNH (Intel®Core^{TM}i7-7567U Processor, 16GB RAM and 250GB SSD) running Ubuntu 16.04 and ROS Kinetic. The robot also carries the repair kit and the custom-made Delta manipulator. The total mass of the system including liquid repair material is 3.5 kg with the masses of individual components listed in Table 2.1. A Vicon motion capture system was used to provide 6-DOF pose feedback at 100 Hz for objects of interest within the flight arena. The PU foam extrusion system is controlled using 2.4 GHz RC link. Dynamixel XL320 smart servo has been chosen as the joints in the Delta manipulator due to its light weight at 16.7g each, its reliable digital communication rather than traditional PWM signal, the ease of its wiring in its ability to be connected within a daisy chain, and the PID tune-able position control mode. XL320 has also been used as the actuator for the extrusion mechanism and linked up to the daisy chain with servo motors in the Delta manipulator. Internal Dynamixel servo parameters have been fine-tuned to suit our applications.

Table 2.1: [1] Weight of each onboard components

Components	Weight [g]	Percent
DJI M100 quadrotor (with battery)	2350	67.1
Repair kit (without material)	250	7.1
Inter NUC	300	8.6
Intel Realsence ZR300	80	2.3
Delta manipulator module	220	6.3
Liquid expansion foam	35	1.0
Other accessories	235	6.7
Total	3500	100

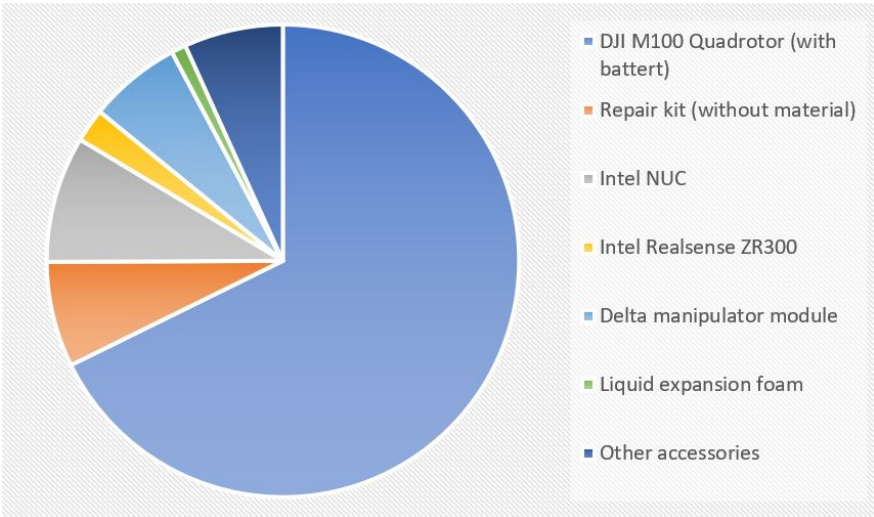

2.4.2 Material deposition accuracy

As a criteria, we aim to be able to perform aerial repair work with certain end-effector positioning accuracy in the X-axis, Y-axis and Z-axis. A maximum allowable fluctuation of 20 mm is chosen to be the end-effector positioning accuracy criteria in the Z-axis. If this criteria has not been met, it could result in the end-effector disrupting repair work surfaces and ineffectiveness in using the downwash windshield to protect the foam deposition process from the downwash of the UAV's rotors.

Positioning in X-axis and Y-axis will benefit from improved accuracy; however, the required accuracy will depend on the size of the damaged area. Regardless of this, improving its accuracy means that the required LD40 PU foam volume will be minimised and will only be deposited in the vicinity of the area of interest. The LD40 PU foam has an large volume expansion ratio. With a mixture capable of 20 time expansion ratio, 0.02 ml of the mixture will generate a half sphere model with a radius of about 5.7mm, which is close to average size of single expanded foam droplet from empirical tests. This number will be used as a guideline for our X-axis and Y-axis root-mean-square-error (RMSE) accuracy evaluation in order to characterise whether or not the aerial material deposition can perform reliably at a given task.

Table 2.2: [1] Performance of the aerial robot in Vicon spot hovering

	RMSE (mm)		Reduction (%)	Max Fluctuation (mm)		Reduction (%)
	M100	Delta arm		M100	Delta arm	
X	5.5	1.7	68.5	10.8	4.9	54.9
Y	4.9	2.3	53.8	11.8	6.6	53.0
Z	10.4	1.9	81.4	22.3	5.7	74.4

Table 2.3: [1] Performances of the aerial robot in Vicon spot hovering with 1 m/s wind along Y-axis

	RMSE (mm)		Reduction (%)	Max Fluctuation (mm)		Reduction (%)
	M100	Delta arm		M100	Delta arm	
X	7.8	2.8	63.8	15.9	8.2	48.7
Y	22.1	5.2	76.5	52.1	11.7	77.6
Z	14.0	3.4	75.6	29.3	9.5	67.6

2.4.3 UAV positional error compensation

A series of autonomous flight tests were conducted for demonstrating the ability of the system to position its end-effector accurately at a target point. To assess the performance of the end-effector stabilisation by the Delta manipulator, we tested the aerial robot in both still air and in a 1m/s windy condition. The wind is created by exposing the robot to an electric fan generating 5500 cubic feet per minute (CFM) air flow directed at the robot while it hovers at spot $[0, 0, 1.5]^T$ m in the world frame.

The test results of the aerial robot while it hovers in still air is given in Table 2.2. As illustrated in Fig.2.7, the aerial robot using compensation function of the Delta manipulator is capable of decreasing both RMSE and the maximum fluctuations of the end-effector in all directions. The RMSEs (raw values and reduction percentages shown in tables to one decimal place) decrease 68.5%, 53.8% and 81.4%, while the maximum fluctuations (raw values and reduction percentages also shown in tables to one decimal place) decrease 54.9%, 53.0% and 74.4% in X, Y, and Z direction respectively.

In comparison to hovering in still air, the test results of the hovering aerial robot exposed a 1m/s windy condition with Y-direction wind generated by an electric fan is given in Table 2.3 and illustrated in Fig.2.8. The results show that the Delta manipulator is able to compensate for the fluctuations of the quadrotor platform and decrease both RMSEs and maximum fluctuations of the end-effector in all directions. As given in Table 2.3, the RMSEs decrease 63.8%, 76.5% and 75.6%, while the maximum fluctuations decrease 48.7%, 77.6% and 67.6% in X, Y, and Z directions respectively.

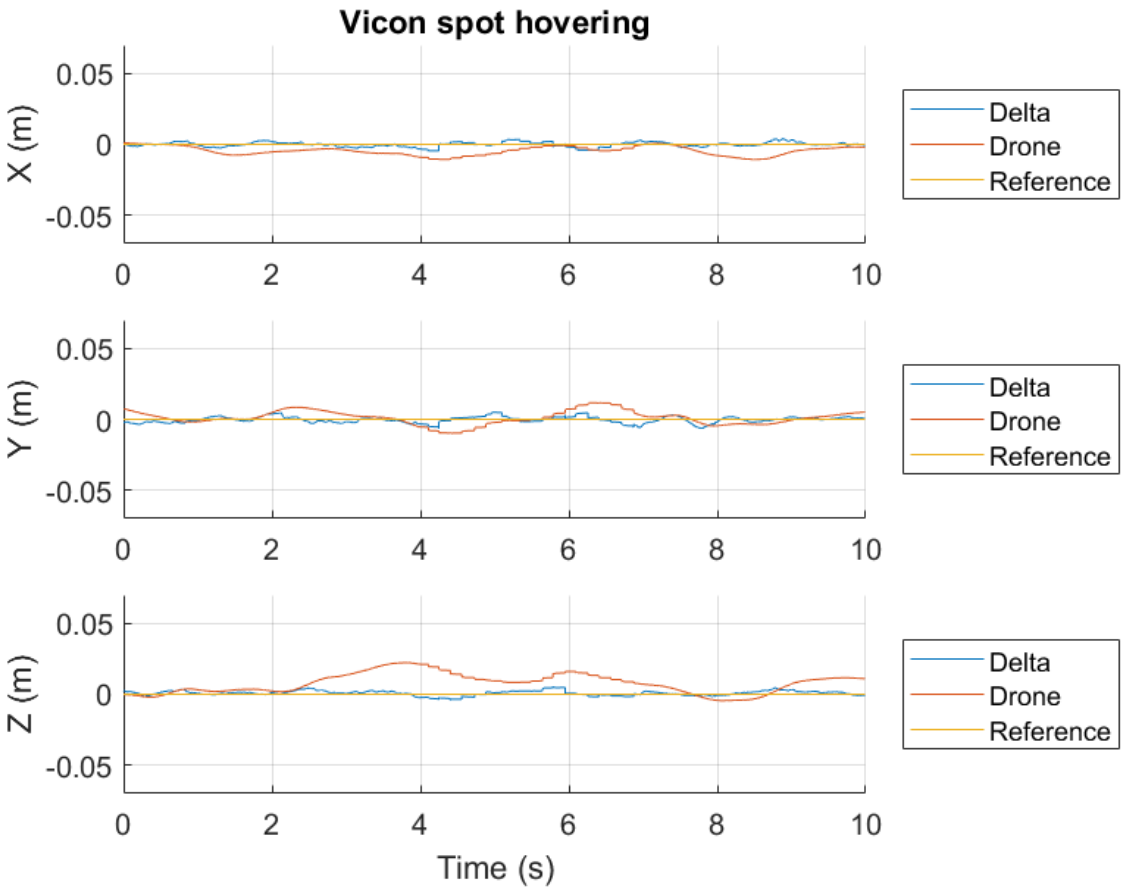

Figure 2.7: [1] Fluctuations from command reference level of the quadrotor platform and the end-effector of the integrated aerial robot in Vicon-based spot hovering mode.

We further assessed the performance of the aerial robot using VI odometry-aided navigation by first hovering in still air and then in a windy environment. The Vicon motion capture system is used to obtain the ground truth of the position of the end-effector and the quadrotor platform. The test results of the aerial robot hovering in still air is given in Table 2.4 and illustrated in Fig.2.9. In this operating scenario, the end-effector implements improved accuracy as the RMSEs decreased by 47.4%, 25.9% and 41.9%, while the maximum fluctuations decreased by 43.4%, 14.7% and 41.2% in X, Y, and Z direction respectively.

The results of the aerial robot exposed to Y-direction wind generated by an electric fan is given in Table 2.5. In this case, the end-effector also demonstrates improved accuracy (Fig.2.10) as the RMSEs decreased by 76.4%, 44.1% and 35.8%, while the maximum fluctuations decreased by 52.8%, 46.9% and 33.6% in X, Y, and Z direction respectively.

Across these four flight test scenarios, and in terms of targeted accuracy of Z-axis max fluctuation of 20 mm and X-axis and Y-axis RMSE of 5.7 mm, the aerial Delta Manipulator is able to pass the performance criteria in Vicon spot hovering, Vicon spot hovering with 1 m/s wind along Y-axis, and VI odometry spot hovering.

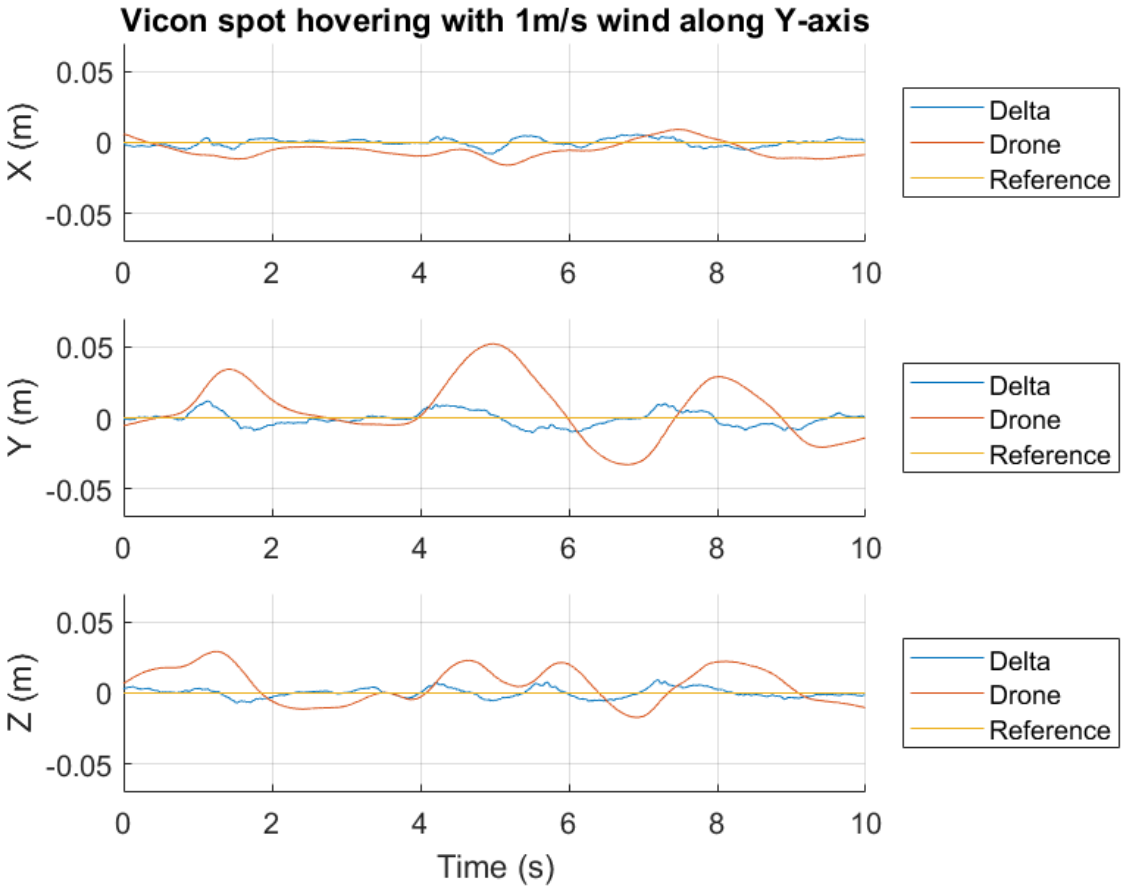

Figure 2.8: [1] Fluctuations from command reference level of the quadrotor platform and the end-effector of the integrated aerial robot in vicon based spot hovering mode with 1 m/s wind along Y-axis.

Table 2.4: [1] Performances of the aerial robot in visual-inertial spot hovering

	RMSE (mm)		Reduction (%)	Max Fluctuation (mm)		Reduction (%)
	M100	Delta arm		M100	Delta arm	
X	7.0	3.7	47.4	15.0	8.5	43.4
Y	7.2	5.3	25.9	16.1	13.7	14.7
Z	8.3	4.8	41.9	17.5	10.3	41.2

Table 2.5: [1] Performances of the aerial robot in visual-inertial spot hovering with $1m/s$ wind along Y-axis

	RMSE (mm)		Reduction (%)	Max Fluctuation (mm)		Reduction (%)
	M100	Delta arm		M100	Delta arm	
X	27.1	6.4	76.4	39.5	18.7	52.8
Y	26.5	14.8	44.1	78.1	41.5	46.9
Z	25.0	16.0	35.8	47.9	31.8	33.6

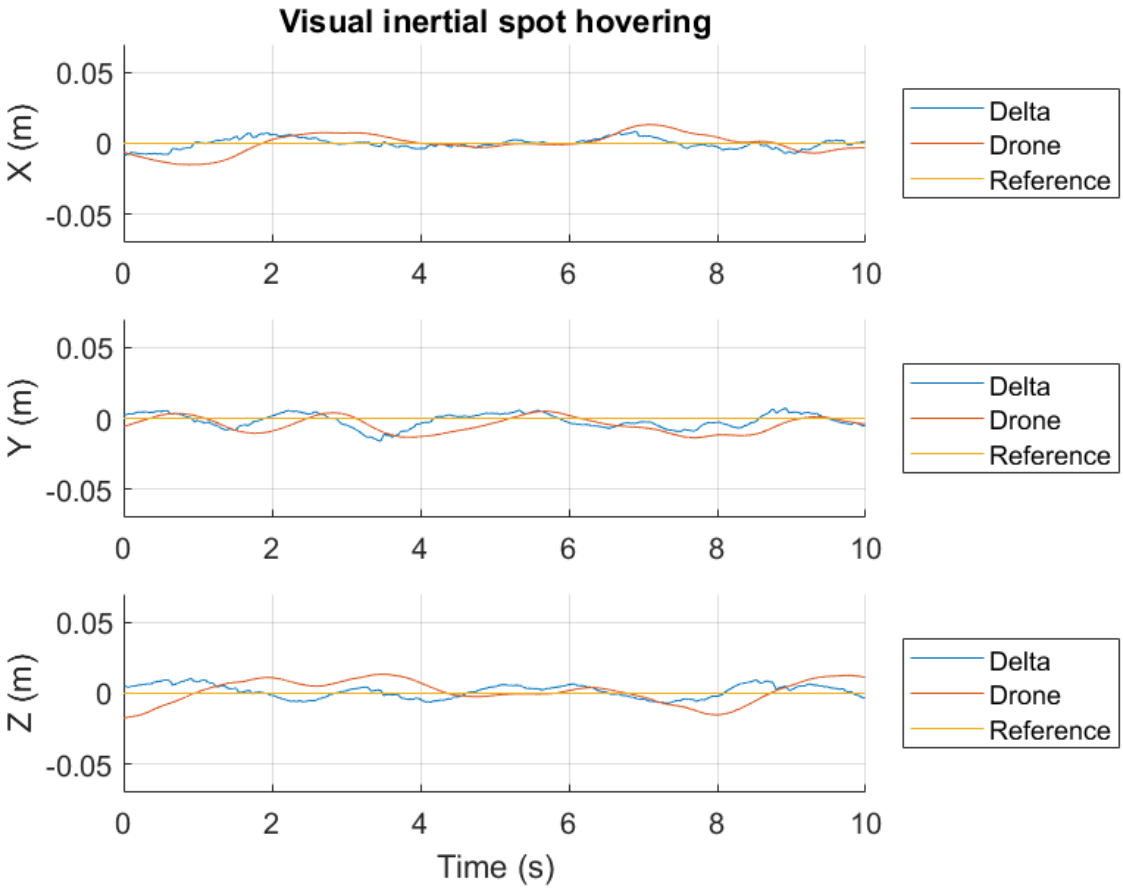

Figure 2.9: [1] Fluctuations from command reference level of the quadrotor platform and the end-effector of the integrated aerial robot in VI-odometry-aided spot hovering in still air.

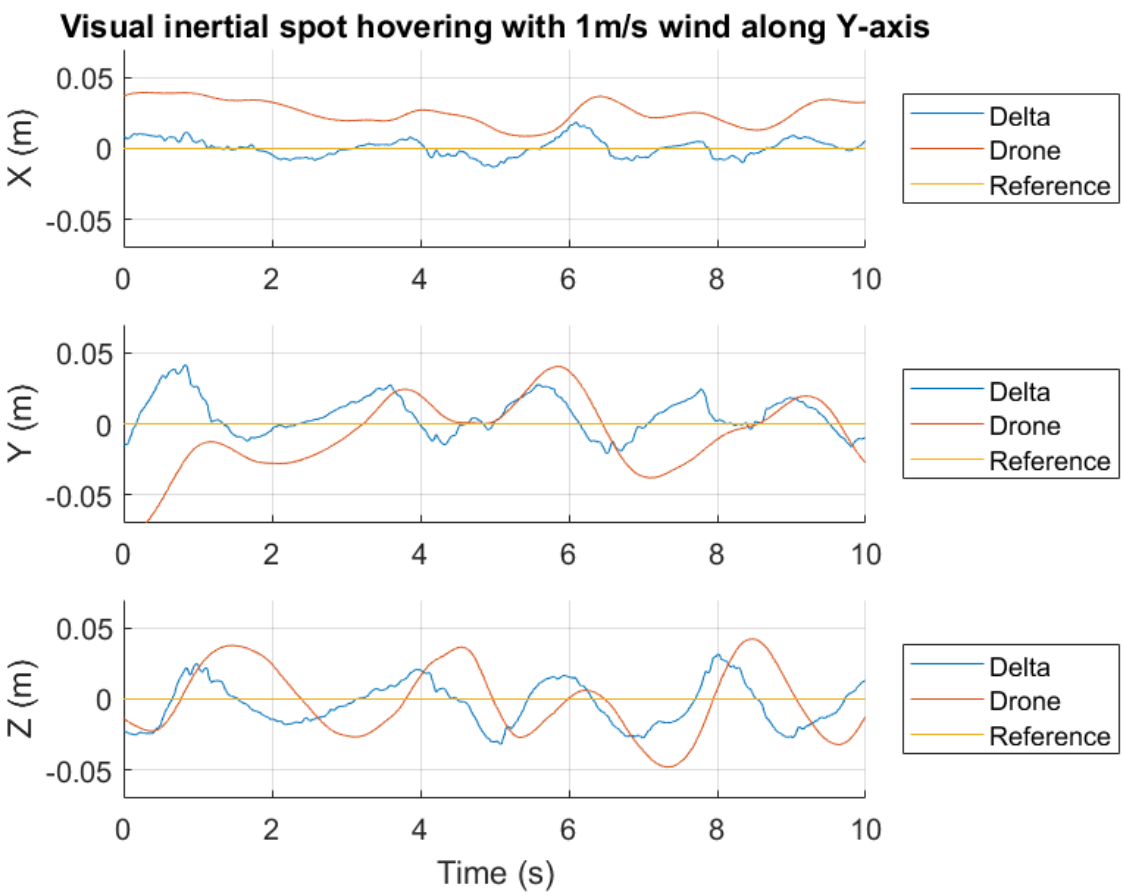

Figure 2.10: [1] Fluctuations from command reference level of the quadrotor platform and the end-effector of the integrated aerial robot in VI-odometry-aided spot hovering with 1 m/s wind along Y-axis.

2.5 Case study: aerial repair with amorphous construction and repair materials

We designed an extrusion mechanism (Fig. 2.5) for depositing amorphous repair materials, such as LD40 Polyurethane foam, to effectively seal leaking spots including cracks and holes. Using two components PU foam has the advantage that the material properties can be easily modified.

2.5.1 Material deposition characterisation: LD40 polyurethane foam

To facilitate autonomous control of material deposition using the above extruding mechanism and complete an aerial repair mission in a hard-to-reach position, we analysed the performance of the mixed foam quantitatively with experimental tests.

Given the volume of the nozzle, V_{nozzle}, used in the mechanism, the continuous flow rate Q through the nozzle is calculated by V_{nozzle}/t. To maintain this flow rate, the angular speed of the servo is derived as

$$\omega_m = \frac{2V_{nozzle}}{\pi t l {D_{syringe}}^2} \tag{2.9}$$

in which $R_{syringe}$ is the inner diameter of the 20ml syringe, t is the time required to drive the material out of the nozzle, and l is the lead of the screw thread.

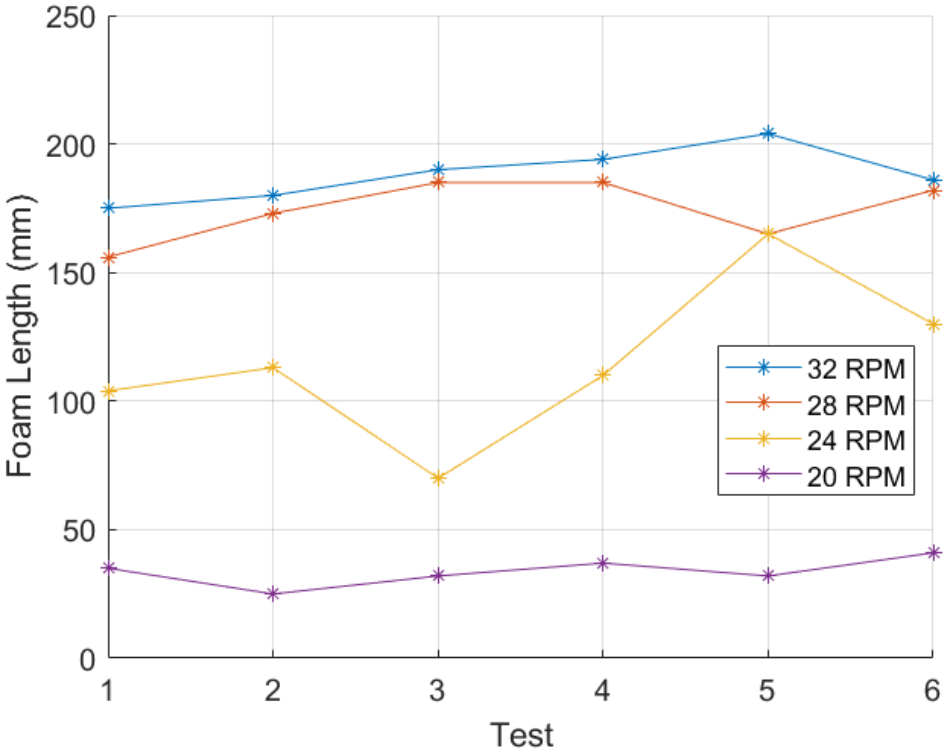

(a)

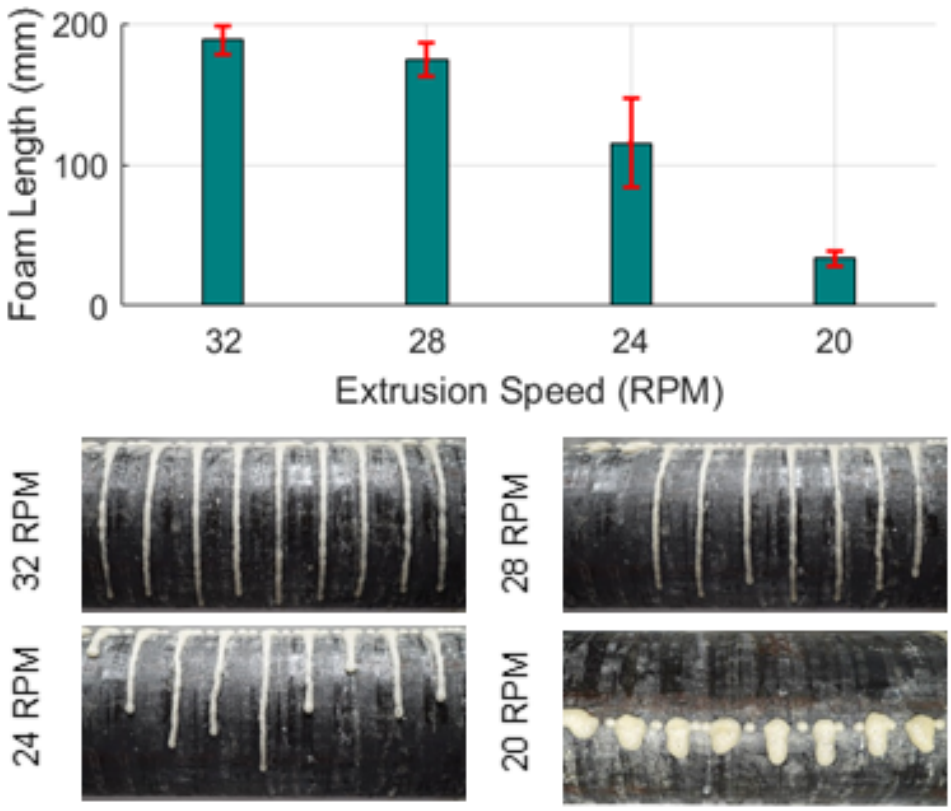

(b)

Figure 2.11: [1] **The flowability of the mixture at various depositing flow rate on a pipe surface** (**a**) length of the flow per test spot, (**b**) average length of the flow per extruding speed.

The cream-time of LD40 polyurethane foam is about 13-18 seconds, as given in the technical data sheet [59]. The material should therefore remain no longer than 18 seconds in the nozzle in order to drive the mixture out of the static mixing nozzle with little force. During this time we can assume that there is no significant change of viscosity of the mixture in the nozzle.

Substituting numerical values to Eq. 2.9, we derive a reference angular angular velocity of 32 rpm for the servo. By reducing the angular velocity, the flow rate of the two part foam material slows down and the mixture will become creamy within the nozzle. This further reduces the flowability of the mixture when it is deposited on an inclined surface.

To analyse the flowability of mixed LD40 foam at various depositing flow rates, we control the servo at different angular velocity starting from 32rpm, and continue to deposit material at spots on top of a typical steel pipe used in construction and infrastructure applications (D = 168mm) for 2 seconds at each spot. We then reduce the servo speed by equal decrements of 4 rpm until the mixture doesn't flow down. The length of the flow down the pipe surface after setting is measured and reported in Fig. 2.11. The results reveal that the mixture deposited on top of the pipe will not flow down while the servo turns at less than 20 rpm.

The power for driving the PU foam out of the mechanism is provided by the Dynamixal servo. The mechanical power available from the gearbox output shaft is calculated by $\tau\omega$, where τ is the output torque and ω the angular velocity. Both the applied torque and real turning speed of the servo are readable with the control algorithm. For extruding tests at different extruding speeds without the static mixing nozzle, there are no significant changes for the required average torque output percentage, as shown in Fig. 2.12. After adding the mixing nozzle, the results reveal that to maintain a depositing flow rate with the servo turning at 32 rpm requires an increase of 20% torque output. These results also show that the lowest turning speed at 20 rpm requires an average of 15% torque output increase due to the higher viscosity of the mixture.

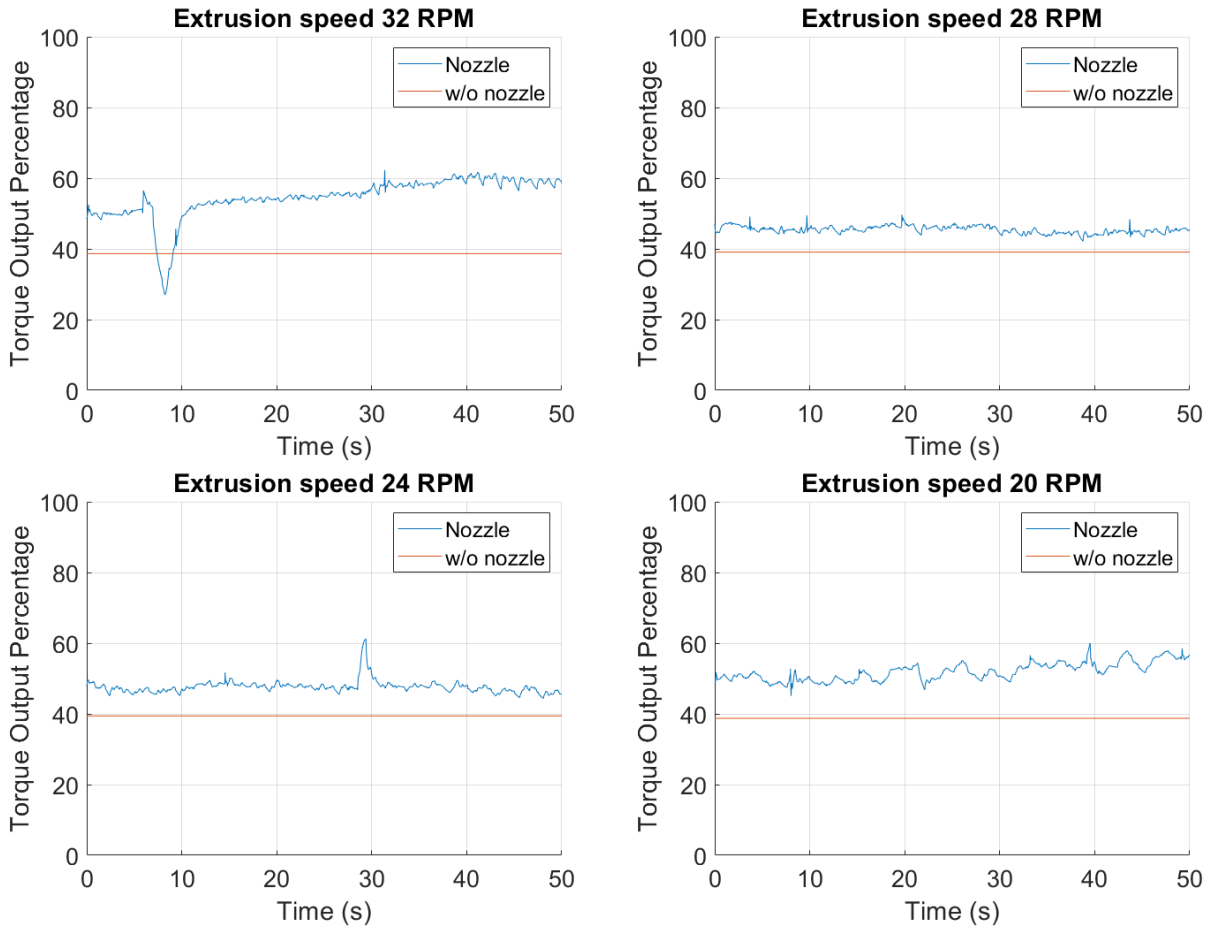

Figure 2.12: [1] Power consumption of the extrusion mechanism at various extruding speeds.

With the experimental results above, we can systematically control the servo velocity to have a mixture with higher flowability by increasing the extruding flow rate and thus a larger flow distance on the pipe surface. Conversely, a slower servo velocity leads to a mixture with higher viscosity and lower flowability, resulting in a creamier foam immediately after deposition.

2.5.2 Leaking sites sealing tests with autonomous flight

This preliminary experimental test is designed to implement an aerial repair using the robotic system presented in this paper. In the test, a section of steel oil pipe with 168 mm diameter is used as a sample, on which a 15 mm straight line crack and another two 10 mm diameter leaking holes are assumed as repair targets.

The locations for the start and end point of the straight-line cracks and the centres of the two holes are obtained using the Vicon system before printing. Knowing these position vectors as key points in the coordinate frame of the Vicon system, a trajectory is then designed for autonomous flight with consideration to the maximum speed of DJI M100 and the distance between the tip of the nozzle and the pipe to avoid physical collision.

Given the fluctuation range of 0.0114 m in the vertical direction of the end-effector of the Delta manipulator, a minimum distance of 0.02 m is set between the tip of nozzle and the pipe as a buffer zone. With a number of flight tests for calibrating the practical flight trajectory, the distance between the mass centre of the drone and the surface of the steel pipe is established at 0.38 m.

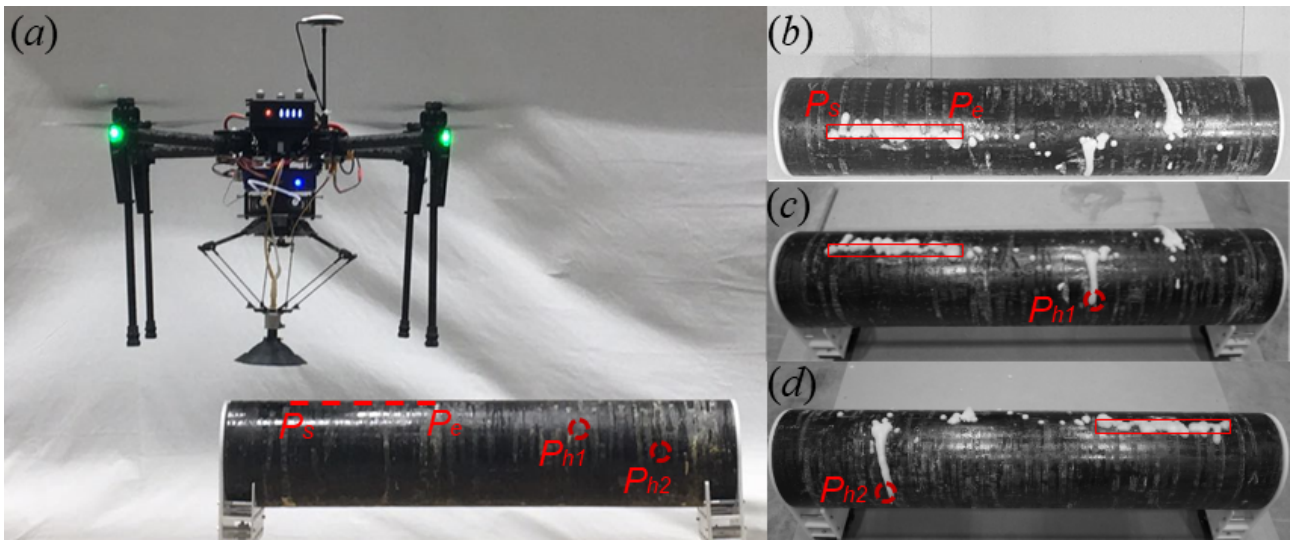

Figure 2.13: [1] **The repair task setup and deposited PU foam for sealing cross-section crack between P_s and P_e and holes at P_{h1} and P_{h2}:** (**a**) front view of the repair test, (**b**) top view of the expanded foam, (**c-d**) side view of the expanded foam at point P_{h1} and P_{h2}.

To implement the repair task, the aerial robot takes off from the side close to the starting point P_s and flies up to 1 m over the pipe. It then moves to the top of point P_s and consequently descends to the desired printing height as shown in Fig. 2.13(a). In this part, we adjust the velocity of the robot to match the required material depositing velocity, enabling the optimum repairing quality. After sealing the straight-line crack, the robot flies to points P_{h1} and P_{h2} and subsequently hovers over them to fill the two holes. After finishing the repair, the robot flies away from the work-site and lands on the right side of the pipe. Materials accumulated along the straight-line crack and holes on the pipe after the repair are shown in Fig.2.13 (b), (c) and (d).

During this test, the implemented trajectories of the M100 and the Delta manipulator are recorded in the motion capture environment and plotted with respect to their trajectory references as shown in Fig. 2.14.

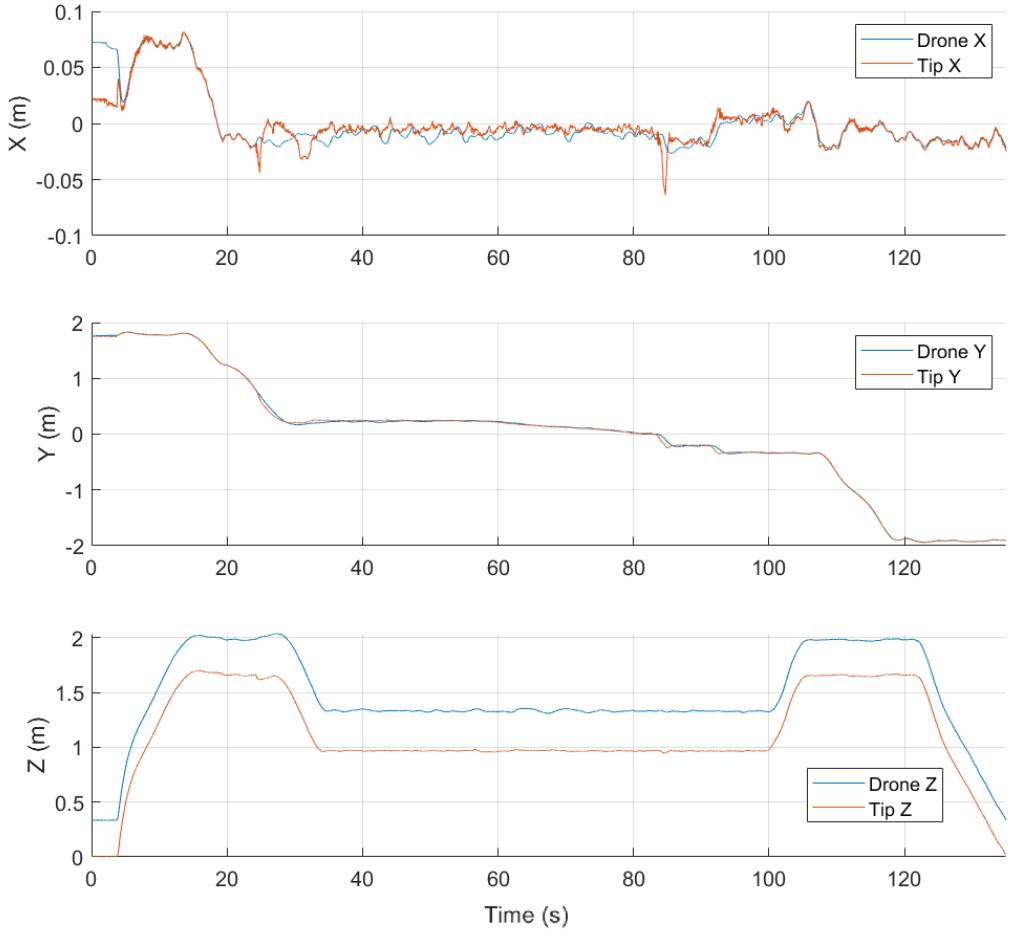

(a)

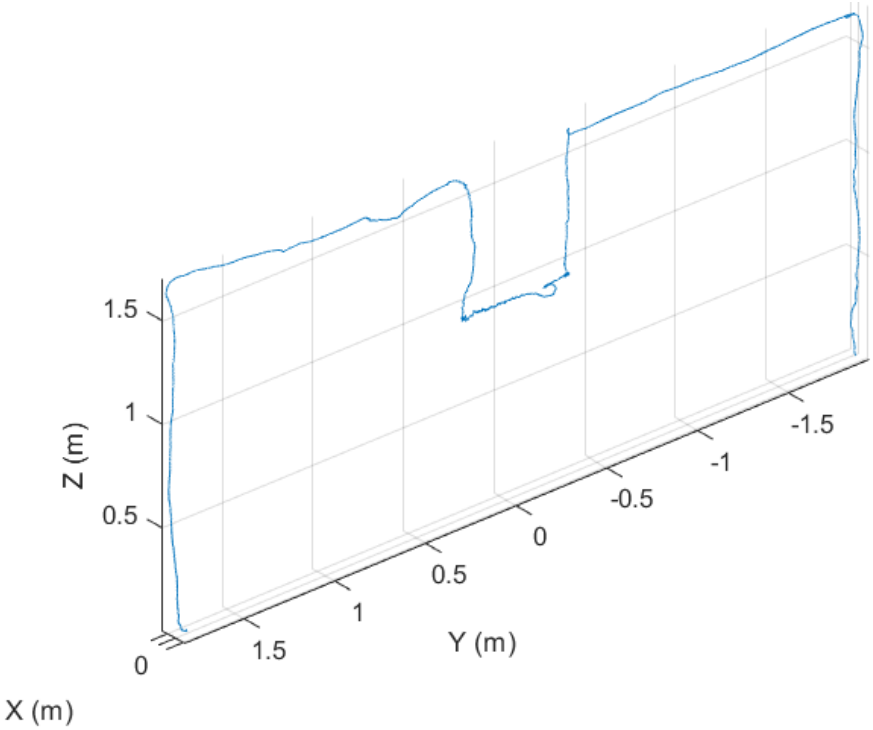

(b)

Figure 2.14: [1] **Reference and implemented trajectories of the M100 and the end-effector of Delta manipulator in the pipeline repair process:** (**a**) decomposed trajectories of the whole repair process along X-, Y- and Z-axis, (**b**) three dimensional trajectory of the planned repair process.

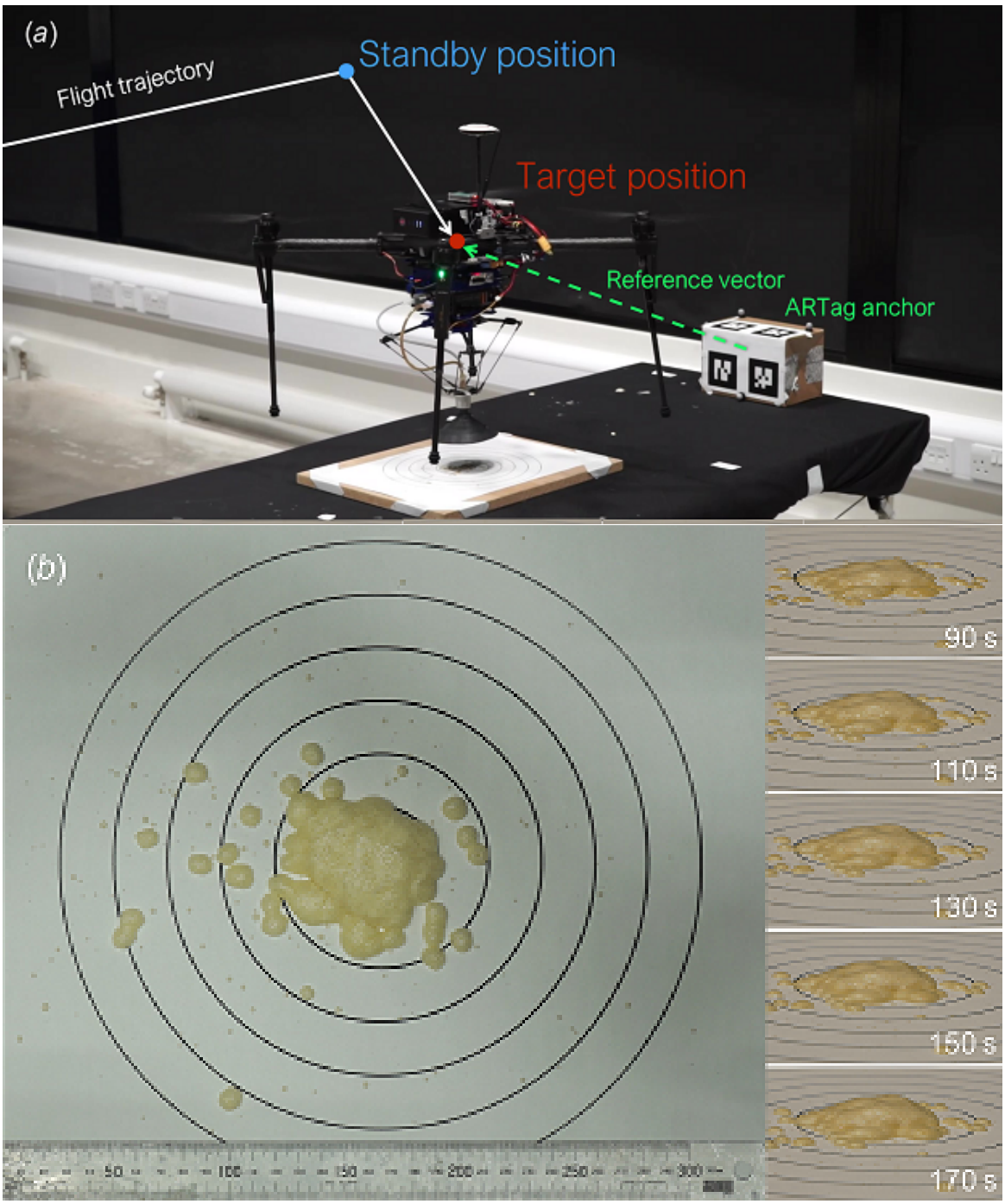

Figure 2.15: [1] **The aerial repair mission using VI odometry-aided navigation.** (**a**) the flight trajectory of the aerial robot for the aerial repairing process, (**b**) the foam material expansion progress in a period of 80 s after deposition at the target spot and the top view showing the final scale.

A VI odometry-aided aerial repair work process is demonstrated in Fig. 2.15(a). In this repair process, the ARTag is placed in front of the repair target and a reference vector is calculated so that the target position of M100 is on the top of the repair target. M100 first flies to the standby position where the ARTag is in the view of the ZR300 camera, then the M100 begins to track the ARTag and maintain the constant reference vector with the ARTag. Once the target position is reached, the delta manipulator starts to stabilize the end-effector and the liquid expansion foam is extruded onto the repair targets precisely, as illustrated in Fig. 2.15(b).

2.6 Conclusion

This work presents a new concept for precise aerial repair, including sealing and filling of cracks. An integrated light-weight 3-DOF Delta manipulator and closed-loop position controller allows high-precision end effector positioning on a UAV platform, showing higher precision than positioning the end effector with the UAV alone. Quantitative experimental data demonstrated that the integrated 3-DOF Delta manipulator is capable of compensating both the translation and rotation offset of the UAV frame, thereby achieving improved accuracy in all directions in the four no-wind and windy test scenarios. We present experimental demonstrations of pipeline repair and flat surface spot sealing by extruding LD40 polyurethane foam from the autonomous aerial robot. These tests verified the concept of using the proposed system for the repair of targets with different geometric shapes. This work can enable potential applications including accurate aerial inspection and repair for infrastructures in challenging environments, such as nuclear or petrochemical plants.

This work initiates a framework for implementing repair tasks at height. Using the on-board camera, the potential of using this system to autonomously identify and repair a fault will be further investigated.

This chapter will be concluded with key points of achievements and progress towards AAM.

- This early-stage proof of concept demonstrates capability of material deposition with UAVs. The integrated 3-DOF Delta manipulator allows high-precision end effector positioning on a UAV platform, providing a first step towards aerial additive manufacturing.
- Case study of aerial repair with amorphous construction and repair materials, in this case LD40 2-part expanding polyurethane foam, has been demonstrated with its performance characterised and shown in this chapter.
- Future works
  - Material deposition accuracy must be improved for successful AAM.

- Further investigation into robustness of UAVs operations in challenging environments would benefit AAM and other UAVs applications.
- Amorphous construction and repair materials have potential to be used in construction material roles. However, the current deposition system has limited material storage capability and hence an improved version of prototype should be developed for further investigation regarding AAM with the certain materials.
- Autonomous aerial repair framework that can autonomously identify and repair faults or cracks using an onboard camera can be further investigated with this work as a basis for the robotic system.

Chapter 3

Robust Operation in Unpredictable Environments

3.1 Introduction

The work in this chapter was previously published in *Science Robotics* with the title "Rotorigami: A rotary origami protective system for robotic rotorcraft" [2, 3, 4]

Navigating in complex and cluttered environments remain an important challenge for many UAV applications. Currently, there are two main routes being investigated in the UAVs community: 1) obstacle detection and avoidance [60, 61, 62, 63, 64], and 2) impact mechanical resilience [65, 4, 66, 67, 68, 69, 70]. The first route mainly relies on sensing technology, for example, optical flow sensor [71, 72, 73], distance sensor [74, 75], lidar [76] and Simultaneous Localisation and Mapping (SLAM) [77, 78, 79], to determine the physical surroundings in order to navigate around them safely. The second route, instead of totally avoids obstacles, tries to cope with collisions when they occur. It relies on mechanical protection systems that protect UAVs from disturbances arising from collisions, which could otherwise cause a loss in control and crash the UAVs.

Most conventional UAVs today are not equipped with any kind of protection system, and any collision will potentially crash and damage components of the aerial robots. A protection system will add extra weight to the UAV and decrease its flight time, hence collision resilience from equipping such protection has often been sacrificed so that operators to extend the flight time. Impact reduction capability is also important consideration as most of conventional UAV protection systems are based on rigid frames and components, which do not significantly reduce collision forces. For example, rigid plastic frames have been used by DJI [80] and polystyrene foam frame has been used by Parrot AR drones [81] as their protection systems. These systems

are designed to be lightweight and inexpensive for commercial drones, but the materials used have high rigidity [82, 83], and thus will not be able to provide significant cushioning upon collision.

Protecting against normal and oblique collisions remains a big challenge for any size of UAVs. However, extra difficulty arises when equipping small UAVs with limited payload, and thus ruling out large and complex protection systems, which may be able to offer extra protection, to be used with these small aerial robots.

With extensively studies on origami structural properties [84, 85] and multiple works on exploring the concept of using origami structures as an impact protection system [86, 87, 88], origami engineering could be a solution to a lightweight and effective protection structure for UAVs.

However, another interesting concept is to have a protection structure in combination with a flight controller than can adapt to and recover from collisions. A relevant work has been reported in the literature [89], but this chapter only focuses on the mechanical aspect for the time being, leaving a possibility of collision-resilient controller-protector scheme for future work.

In this chapter, we report the design and development of a lightweight and cost-effective mechanical protection system for micro multirotor platforms. Impact protection capabilities of the new concept has been tested in comparison with the traditional rigid protection concept, showing superior performance to the traditional one.

3.2 Design and development

3.2.1 Impact protection strategies

The principle of individual propeller guards (Fig. 3.1A) is currently the most common protection accessory for multicopters. Although several variations of this configuration exist (including four connected and stringed guards), the principle drawback remains the same: because the guard is fixed to the drone, the moments induced due to the arising tangential force F_t and normal force F_n both contribute to the yawing moment about the center of the drone that causes flight instability.

As an improvement on the common individual protectors, we aimed to develop a mechanical system that withstands collisions effectively and can be integrated into existing flying platforms. A slightly improved variation to be considered in this conceptual analysis is the decoupled individual propeller guard (Fig. 3.1B): If the propeller guard was to rotate independently from the drone, assuming a decoupled system is implemented, then the moment arm due to Ft would

be reduced. However, this configuration has the same low resilience against the yawing moment induced by the normal force as in the previous configuration.

The advantage of a fixed universal (protecting all propellers) protector (Fig. 3.1C) over individual guards for a multicopter is that, in the case of a universal guard, the normal force, F_n, does not produce any yawing moment around the center of mass of the multicopter, assuming that the guard rotates around its center of mass [4, 90]. The final and most advantageous design considered is a decoupled universal protector (Fig. 3.1D). Theoretically, assuming that the center of the universal protector is coincident with the center of mass of the drone and that the friction in rotational joints between the platform and the protector is negligible, a decoupled universal protector will eliminate all yawing moments arising from the collision.

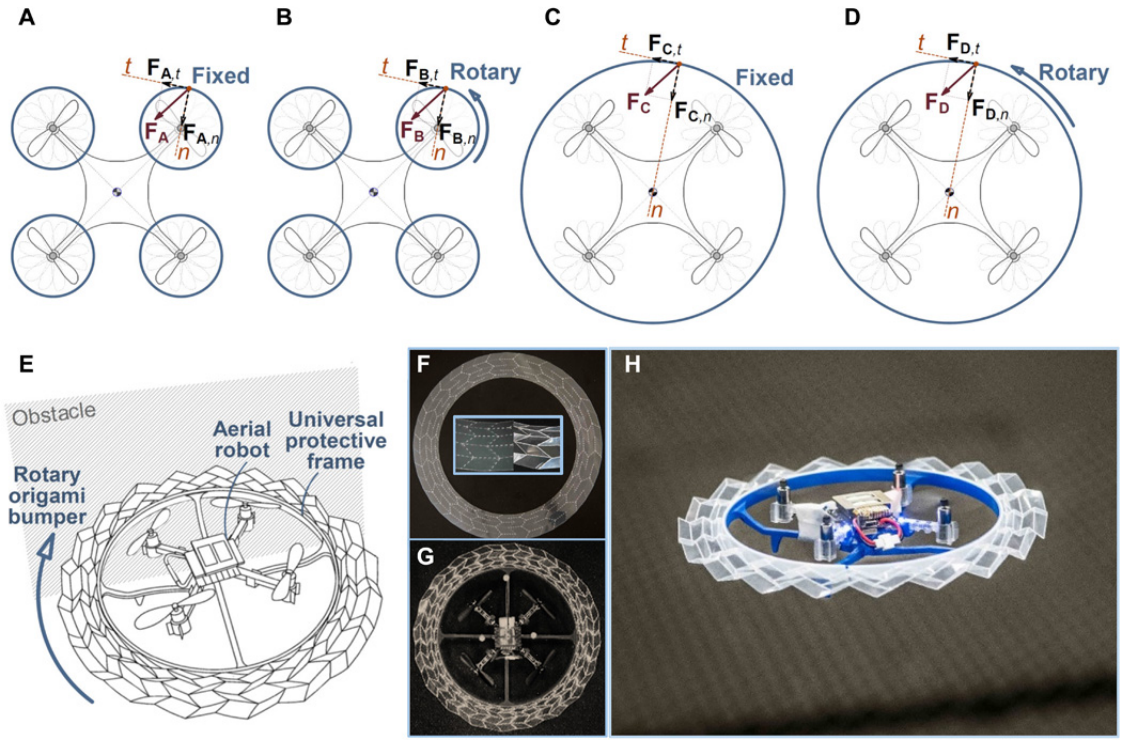

Figure 3.1: Conceptual analysis, design, and development of Rotorigami for quadcopters. (**A** to **D**) Graphical representations of four mechanical protection systems: (**A**) fixed individual propeller protector, (**B**) rotary individual propeller protector, (**C**) fixed universal protector, and (**D**) rotary universal protector. (**E**) Rotary universal protector with origami cushion. (**F**) Laser-cut pattern and its detailed view before and after folding along its perforated crease lines. (**G**) A miniature quadcopter equipped with Rotorigami (Rotary Origami Protective System) in a plan view and (**H**) in flight. Figure courtesy by Pooya Sareh. [2]

In addition to moment decoupling as a first strategy, a second strategy to enhance the impact robustness of aerial robots is to minimise the peak collision force experienced by the platform. Given the weight of the protector as a main challenge and to realise the notion of an ultra-lightweight impact cushion, we demonstrated the functionality of an origami impact protector made of a very thin plastic sheet (Fig. 3.1, E to H). Among a large variety of origami patterns, the Miura-ori [91, 92, 93, 94] is perhaps the most widely used tessellation in engineering de-

sign as a result of its manufacturing simplicity, geometric versatility, and desirable functional properties. Full origami design and analysis can be found in the author's publication [2].

3.2.2 Materials and methods

The impact-protection origami structure was folded manually from a 0.2-mm-thick laser-cut sheet of polypropylene (Fig. 3.1F). To facilitate folding and to ensure the accurate geometric replication of the origami model, we engraved perforations along the fold lines of the pattern using a Versa CO2 laser cutter (Universal Laser Systems PLS6.75). To change their depth and width, we engraved these fold line perforations by using different power settings on the laser cutter. Because low engraving power settings may create scores that do not cut through the entire thickness of the sheet, the mountain and valley fold lines were engraved separately on each side of the sheet. The plastic deformation created along the fold lines is an important element to consider when assessing the structural performance of the manufactured protection structure. The structure was assembled on a three-dimensionally printed acrylonitrile butadiene styrene plastic frame in the form of a cylindrical shell with a thickness of 1.1 mm.

The palm-sized quadrotor Crazyflie 2.0 was chosen to be the testing platform. Its small size (92 mm 92 mm 29 mm) and reasonable payload capacity of up to 18 g ensured that the protection frame and the origami structure were fabricated on a small scale, thereby reducing complexities in their manufacturing processes. The small size and the limited payload of this platform also demonstrated the benefits of origami-inspired solutions as impact-protection structures. These benefits include low weight and high design flexibility to achieve a desirable level of structural performance by perforating and folding an inexpensive plastic sheet.

3.3 Experimental setup

To investigate the capabilities of the proposed protective concept, we carried out impact experiments with a miniature multirotor aerial robot. The following are the four universal design configurations that were tested for their impact resilience performance: (**i**) fixed naked (Fig. 3.1C), (**ii**) rotary naked (Fig. 3.1D), (**iii**) fixed origami-protected [Fig. 3.1E; without rotational degrees of freedom (DOF)], and (**iv**) rotary origami-protected (Fig. 3.1E; with rotational DOF) universal protectors. The peak impact force and angular speed of these design configurations were measured and analysed to compare their corresponding impact protection qualities in normal and oblique collisions. In these experiments, pendulum swing tests were performed by using the quadcopter equipped with an inertial measurement unit (IMU) module as a pendulum mass. A maximum velocity of 1.2 m/s at the lowest point of the pendulum swing was set as a typical target velocity to simulate a horizontal collision to a surface.

To obtain certain collision velocities, we used a simple energy conservation equation between potential and kinetic energy ($E = mgh = 0.5\ mv^2$) to calculate the required height at a pendulum releasing point, where E is the total amount of mechanical energy, m is the pendulum mass, h is the height of the pendulum from the releasing point to the point of impact, and v is the velocity upon impact to the wall. An electromagnet was used to hold and release the vehicle precisely to make sure that each collision has the same initial velocity and initial orientation for each testing configuration (fig. 3.2A).

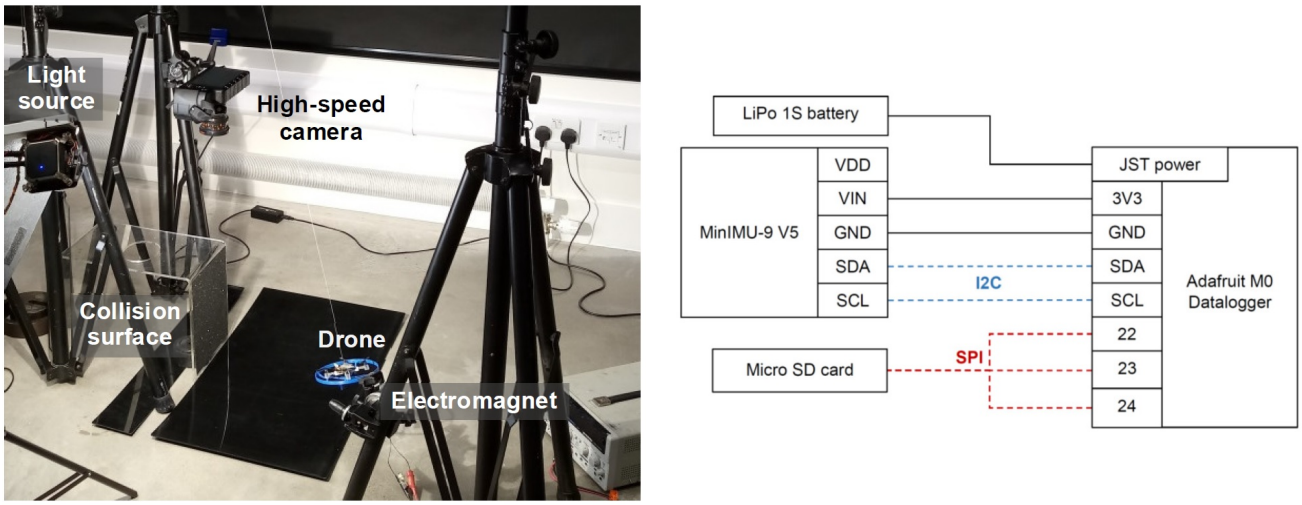

(A) Experimental setup for pendulum collision tests of a miniature quadcopter to a surface.

(B) Connection between MinIMU-9 V5 and Adafruit Feather M0 data logger.

Figure 3.2: Mechanical and electronic setup of the collision experiments. [2]

We integrated a miniature data logging system into the aerial robot for the measurement of dynamic variables. The MinIMU-9 V5 with LSM6DS33 (featuring a three-axis accelerometer and a three-axis gyroscope) and LIS3MDL (featuring a three-axis magnetometer) was chosen as an IMU due to its small size, high data rate, and broad range of sensing. The Adafruit Feather M0 data logger with micro secure digital (SD) card module was programmed and connected to work with the above sensor. The connection diagram was shown in Fig. 3.2B. An Arduino library for LSM6 devices from Pololu was modified by using the SdFat library to increase micro SD card writing speed [95, 96]. An Ultra Micro secure digital high capacity (SDHC) card with UHS-I bus interface was tested with the data logger in terms of sensor data writing speed. A maximum reliable writing rate of 600 Hz was achieved with minimum and maximum time steps of 1661 and 1673 s, respectively, between successive data samples. To match the above SD card data writing rate, certain LSM6 control registers were changed from default values to modify sensor ranges and data rates (see table 3.1). In this configuration, the accelerometer range was set at the maximum value of 16g and with the data rate of 833 Hz to ensure that the sampling rate was high enough that the data logger would log a new data point from the sensor every time.

Control register	Value (Hex)	Value (Binary)	Description
CTRL1_XL	0x74	0b01110100	Accelerometer range = ±16g, data rate = 833 Hz, AAF = 400Hz
CTRL2_G	0x7C	0b01111100	Rotational velocity range = 2000 DPS, data rate = 833 Hz

Table 3.1: Control registers for MinIMU-9 V5 with LSM6DS33 [2]

The masses of the robot naked and with the origami protector were not the same due to the added weight of the origami structure; the origami-protected configurations had a mass of 53.0 g, whereas the naked configurations were both 48.5 g. Hence, the impact forces were calculated from the actual mass of each design configuration. The impact surfaces were switched between smooth (acrylic glass) and rough (sandpaper with ISO Grit P80) to determine the effect of the friction coefficient of hitting surfaces. The pendulum string held the drone at certain positions to simulate impacts at different angles of collision with respect to the colliding surface: 30°, 60°, and 90°(normal collision). For each collision scenario, the average values of force and angular speed from five tests were plotted on the basis of 30 samples at a 600-Hz sampling frequency, with peak forces aligned to show relevant force and angular speed profiles before and after impact. Each line plot also contains its minimum and maximum occurred values in the sample data sets to show the range of the data (Figs. 3.3 and 3.6).

3.4 Results

3.4.1 Impact-cushioning strategy: naked versus origami-protected configurations

The collision duration in the origami-protected systems was observed to be notably longer than that of the naked systems, providing a substantial level of impact cushioning. We began by comparing the impact protection quality between naked and origami-protected systems in a normal collision (movie S1 in [2]). The force and angular speed profiles of both systems for each experiment setup are plotted in the same figure to aid visual comparison (Fig. 3.3 and table 3.2). The peak force reduction turned out to be around 30% for both fixed (Fig. 3.3, A and C) and rotary (Fig. 3.3, B and D) origami-protected systems when compared with the naked configurations. The next study consisted of collisions at 6°(movie S2 in [2]); given the fact that impacts at this angle are closer to normal rather than tangential collision, the normal component of the impact force was dominant. The peak force reduction by the origami structure in both fixed and rotary configurations was around 38% on average. Last, for impacts at 30°with respect to the collision surface, in which the tangential collision force was dominant, the peak force reduction was around 20%.

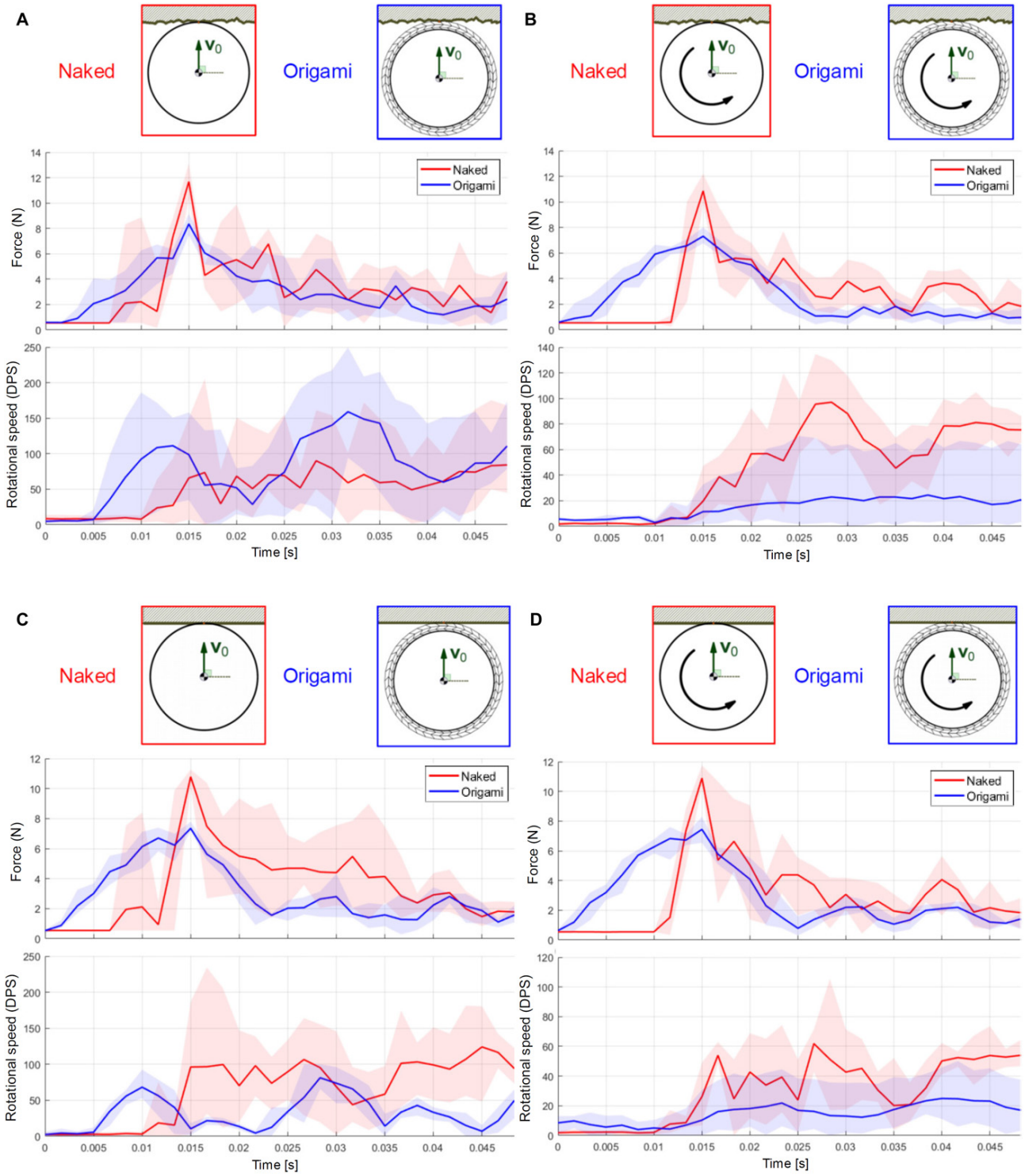

Figure 3.3: Force and angular speed profiles at a contact angle of 90° (normal collision) and impact speed of 1.2 m/s for the naked and origami-protected configurations on the rough and smooth surfaces. The shaded areas represent the range of data (from five trials) corresponding to each collision. (**A**) Rough surface with fixed protector. (**B**) Rough surface with rotary protector. (**C**) Smooth surface with fixed protector. (**D**) Smooth surface with rotary protector. [2]

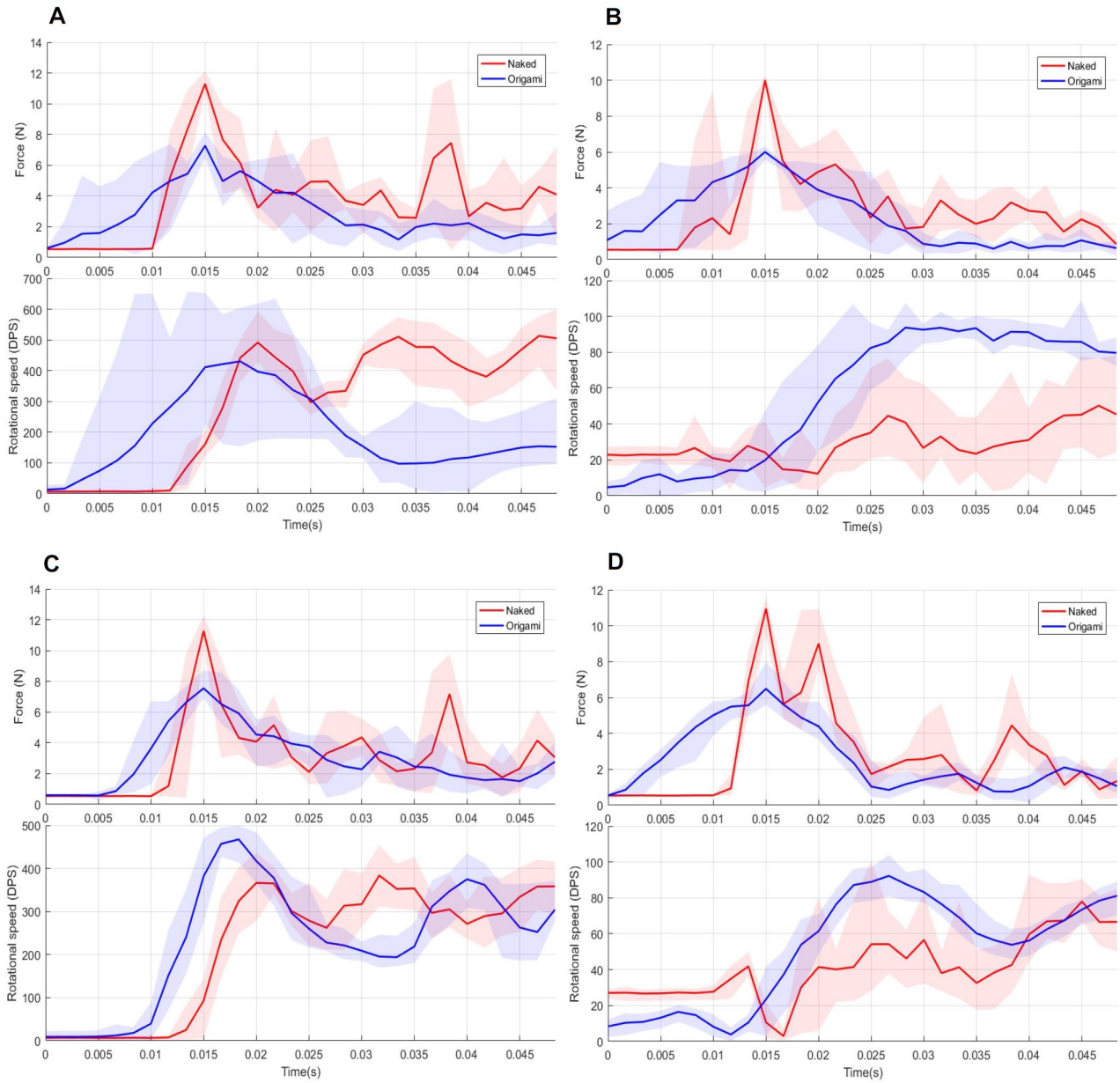

Figure 3.4: Force and angular speed profiles at a contact angle of 60° and impact speed of 1.2 m/s for the naked and origami-protected configurations on the rough and smooth surfaces. The shaded areas represent the range of data (from five trials) corresponding to each collision. (**A**) Rough surface with fixed protector. (**B**) Rough surface with rotary protector. (**C**) Smooth surface with fixed protector. (**D**) Smooth surface with rotary protector. [2]

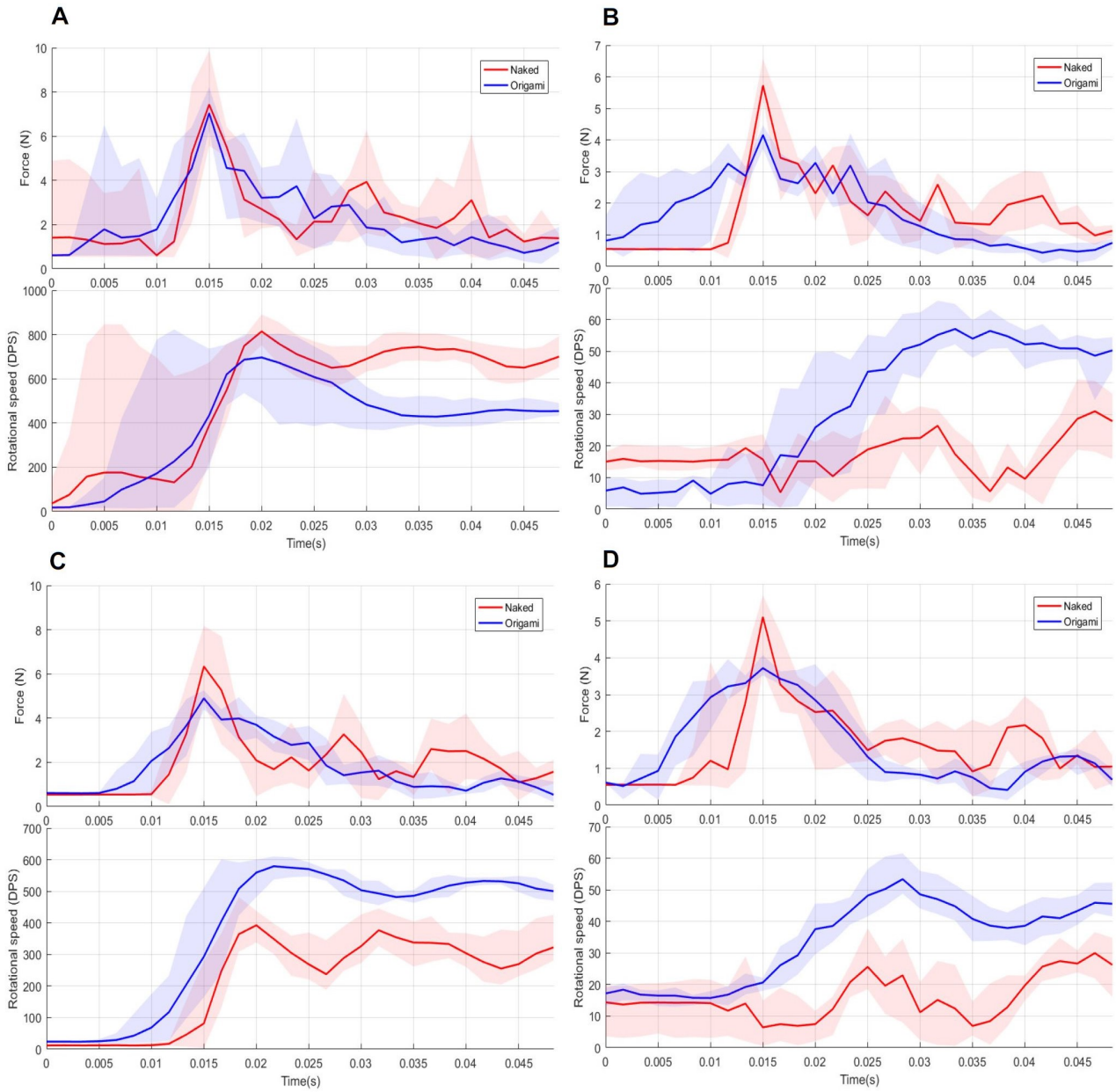

Figure 3.5: Force and angular speed profiles at a contact angle of 30° and impact speed of 1.2 m/s for the naked and origami-protected configurations on the rough and smooth surfaces. The shaded areas represent the range of data (from five trials) corresponding to each collision. (**A**) Rough surface with fixed protector. (**B**) Rough surface with rotary protector. (**C**) Smooth surface with fixed protector. (**D**) Smooth surface with rotary protector. [2]

3.4.2 Moment-decoupling strategy: fixed versus rotary configurations

To investigate the performance of the rotary configurations compared with the fixed ones, we plotted force and angular speed data in a way similar to the previous section. In this case, rather than comparing naked and origami-protected systems, data for the fixed and the rotary systems were plotted in the same graph for each experiment setup. The effect of the rotary concept on the reduction of rotational speed after impact was demonstrated in the 30°impact experiments (Fig. 3.6 and movie S3 in [2]), where the tangential component of collision force was relatively large. As anticipated, every fixed protection system displayed considerably higher rotational speed after impact compared with the rotary systems. Specifically, the fixed protection systems were not effective against the rough surface in sliding collisions, because the average maximum angular speed for fixed naked and fixed origami-protected systems were recorded to be around 814 and 697 degrees per second (DPS), respectively. Although those values for the fixed protection system on the smooth surface were lower compared with those of the rough surface due to lower friction, they were still significantly high: around 392 and 579 DPS for fixed naked and fixed origami-protected systems, respectively. In contrast, the rotary systems effectively decoupled shear impact force, resulting in an average maximum angular speed of one order of magnitude smaller compared with those of the fixed protection systems in the collision scenarios above. In the 60°collision experiments, again, the rotary protection systems showed superior impact-reduction performance in all tests: On average, a reduction in angular speed around 82% (Fig. 3.7 and table 3.2) was achieved for the four collision scenarios by using the moment-decoupling strategy. In normal collisions, the fixed and rotary systems performed similarly as expected because of the dominance of the normal component of the collision force (Fig. 3.8 and table 3.2).

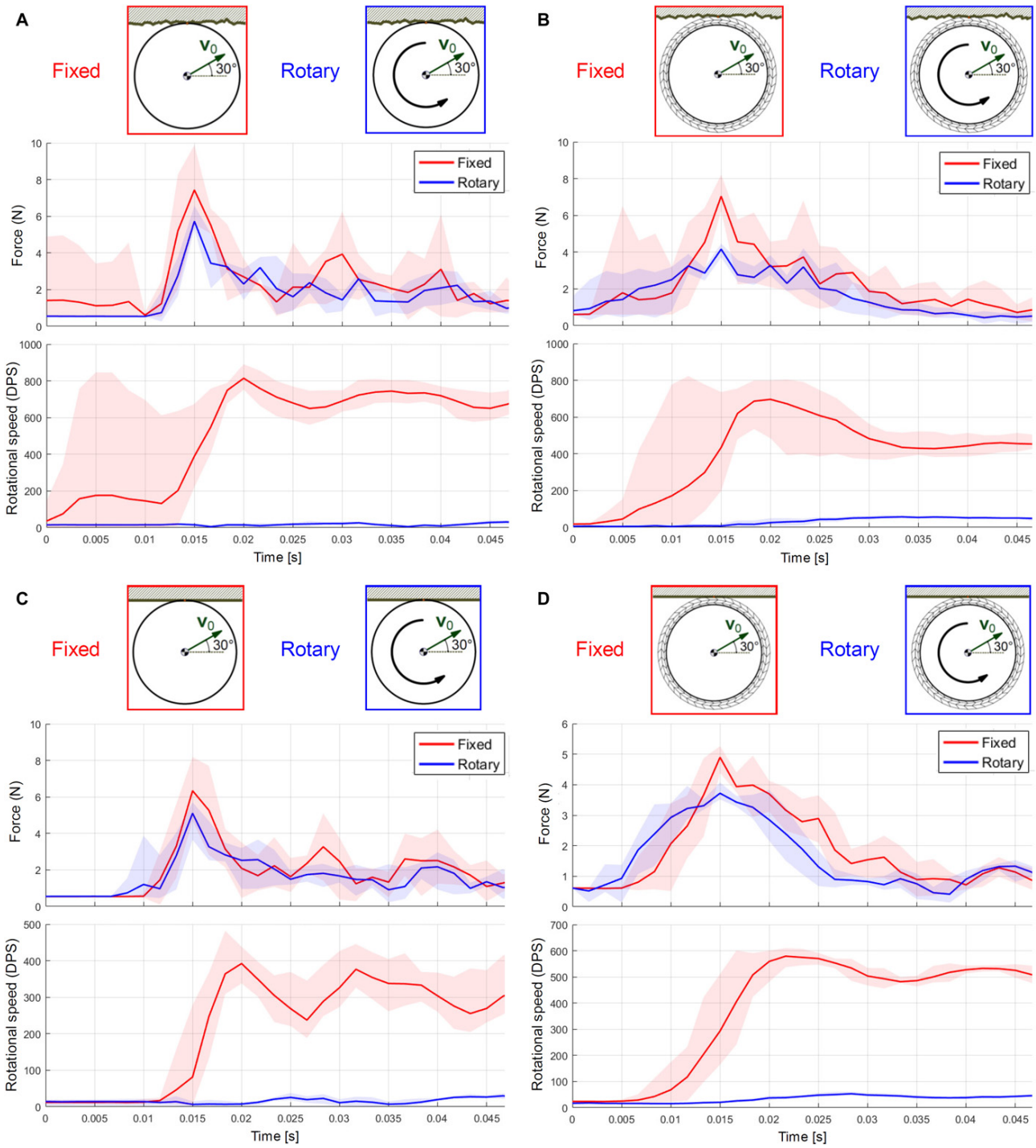

Figure 3.6: Force and angular speed profiles at a contact angle of 30° and impact speed of 1.2 m/s for fixed and rotary configurations on rough and smooth surfaces. The shaded areas represent the range of data (from five trials) corresponding to each collision. (**A**) Rough surface with naked protector. (**B**) Rough surface with origami protector. (**C**) Smooth surface with naked protector. (**D**) Smooth surface with origami protector. [2]

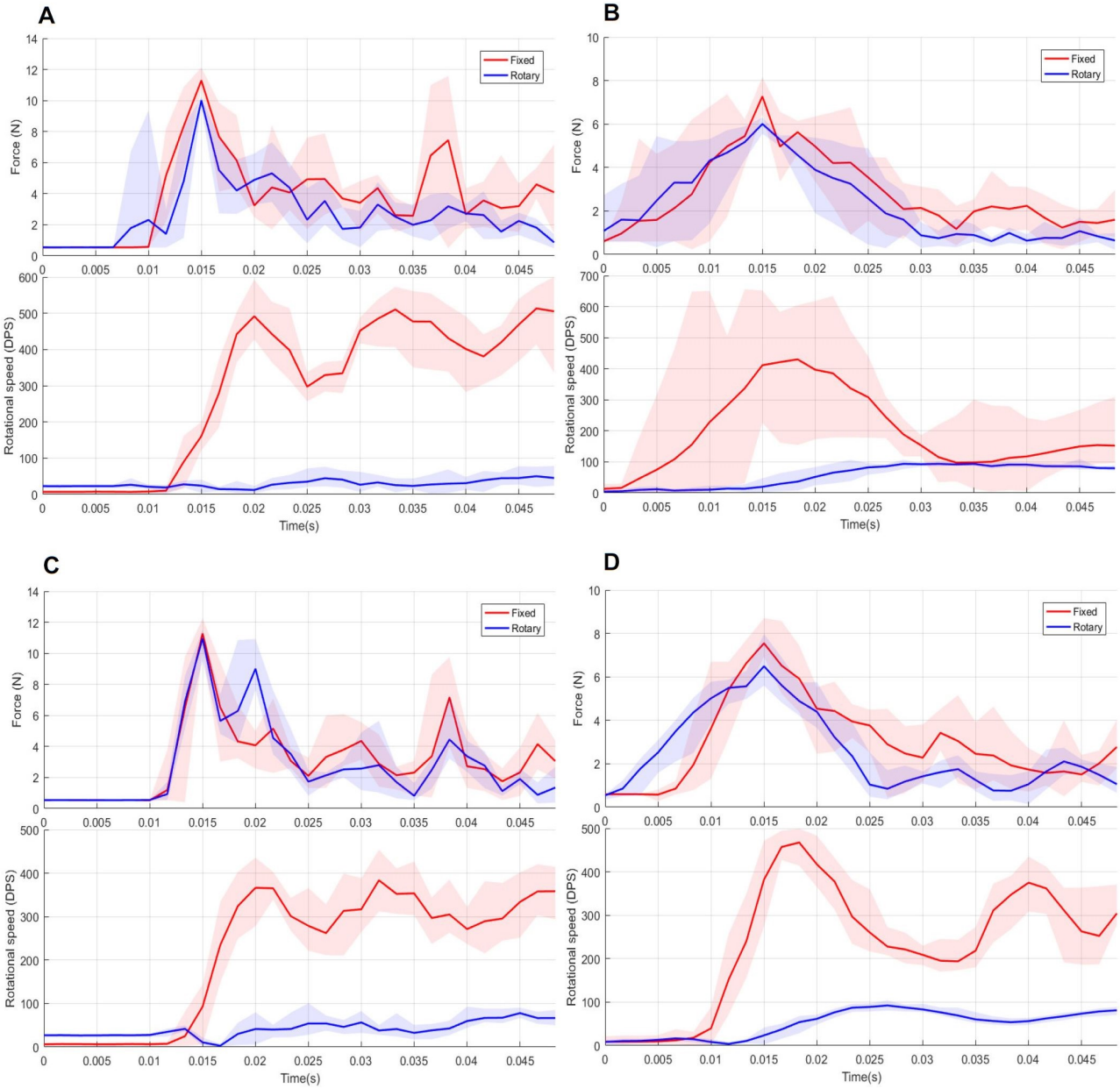

Figure 3.7: Force and angular speed profiles at a contact angle of 60° and impact speed of 1.2 m/s for fixed and rotary configurations on rough and smooth surfaces. The shaded areas represent the range of data (from five trials) corresponding to each collision. (**A**) Rough surface with naked protector. (**B**) Rough surface with origami protector. (**C**) Smooth surface with naked protector. (**D**) Smooth surface with origami protector. [2]

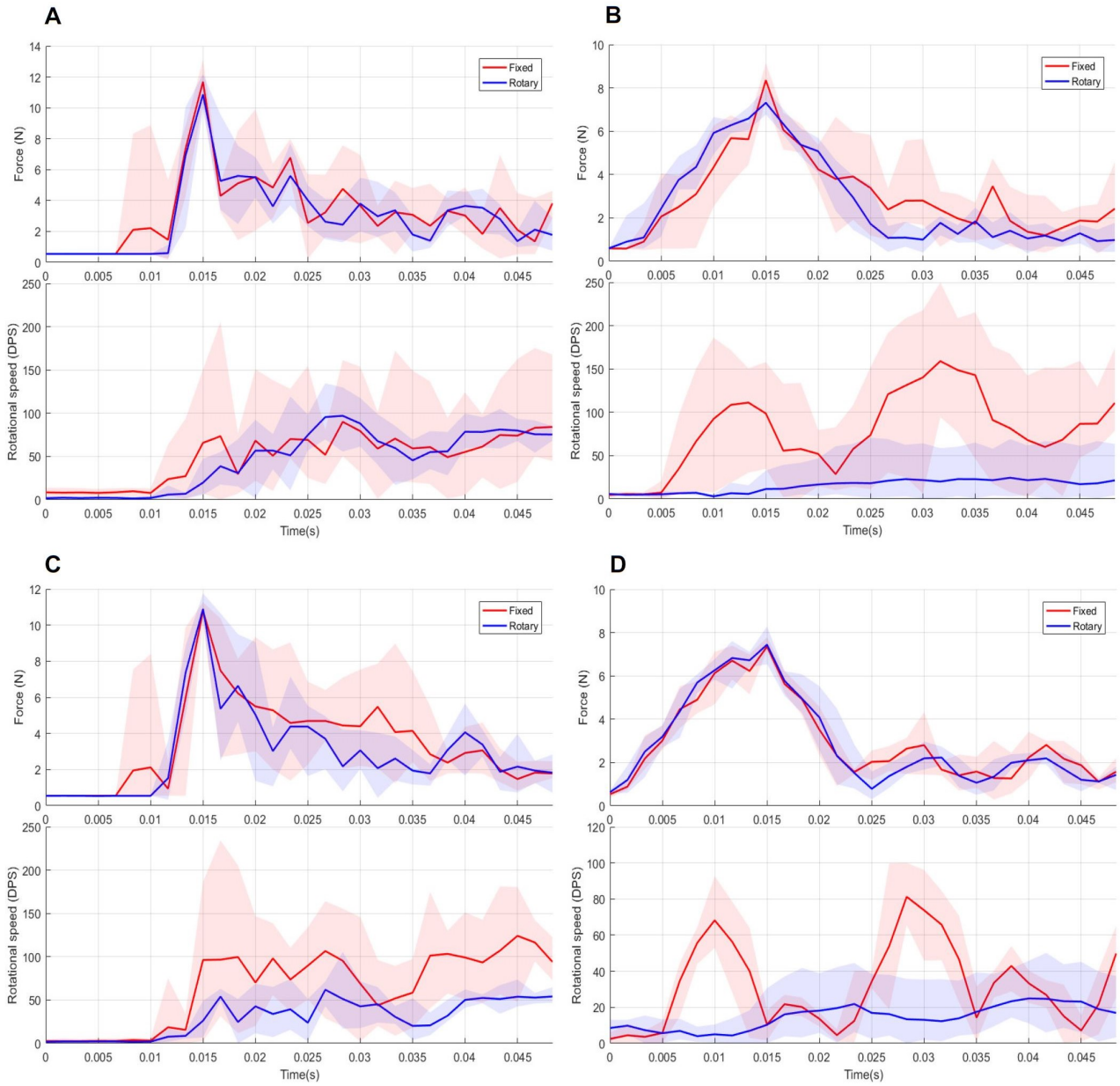

Figure 3.8: Force and angular speed profiles at a contact angle of 90° (normal collision) and impact speed of 1.2 m/s for fixed and rotary configurations on rough and smooth surfaces. The shaded areas represent the range of data (from five trials) corresponding to each collision. (**A**) Rough surface with naked protector. (**B**) Rough surface with origami protector. (**C**) Smooth surface with naked protector. (**D**) Smooth surface with origami protector. [2]

3.5 Discussion

By combining a ring-shaped origami structure and a passively rotating universal circular frame, we developed and demonstrated an effective protection system that could cushion impact to reduce the overall collision peak force experienced by the drone and decouple the induced yawing moment from the platform (Fig. 3.9A). Extensive experimental work in a range of impact angles on both smooth and rough surfaces demonstrated that the simultaneous exploitation of these two concepts is the most advantageous design configuration in terms of the overall impact resilience quality (Fig. 3.9B). In summary, origami-protected systems offered about 30% improvement in the peak impact force reduction compared with naked-protection systems in all tested collision scenarios. By changing the material thickness and perforation settings on a laser or blade cutter, this protector can be fabricated with different levels of stiffness for diverse applications, providing a range of softness levels and therefore a range of peak force reduction capacities appropriate for various missions and environments. For example, for low-speed hovering around people and animals or in an area with delicate and fragile obstacles, the origami ring must be scored or perforated more deeply; this may provide a relatively soft protective structure that makes the vehicle safe to fly around vulnerable obstacles.

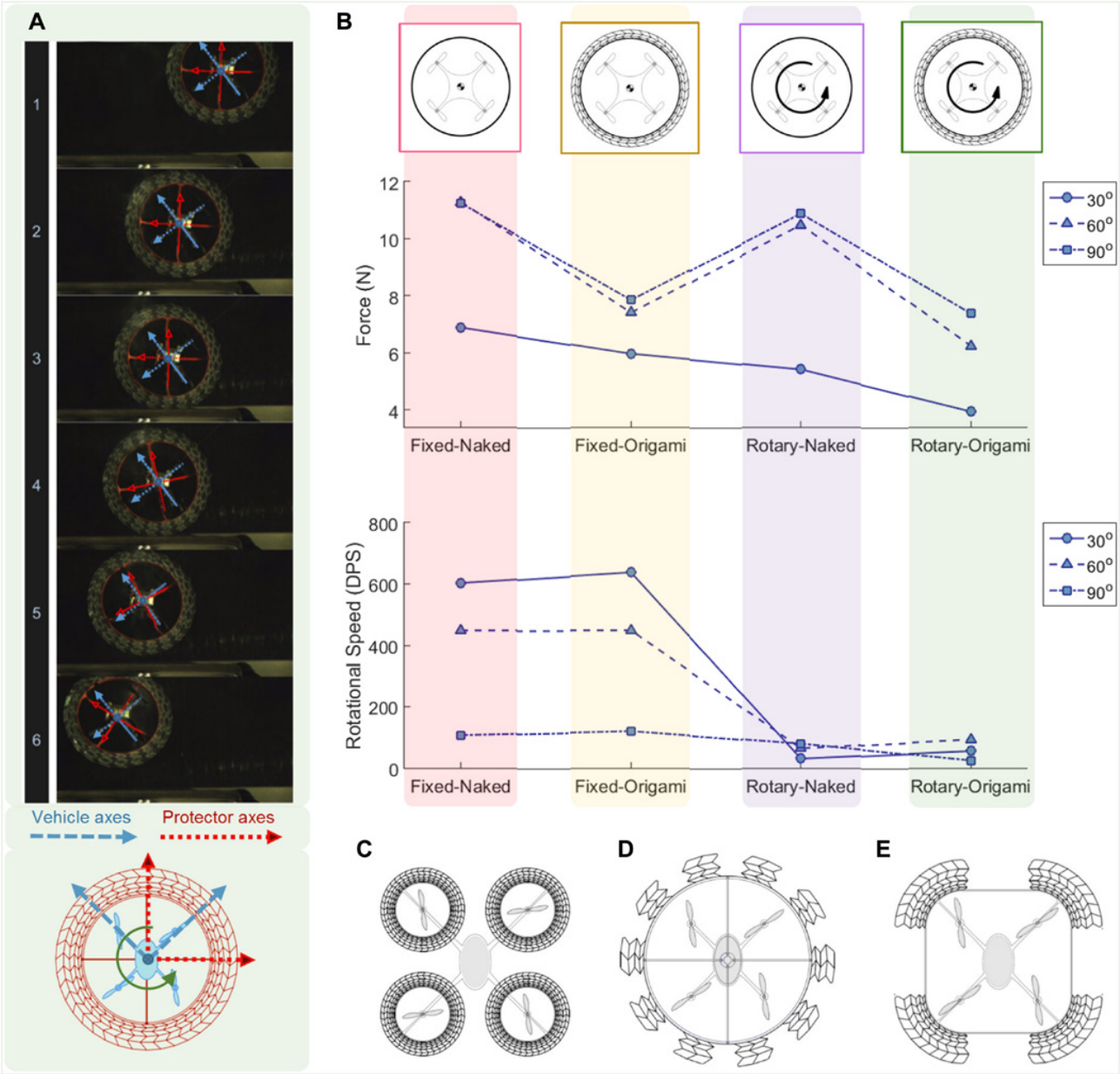

Figure 3.9: Analysis of experimental results. (**A**) Snapshots from high-speed camera videos for an oblique collision with a rough surface at a contact angle of 30 for the origami-protected system in the rotary configuration. Although the protector axes (red) rotate significantly upon impact to the surface, the orientation of the vehicle body axes remains almost invariant. (**B**) Summary of all results (values averaged between rough and smooth surfaces) demonstrating that the Rotary-Origami (Rotorigami) configuration is the most advantageous design configuration in terms of the overall impact resilience quality. (**C** to **E**) A series of conceptual designs for origami-protected aerial robots. [2]

Collision scenario				Experimental outputs		Improvement %	
Collision angle	Surface type	Impact cushion	Rotational DOF	Avg. peak force (N)	Avg. peak angular speed (DPS)	Average peak force	Average peak angular speed
30°	Rough	Naked	Fixed	7.43	814.26	0.00	0.00
			Rotary	5.73	30.98	22.92	96.20
		Origami	Fixed	7.04	696.50	5.26	14.46
			Rotary	4.16	57.02	44.02	93.00
	Smooth	Naked	Fixed	6.34	392.37	0.00	0.00
			Rotary	5.11	29.97	19.47	92.36
		Origami	Fixed	4.90	579.22	22.77	-47.62
			Rotary	3.72	53.37	41.35	86.40
60°	Rough	Naked	Fixed	11.29	513.21	0.00	0.00
			Rotary	10.01	50.23	11.38	90.21
		Origami	Fixed	7.27	430.29	35.61	16.16
			Rotary	6.00	93.75	46.84	81.73
	Smooth	Naked	Fixed	11.28	383.67	0.00	0.00
			Rotary	10.96	77.97	2.87	79.68
		Origami	Fixed	7.55	467.42	33.08	-21.83
			Rotary	6.49	92.29	42.46	75.95
90°	Rough	Naked	Fixed	11.69	90.04	0.00	0.00
			Rotary	10.86	97.02	7.12	-7.75
		Origami	Fixed	8.35	159.05	28.55	-76.64
			Rotary	7.31	24.45	37.44	72.84
	Smooth	Naked	Fixed	10.79	124.11	0.00	0.00
			Rotary	10.90	61.90	-0.99	50.12
		Origami	Fixed	7.35	81.27	31.87	34.51
			Rotary	7.44	24.93	31.01	79.92

Table 3.2: Summary of experimental results. [2]

3.6 Conclusion

The concept motivates future research on the utility of origami structures for enhancing the impact resilience of aerial and ground robotic vehicles. Future research will also need to incorporate dynamic and aerodynamic flight studies of the proposed concept. An important note is that, although the universal protective configuration improves the collision resilience of the vehicle by improving its response to the impact-yawing moment, there is a pitching moment increase penalty due to the larger moment arm for the imposed out-of-plane component of the impact force, compared with individual protective configuration. This increased pitching moment could cause the vehicle to tip over upon contact with the obstacle in the naked configurations. However, experiments showed (movies S1 and S4 in [2]) that, by equipping the vehicle with an origami ring, the tendency of the vehicle to pitch is substantially decreased. This improved stability could be explained as the combination of three factors: First, the origami ring considerably increases the mass moment of inertia of the vehicle with respect to the pitch axis; second, the aerodynamic resistance to pitch is larger for the origami-protected system due to its increased contact area; and finally, the peak impact force (and therefore its out-of-plane component) is smaller in the origami-protected configurations, leading to decreased tendency to tip over upon impact. Although this study was confined to a passive structure, it could be a starting point for developing advanced concepts with actively deployable origami structures capable of adjusting their stiffness for optimal contact with different surfaces. These structures could be fully folded (retracted) when the vehicle is not flying in a cluttered environment, that is, where it experiences a higher risk of collision to obstacles. This could lead to improved flight endurance. To enhance crash resilience, a second generation of this protective concept should include an active mechanism that protects the aerial robot in top and bottom collisions, without compromising the physical compactness of the vehicle. Furthermore, the same design principles can be extended and applied to other protected configurations, such as the individual propeller guards (Fig. 3.9C) and universal frames with modular origami impact cushions (Fig. 3.9, D and E). Future research may consider advanced structural concepts and further optimisation of the protective ring. This may include origami-inspired structures with cutout facets to decrease the structural mass of the system while preserving an appropriate level of structural performance.

This chapter will be concluded with key points of achievements and progress towards AAM.

- Rotorigami, a rotary origami protective system has been conceptually analysed, designed and developed. It is able to reduce normal impact forces upon collisions experienced by the UAV test platform and decouple yawing moments generated by tangential impact force.
- This concept demonstrates enhanced impact resilience and robustness for UAV opera-

tion in confined or cluttered environments, even though more research and experimental characterisation are required before this concept can be integrated in AAM and other real-world applications.

- Future works
  - Dynamic and aerodynamic studies of origami-based protective structure on UAV flight.
  - Physical interaction studies between UAV with origami-based protective structure and physical environments.
  - Origami-based protective structures can be in various designs, and different impact protection strategies are possible. Other concepts based on this work would be worth further investigation.

Chapter 4

Robust Landing for High Precision Aerial Manufacturing

4.1 Introduction

The work in this chapter was previously published in *Journal of Field Robotics* as "Bioinspired design of a landing system with soft shock absorbers for autonomous aerial robots" [5]

Unmanned aerial vehicles (UAVs) experience an ever-growing demand to perform reliably in real-world applications such as in post–disaster rescue, pollution monitoring, ecology, infrastructure inspection, and smart agriculture [97]. Small aerial robotic systems (in particular multirotor UAVs and related technologies) not only raise great interests in the robotics research community, but also lead to extensive development on the consumer market. One major focus of the current research in this field includes multifunctional robotic systems capable of flying, perching, gliding, climbing, and manipulation [98, 99] in unstructured outdoor environments. Seeking energy efficient locomotion, a jump-gliding miniature robot [100] is able to take off from ground using high–power jumping mechanisms [101] and uses gliding flight to effectively exploit the height gained after the boost for energy-efficient mobility. To overcome limited endurance and restrictions on current battery capacity of small-scale aerial robots, the Stanford Climbing and Aerial Maneuvering Platform [102] provides one promising solution which effectively combines directional attachment [103] and climbing [104] technologies. Other examples include adaptive morphology design principles for multimodal locomotion, such as the flying and walking robot, DALER, which is able to use its wings as legs to move on the ground, leading to effective and adaptive locomotion in different environments [105].

The efforts above explored a number of aerial robotic systems capable of perching and multimodal locomotion in unstructured environments. These studies demonstrated that dynamic

transition between flight and landing is an essential phase of a complete flight mission for autonomously piloted multimodel UAVs. Looking closely at landing systems for small multirotor UAVs, there are various landing gear designs for small UAVs for both scientific research and commercial production. However, most commercial designs have rigid frames (Figure 4.1a) aimed at vertical landing on flat surface of structured environments. In contrast to rigid frames widely used for commercial products, a number of interesting designs (Figure 4.1b-f) dedicated to simple linkage-based, movable landing gears have been explored recently. In these designs, either gravity-powered passive actuation mechanisms or motor-operated actuation mechanisms were used. While these systems are simple and lightweight, their fixed design with a rigid frame can lead to high impact forces on the UAV platform during landing, as well as blocked views of the onboard cameras and a largely restricted operating space for additional manipulators. Another challenge is that passive actuation mechanisms have difficulties to keep the UAVs in balance and remain upright with pure friction between grippers and structures.

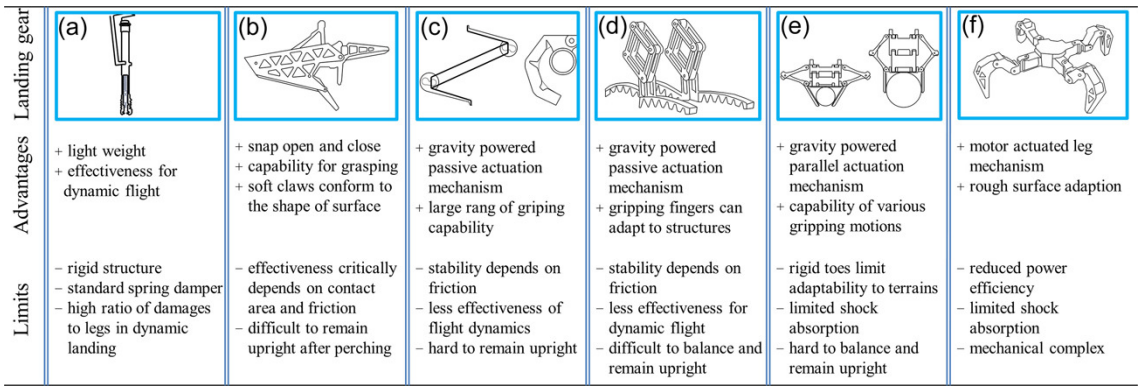

Figure 4.1: [5] **Designs of landing mechanisms for unmanned aerial vehicles especially for multirotor UAVs:** (**a**) The rigid landing gear with pneumatic shock absorber of DJI M100 [106]; (**b**) a snapping claw mechanism-based design with soft claws [107]; (**c**) a passive actuation mechanism with tendon driven claws [108]; (**d**) a four-bar linkage-based landing mechanism with compliant gripping digits [109]; (**e**) a Sarrus linage-based landing mechanism [110]; and (**f**) a landing mechanism based on legged robots [111]

Though high impact energy arise from dynamic landing, it was rarely taken into account in most of the designs of small-scale aerial robotic systems for real-world applications. To facilitate dynamic landing of aerial robots in various terrain structures, weather conditions, landing modes, and speeds, the landing mechanisms need to be adaptable to varied surface structures and functional for absorbing the impact energy. This is particularly important for dynamic landing maneuvers at fast speed, where the impact energy can reach high values that can damage the vehicle frame, sensitive cameras, and other electronics onboard. Further, the leg mechanisms have to be lightweight, given the limited payload capacity of these small aerial robots.

A recent cross-disciplinary study of adopting origami-folding technologies in engineering appli-

cations revealed that origami–inspired mechanisms based on foldable tessellations have great potential for energy absorption applications [112]. Examples include the thin-walled energy absorption devices [88, 113, 114] for transportation vehicles. Further, engineering principles were applied to the performance evaluation of foldable origami artefacts in artistic disciplines, leading to novel solutions to various engineering problems in real-world applications [115, 116, 117].

In this study, we first review biological landing mechanisms and explore the landing methods. Taking the biological landing techniques of the animal flyers as a source of inspiration, we abstract key functions of different types of legs and sensory systems to inform the design of a landing mechanism for small aerial robots such as the quadrotor UAV in this study. With the abstracted functions as guidance of practical design, this chapter proposes a new adaptive landing mechanism for autonomous aerial robots in a way of combining both advanced flight control based on an onboard visual sensory system and resilience of 3D printable soft shock absorbers and landing pads.

This chapter reports on design, development and experimental validation of an aerial robot with enhanced capability of performing dynamic landing by adopting visual–inertial guidance, adaptive landing mechanism which allows active morphing in accordance to flight phases and 3D–printed soft shock absorbers and soft landing pads. The ability to land on various structures can be of particular benefit to aerial manufacturing, especially in scenarios when high fidelity flight control is difficult or not, such as in windy conditions. Such a technique allows aerial construction agents to land on the surface of interest and complete required tasks in a stable manner.

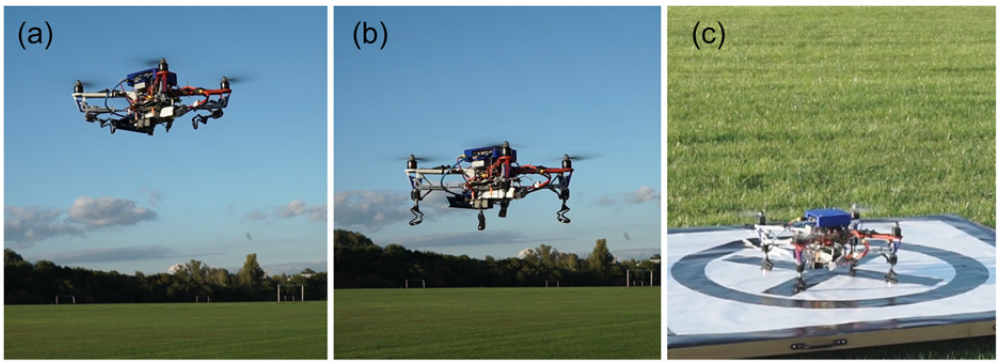

Figure 4.2: [5] **The autonomous quadrotor unmanned aerial vehicle, designed and built at the Aerial Robotics Lab with an one-degree-of-freedom retractable landing mechanism, performing an alighting maneuver:** (**a**) The pre-landing stable flight with retracted landing gear; (**b**) approaching the landing site with deployed landing gear, and (**c**) successful landing on the target

4.2 Bioinspired strategy and mechanism for autonomous landing

4.2.1 Brief review on biological principles during landing maneuvers

The study of natural systems revealed that evolutionary adaptation enables objects and processes in nature to be highly effective and robust [118, 119]. While the natural world evolves, its processes provides an extensive source of inspiration for creating comprehensive models of artificial systems that can mimic certain functions of their counterparts in nature [120]. The bioinspired design paradigm [67] and perching principles [121, 122] provide cross-disciplinary approaches to developing new devices by mimicking the natural world in the way of adopting concepts and principles in nature to solve engineering challenges.

Powered and unpowered flight is a unique form of locomotion used by living species such as insects, birds, and gliding mammals with various landing maneuvers being adopted by each [120]. Analysing and learning from the landing techniques of these animal flyers in nature can guide us to generate innovative ideas and concepts for the design of effective and robust landing systems of small aerial robots.

The overall landing strategy of animal flyers and gliders consists of comprehensive techniques, where behaviors are combined with sensing and actuation of wings, tail, legs, and other body structures. In nature, dynamic landing combines aerodynamics, multimodal sensing, and learning. This paper focuses on reviewing and extracting the physical aspects of the landing process, with particular attention to how legs can be designed to damp impact during the dynamic transition phases between flight and landing.

The following principles are identified to have promise for being implemented in the phases of landing maneuver of aerial robots.

1. Vision–based sensory system that guides the approach behaviors and mechanical adaptability for a robust landing on a target position on the surface.
2. Two–level adaptivity of the damping structure, with the first level to locally adapt to surface architecture and second level to damp the high impact.
3. Mechanical adaptability of the soft landing pad to the surface, using mechanical reflex in the design of the system without the need for surface sensing and complex control.

4.2.2 The strategy inspired by biological landing techniques

Here we present our general strategy to achieve dynamic landing in a representative landing scenario in the finals of the The Mohamed Bin Zayed International Robotics Challenge 2017 [123], which requires the UAV to land on a horizontal surface on top of a car moving at various speed. Inspired by the landing techniques of animal flyers, we have divided the mission of searching the moving platform and alighting the UAV on target into following steps:

1. Automatic take–off with a robust vision–based autopilot employing visual-inertial simultaneous localisation and mapping (SLAM) and model-predictive control (MPC).

2. Search for the landing pattern on moving vehicle with the use of visual detection and tracking.

3. Approach the landing pattern on top of the moving vehicle with accurate tracking and motion prediction.

4. Landing the UAV with the use of a retractable landing system employing 3D printable shock absorbers and soft landing pads with magnets.

With the principles learned from animal flyers, our general approach to the landing maneuvers of the quadrotor UAV consists of three corresponding phases (as illustrated in Figure 4.3), including (a) approaching, (b) alighting, and (c) stabilising. This operation process will enable transitions from high speed descending flight to a short drop by combining robust visual guidance and mechanical resilience of the proposed leg mechanism.

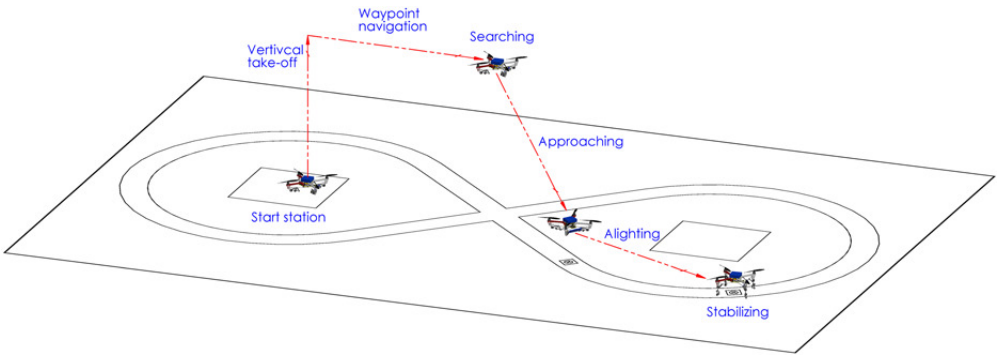

Figure 4.3: [5] **General strategy for alighting the UAV on the horizontal surface of a moving target (in the flight arena (1:1000) of The Mohamed Bin Zayed International Robotics Challenge competition).** (**a**) Before taking off: The robot in stationary mode at the start location. (**b**) After vertical take-off: The robot reaches a certain height and starts searching the moving target with landing pattern on top. (**c**) The robot approaches the moving vehicle with automated motion prediction. (**d**) Landing mechanism deploys from the folded stage, allowing soft contact between the landing pads and the target. (**e**) The landing pads bend upwards and the shock absorber deforms for energy absorption, while the the magnets on the landing pads attach to the platform to stabilise the UAV while as the target is still moving

4.3 System overview

The constrains for optimising the design of an autonomous UAV include the total weight of subsystems, high-performance onboard computer, and visual sensors (which are essential for facilitate the UAV to complete the mission in outdoor environment), as well as the size of landing pattern placed on top of the roof of the moving vehicle. With consideration of these constraints, we have used DJI F450 as the quadrotor platform and a modular open-architecture for the electronic hardware, to allow quick reconfiguration of the layout to match the details of MBZIRC2017 mission requirements. A 3D model of the UAV developed in this study with a DJI F450 frame is illustrated in Figure 4.5. Here, we took the DJI Flamewheel F450, since its frame arms are made of ultra strength material, providing crashworthiness and the flexibility and abundant assemble space for further customisation. The technical data of the UAV platform and customised specifications are listed in Table 1.

Characteristics	MBZIRC requirements	Design specifications
Flight time	20 min	10 min
Range	>100 x 60 m	2 km
Max size of the UAV	1.2 x 1.2 x 0.5 m	0.85 x 0.85 x 0.2 m
Max speed of the UAV	30 km/hr	70–80 km/hr
Weight of the UAV	NA	2 kg

Figure 4.4: [5] The MBZIRC requirements and technical data of the customised aerial robot

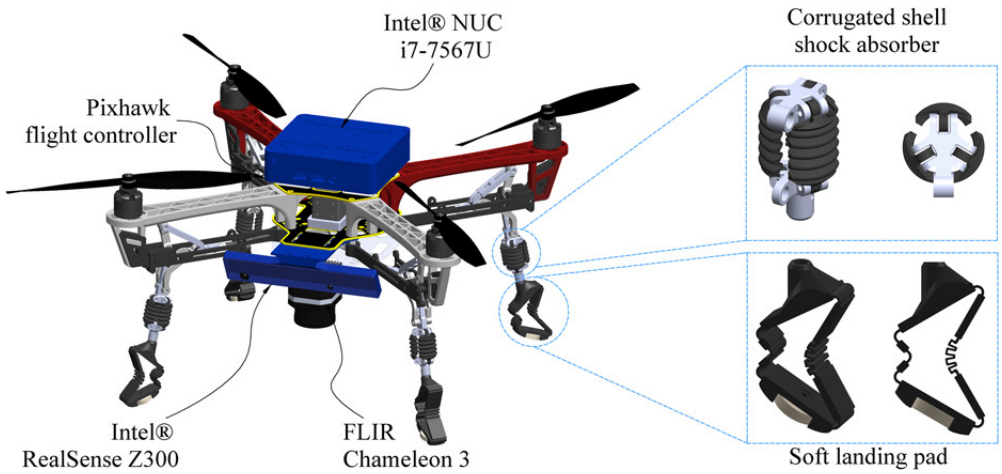

Figure 4.5: [5] Three-dimensional model of the integrated quadrotor micro aerial vehicle with retractable landing gear, 3D printable shock absorbers, Intel NUCi7, Intel Realsense visual sensor, and an additional downward looking camera

4.3.1 Retractable leg mechanism with 3D printable soft shock absorbers

One of the critical challenge for UAVs is the limited payload capacity comparing to those large-scale fixed wing drones and ground robots. It is always important to keep subsystems for small UAVs to be lightweight to maintain proper trade-off between flight duration and the added payload. To complete the MBZIRC2017 mission described in Section 4.22 within the shortest time, the quadrotor UAV requires aggressive and agile movement during the searching and approaching phases of the whole process in Figure 4.3. Taking all requirements above into account, we propose a new retractable leg mechanism which allows the UAV to fold its legs thus maneuver in a compact configuration in the same way of animal flyers while hovering and dynamic maneuvering.

The penultimate stage-one of the most important tasks of the challenge in MBZIRC2017 is to land the UAV on a moving target. This flight transition phase requires not only precise real-time tracking, following, and estimating of the moving target with the visual sensory system,

but also mechanical robustness, allowing the UAV to alight on the horizontal surface and absorb shock energy associated with high-speed landing as the UAV makes contact with the moving target.

Inspired by the biological landing techniques of animal flyers, particularly the use of extensible elements in their legs for shock absorption, this paper presents a new design of shock absorber with corrugated shell mechanisms (Figure 4.5) that can be fabricated with advanced multimaterial additive manufacturing techniques [124, 125]. In this study, we selected Onyx, a printable composite material, made from combining tough nylon with microcarbon fiber reinforcement [126] and the flexible ultimaker thermoplastic polyurethane (TPU) 95A [127].

For design, FEA simulation, statics characterisation of shock absorbers and landing pads, and design of actuation mechanism for retractable landing system, detailed analysis can be found in author's publication in [5].

4.3.2 UAV control and navigation

We describe the software components for intelligence of the UAV in Figure 4.6. We follow a fairly classic decomposition of first estimating the state of the UAV, as well as the landing target followed by a controller to track a setpoint which in turn is determined by a higher level guidance and state machine. Furthermore, we split the controller into a high-level Model-Predictive Controller, we developed ourselves and a low-level attitude and thrust controller employing an off-the-shelf Pixhawk module.

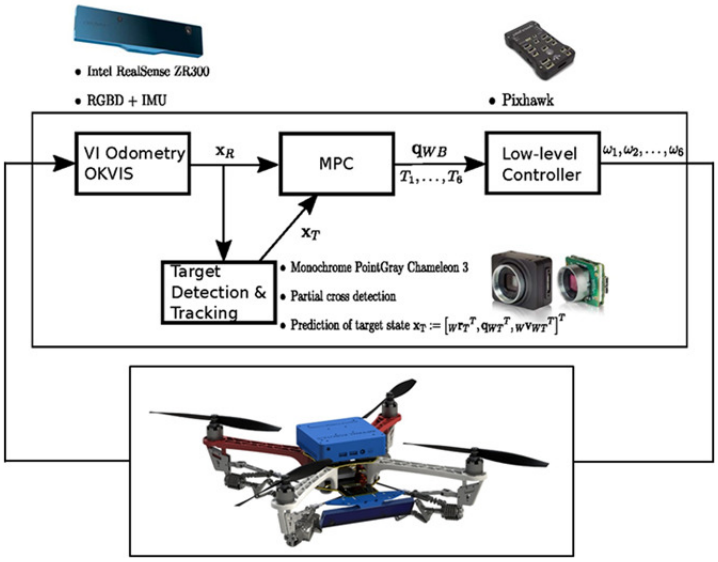

Figure 4.6: [5] Open keyframe-based visual-inertial SLAM [79] is used in combination with the Intel RealSense ZR300 for the visual-inertial odometry estimation. The UAV state x_R is parsed to the target detection and tracking module. A monochrome FLIR Chameleon 3 is used for the detection. The target state x_T and the UAV state x_R are further used in the MPC to generate a reference quaternion q_{WB} and reference thrusts $T_1, ..., T_6$ for the low-level controller. A Pixhawk is used to convert the reference inputs to PWM signals $\omega_1, ..., \omega_6$. IMU: inertial measurement unit; UAV: unmanned aerial vehicle; MPC: model-predictive control; PWM: Pulse Width Modulation

State estimation

As a basis for localisation of the UAV, we employ an extension of open keyframe-based visual-inertial SLAM [79]. We have modified the formulation of the underlying estimator to use the RGB-D (Red, Green, Blue-Depth)-inertial camera RealSense ZR300 instead of a stereo camera with integrated IMU. The underlying principle is inspired by ORB-SLAM 2 [128], where we use depth measurements when available to create landmark observations in a virtual stereo camera.

To detect and track the moving target pattern as specified by the MBZIRC organisers, we use a downward-looking fisheye camera and assume the visual-inertial pose using OKVIS is known accurately enough. Initial detection follows a fairly straightforward, but highly optimised vision-processing pipeline to extract a quadrangle in the undistorted image, estimating the relative pose and verifying the appearance of the the landing pattern template. To track the target, even if it is only partly visible, we formulated an extended Kalman filter using a model of the dynamics in 3D space that assumes constant linear velocity and constant orientation in the prediction step. The update step then uses observations of the tracked keypoints of the pattern.

Controller

The UAV tracks the desired set-point using a cascaded control approach. Our high-level controller follows a linear MPC approach to output tilt angles and thrust to track position and yaw angle. This is then followed by the low-level attitude and thrust controller, where we employ an off-the-shelf Pixhawk board. Finally, a high-level logic determines the current state set-point. First, commanding the drone to hover at the cross point of the figure-eight track (where we expect the vehicle with the landing pattern to pass through), secondly, following it to initiate descent, once the UAV has properly caught up. We describe this logic in more detail in Figure 4.7 depicting a flowchart with operating modes including the strategies in the case of target detection loss.

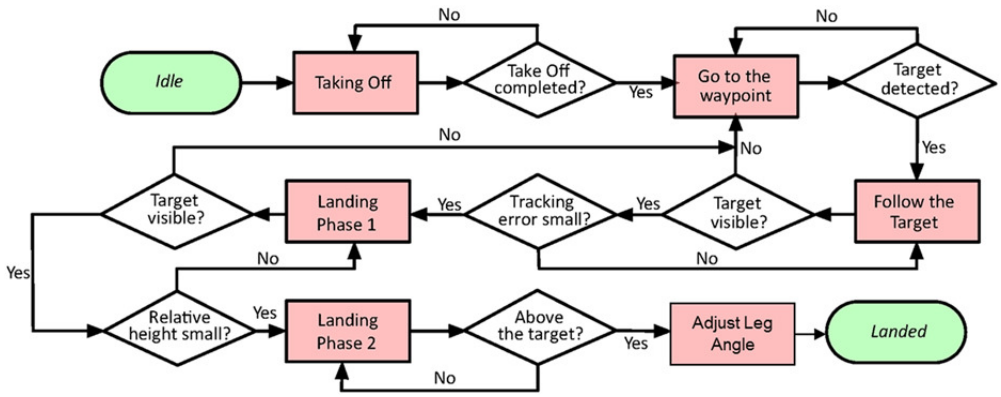

Figure 4.7: [5] Flowchart indicating the transition between the various operating modes

4.4 Experimental validation of dynamic landing on various structures

The impact accelerations experienced by the quadrotor UAV have been recorded using ADXL377 accelerometer breakout board, which is rigidly attached to the frame of the quadrotor. The acceleration data stream has three axes: [X, Y, Z] and they were recorded at a rate of 250 Hz. The accelerometer implements 10-bit analog output with 200 g as an output range. This gives us a resolution approximately at 3.83 m/s^2 of the recorded acceleration. In the indoor environment, we implemented the landing tests in a Vicon motion capture system which is used as a source for position and landing velocity data, at 100 Hz, for the UAV control system. Following the indoor characterisation, we then implemented the control and navigation system in Section 4.3 in the field tests.

4.4.1 Vertical landing on static convex, concave and flat structures with shock absorbers and landing pads

Similar to many flyers in the animal kingdom that employ a short-drop approach in the final stage of landing, the UAV cuts out the thrust and implements a free drop towards the surface structure to complete the last stage of a vertical landing once it has received the landing command. Before the short drop has been initiated, the quadrotor is hovering directly above the target position.

For the purpose of demonstrating the reconfigurability of the 1- DOF leg actuation mechanism and the adaptability to varied surface structure, landing tests have been implemented on three different structures including a horizontal flat plate, a convex surface structure, and a concave surface structure.

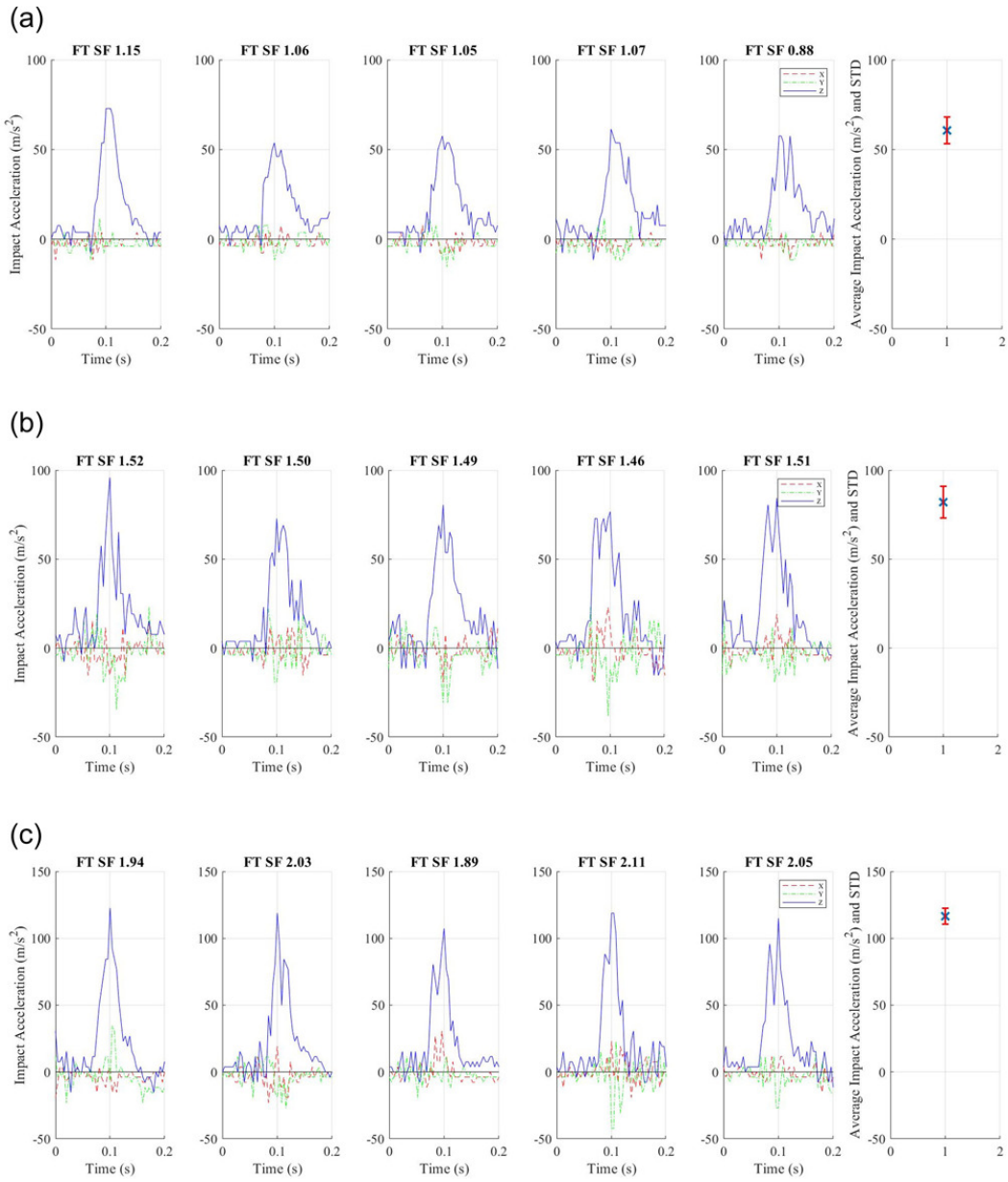

Figure 4.8: [5] **Landing tests on static horizontal flat surface structure: Peak, average, and standard deviations of impact accelerations of five tests with average vertical landing speed at** (**a**) 1.04, (**b**) 1.50, and (**c**) 2.06m/s. FT: flat surface; SF: soft leg

Vertical landing tests were first implemented with horizontal flat surface structure, which was designed according to the specifications given by the challenge of MBZIRC2017. As shown in the experimental results in Figure 4.8, both X and Y components of the acceleration remained close to zero as the landing is completed with a vertical short drop. Contrarily, we observed two peaks, negative and positive, acceleration in Z-axis direction. Instead of having spontaneous and sudden impacts, the soft shock absorbers dissipate the impact energy by spreading the impact shock over time. The duration of these positive peaks can be seen to last about 50 ms rather than one spike which lasts a mere millisecond for hard impact/ crash [129].

Following the landing tests on flat surface structure, the landing system was further tested on both convex and concave surface structures respectively.

As illustrated in Figure 4.9, a metal sheet of 1mm thickness was deformed to a convex surface structure of which the top section is a half cylinder with R1 = 254mm. With this convex surface structure, the leg mechanism is open at 82.5 to adapt to the geometry. For these landing tests, we adopted same landing strategy and the quadrotor first hovers on the top of the target position and then completes the landing with a short drop. A total of 15 tests were implemented with average vertical touchdown speeds at 1.14, 1.62, and 1.99 m/s. The impact acceleration of these tests are reported in Figure 4.10. It reveals that both X and Y components of the acceleration increase as the robot tilts laterally to adapt to the surface structure, but they remained relatively small comparing to the component at Z direction.

For the tests on concave structure, a metal sheet was deformed to a concave surface structure in Figure 4.11 with R2 = 654 mm. With this convex surface structure, the leg mechanism is open at 110 to adapt to the geometry. A total of 15 vertical landing tests were implemented with average vertical touchdown speeds at 1.03, 1.57, and 1.81 m/s, respectively. The impact acceleration of these tests is reported in Figure 4.12.

It reveals that in the landing tests on convex and concave surface structures, both X and Y components of the acceleration also increase but remained relatively small comparing to the component at Z direction.

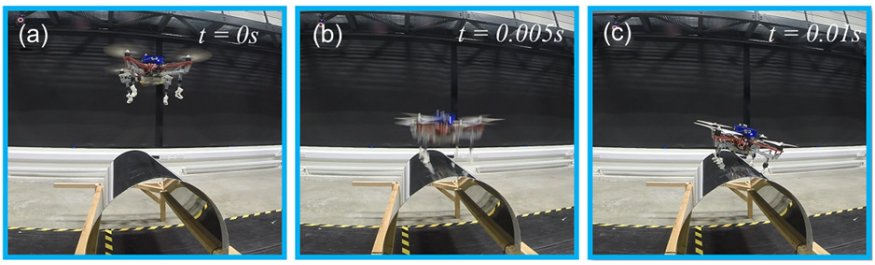

Figure 4.9: [5] **Indoor landing on convex surface structure with landing pad printed using thermoplastic polyurethane (TPU) 95A:** (**a**) Hovering above the target position and start drop, (**b**) touchdown at t = 0.005 s, and (**c**) stabilized at t = 0.01 s

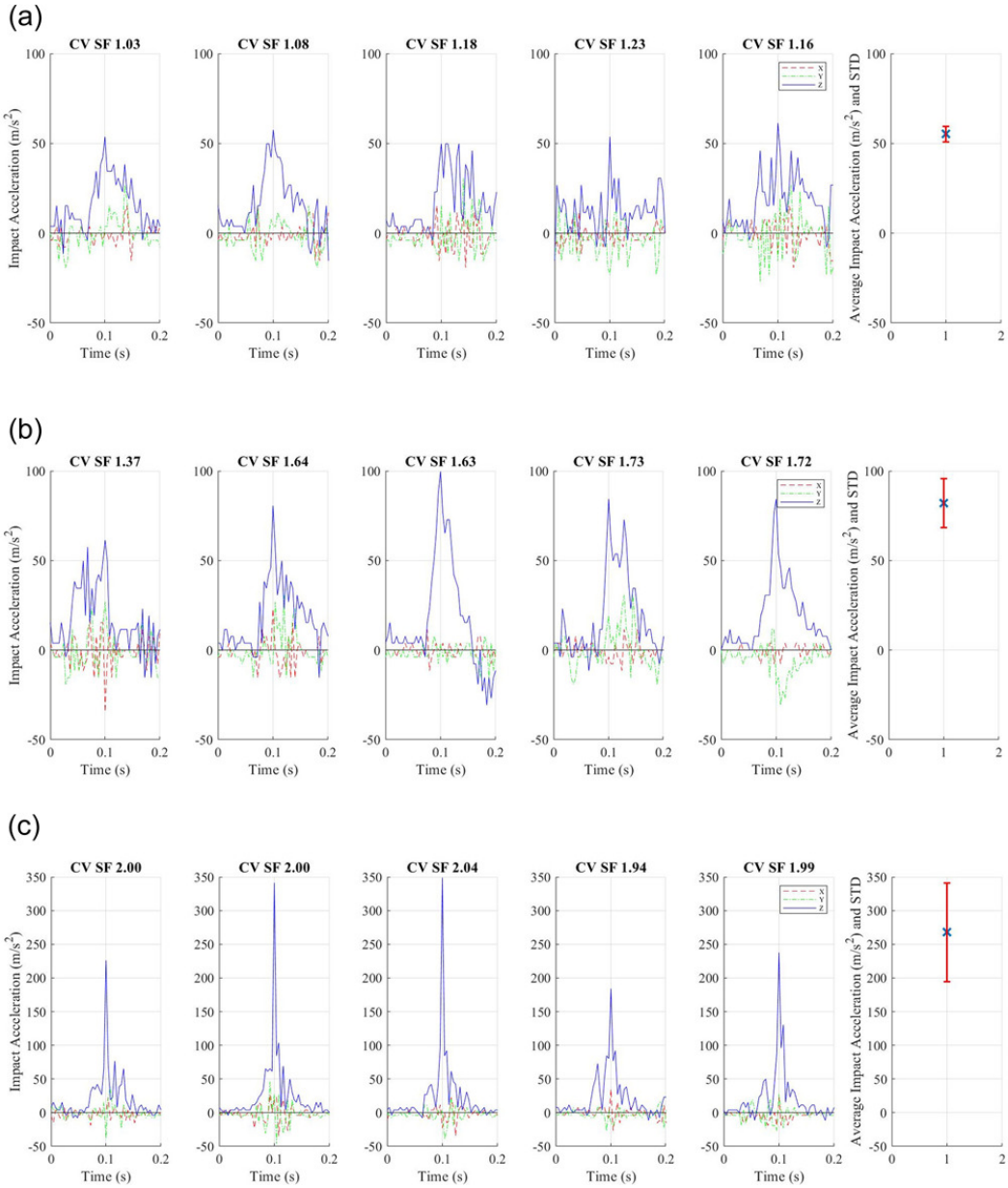

Figure 4.10: [5] **Impact acceleration of landing tests on static convex surface structure: Peak, average, and standard deviations of impact accelerations of five tests with average vertical landing speeds at** (**a**) 1.14, (**b**) 1.62, and (**c**) 1.99 m/s. CV: convex surface; SF: soft leg

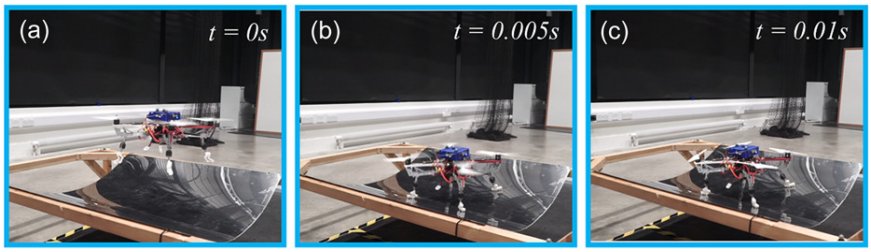

Figure 4.11: [5] **Indoor landing on concave surface structure with landing pad printed using TPU95A material:** (**a**) Hovering above the target position and start short drop, (**b**) touchdown at t = 0.005 s, and (**c**) stabilised at t = 0.01 s

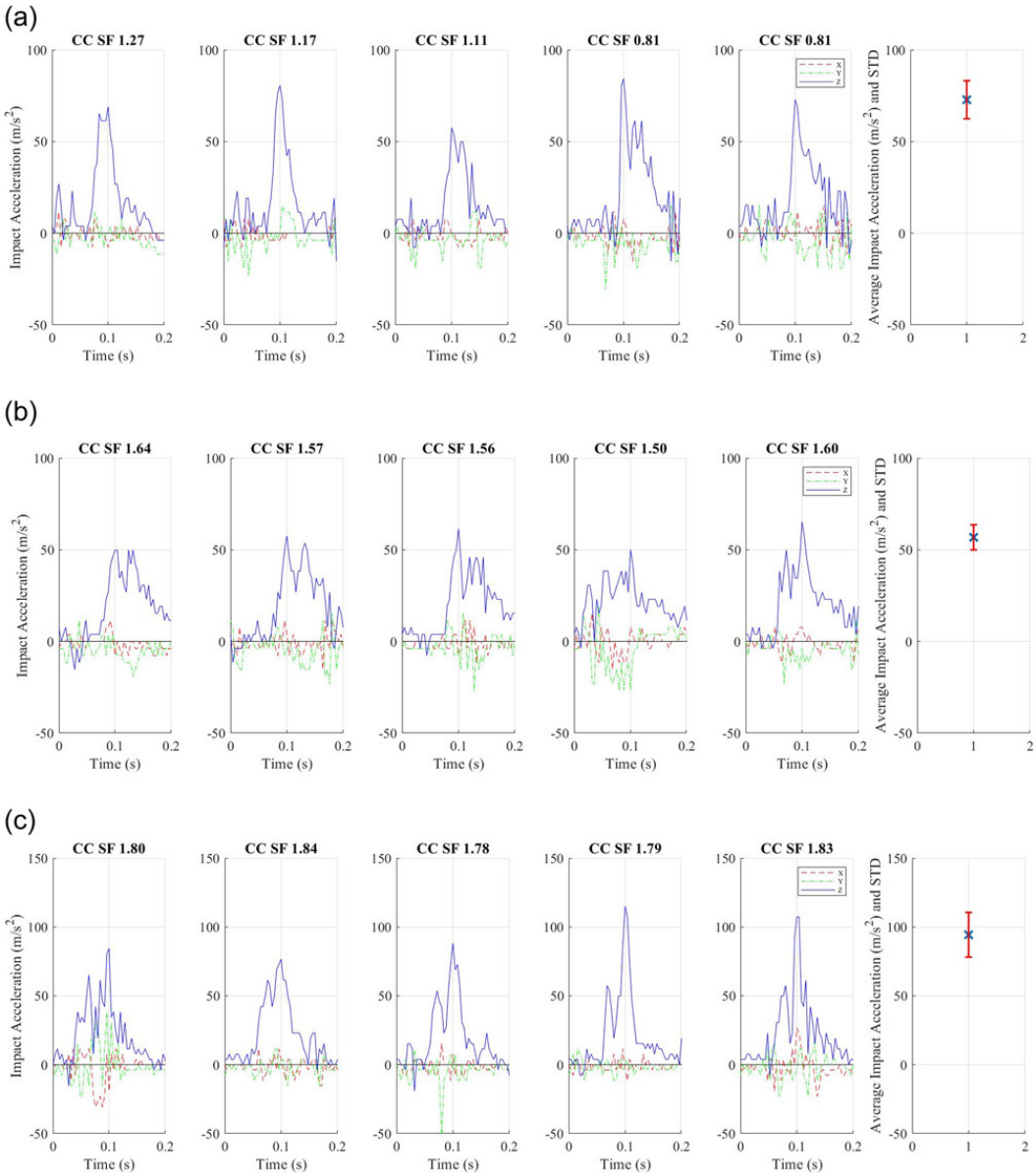

Figure 4.12: [5] **Impact acceleration of landing tests on static concave surface structure: Peak, average, and standard deviations of impact accelerations of five tests with average vertical landing speeds at** (**a**) 1.03, (**b**) 1.57, and (**c**) 1.81 m/s. CC: concave surface; SF: soft leg

4.4.2 Vertical landing on static horizontal flat surface with rigid legs

Apart from the landing tests above, we further implemented same landing tests on horizontal flat surface with rigid legs. This allows us to characterise the design significance of the proposed soft shock absorbers by comparing the peak accelerations in the landing direction during a series of landings at different speed.

For the landing tests with rigid legs with average vertical touchdown speeds at 1.04, 1.55, and 2.08 m/s, we implemented 15 times landing tests five times for each touchdown speed. The peak acceleration of each test is reported in Figure 4.13.

Because the vertical impact acceleration is markedly larger compared to the anterior-posterior or medial-lateral components, the peak value of vertical components has been used for characterising the capacity of absorbing impact energy.

The peak impact accelerations of all landing tests with soft shock absorbers are compared against that of rigid legs at average touchdown speeds referenced at 1, 1.5, and 2.0m/s. The statistic box plot in Figure 4.21 explicitly illustrates that the vertical peak impact acceleration is significantly reduced in all tests with the soft shock absorbers and landing pads. Only those peak accelerations of landing tests on convex structure with average speed at 1.99 m/s are higher than the other cases. The exceptional individual tests results with high value could be cases where the absorber were broken due to bending motions that exceeded the design ranges.

The comparison of results using soft legs and rigid legs reveals that the soft leg mechanism proposed in this paper is capable of reducing the peak acceleration by 270 m/s^2, therefore dissipating 540N impact force at maximum (given the UAV mass of 2kg and Newton's second law).

From principle of momentum conservation, a quadrotor colliding with a static metal plate is expected to bounce up (given that its coefficient of restitution is greater that zero and not all of its kinetic energy is dissipated). However, this is not the case here because of the magnets mounted on the flat panel of the landing pad which touches the surface structure at first. Only small upward acceleration can be seen throughout all tests as the magnets is used to holding the UAV on the target position, which is particularly important while the target is moving.

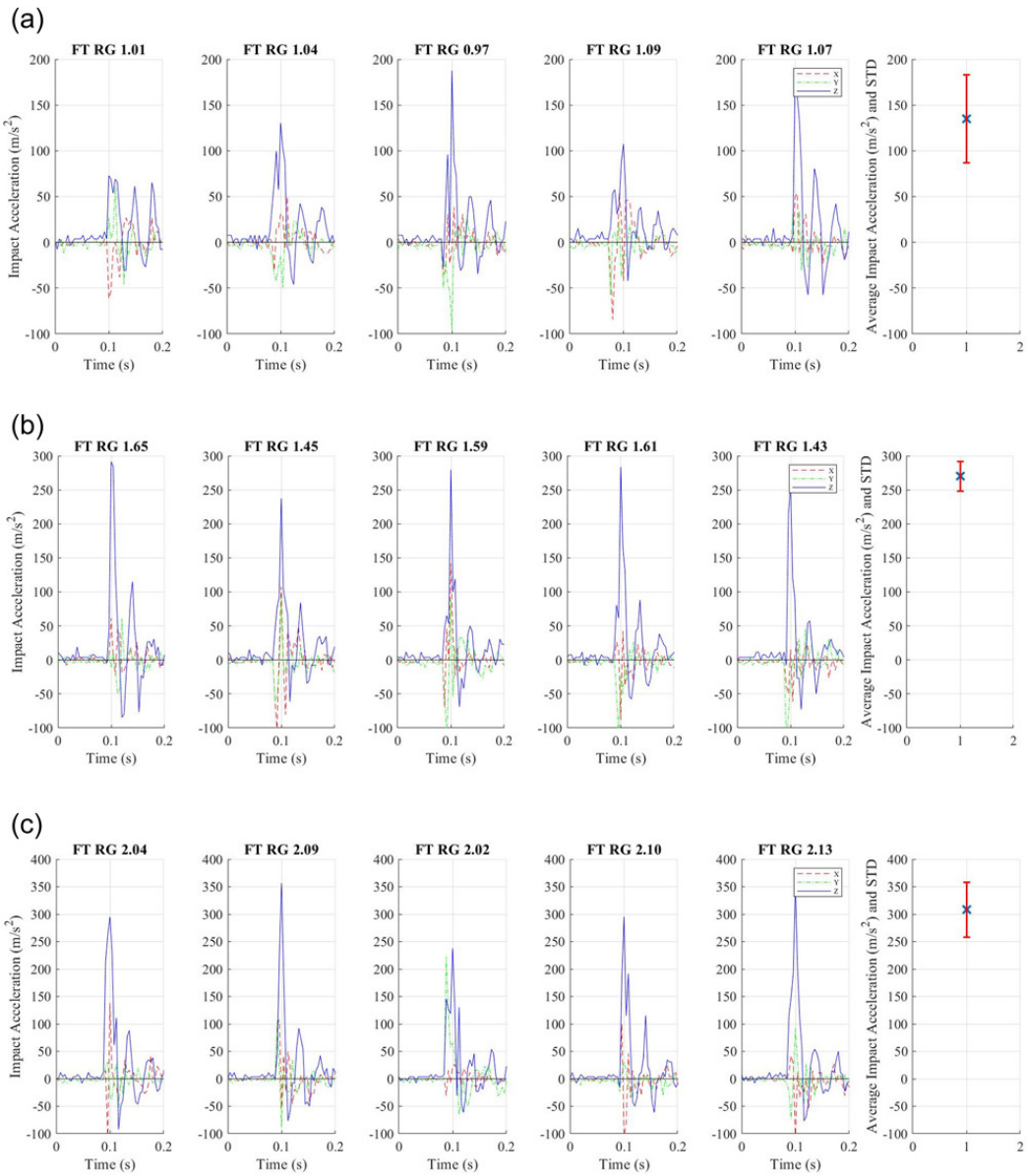

Figure 4.13: [5] **Impact acceleration of landing tests on static flat steel plate: Peak, average and standard deviations of impact accelerations of five tests with average vertical landing speeds at** (**a**) 1.04, (**b**) 1.55, and (**c**) 2.08 m/s. FT: flat surface; RG: rigid legs

4.4.3 Field tests of dynamic landing on grassy field and a moving target

Experimental results in this section were obtained in outdoor field tests where the UAV landed on a grassy field as well as a moving target that suits MBZIRC17 requirements. In the scenarios of vertical landing the UAV on dry grass ground and where the magnets are not necessary, the soft landing pad with magnets were removed and only the Sarrus shock absorbers were used to absorb the impact energy during landing (Figure 4.14).

The tests results for vertical landing on grassy ground with average vertical landing speeds at 1.09, 1.44, and 2.10 m/s are illustrated in Figure 4.16. Comparing to the results of landing tests, in which magnets are used to allow the UAV to grip to the structure, in Subsection 4.4.2, the landing tests on grassy field show larger lateral impact accelerations. This means that accelerations in the direction of X- and Y-axis may not be negligible in certain landing scenarios. This can induce bounce off from landing surface and thus drop from the landing target moving at a high speed. Thus, gripping techniques are essential to allow the UAV to firmly grip to the target position.

To successfully land on a moving target, the UAV has to actively track the target while adjusting its attitude to achieve certain landing velocity. The outdoor flight tests were carried out following the mission strategy introduced in Section 4.2. The decomposed trajectories in X-, Y- and Z-axis directions in the global coordinate frame of one of the implemented flight tests are plot in Figure 4.15b. The autonomous tracking, approaching, and landing phases on the moving target in the experiment is illustrated in Figure 4.15c, in which the frames are taken with equal intervals in between. The varied poses of the quadrotor demonstrate the maneuvers in response to the speed of the moving target on the ground. As a result, the UAV may land at a non-vertical angle and experience shock in axes other than the Z-axis in the acceleration data. However, similar trend as the indoor experiment can be observed from the data obtained in experimental tests.

In terms of peak vertical impact acceleration, all 1 m/s velocity setpoint impact tests, both indoor and outdoor, yield approximately 50 m/s^2 or below for the peak impact shocks. In 1.5m/s impact scenarios, peak vertical impact shocks are about 80 and 100 m/s^2 for indoor and outdoor tests respectively. At highest impact velocity scenario, we observed values within 100m/s^2 for indoor tests and within 150m/s^2 for outdoor tests. This range of impact shocks is arguably within the safe region for quadrotor UAV [129]. The UAV does not show any sign of damage and deterioration of performance (Figure 4.17, Figure 4.18, and Figure 4.19).

With the impact acceleration obtained from the accelerometer during the outdoor landing tests, the impact force during the touchdown moment of landing can be then calculated given the mass of the robot is known. The impact forces of selected outdoor tests where the robot did not bounce off with reference landing speed at 1, 1.5, and 2 m/s are reported in Figure 4.20, where maximum impact forces corresponding to each landing speed of the outdoor tests are 95N at 1 m/s, 197N at 1.5 m/s, and 295N at 2 m/s.

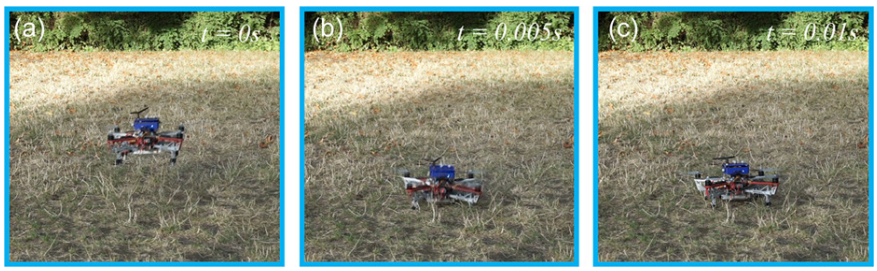

Figure 4.14: [5] **Outdoor landing on grassy field with Sarrus shock absorber:** (**a**) Hovering above the target position and start drop, (**b**) touchdown at t = 0.005 s, and (**c**) stabilised at t = 0.01 s. The UAV landing at a speed higher than 1 m/s always bounces off the ground after first touchdown. Gripping techniques are essential for stabilising the UAV. UAV: unmanned aerial vehicle

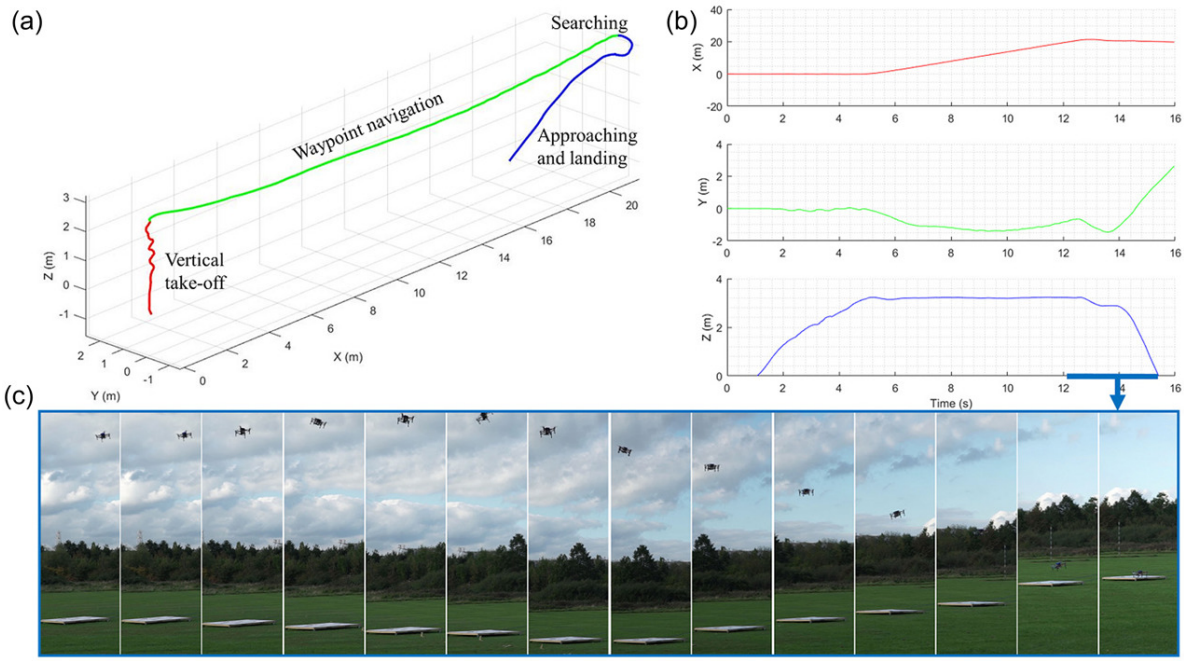

Figure 4.15: [5] **Outdoor test following the mission for landing on the moving target.** (**a**) Three dimensional trajectory of the planned mission, (**b**) decomposed trajectories of the approaching and landing phases, and (**c**) flight maneuver sequence during the transition phase of landing on moving target

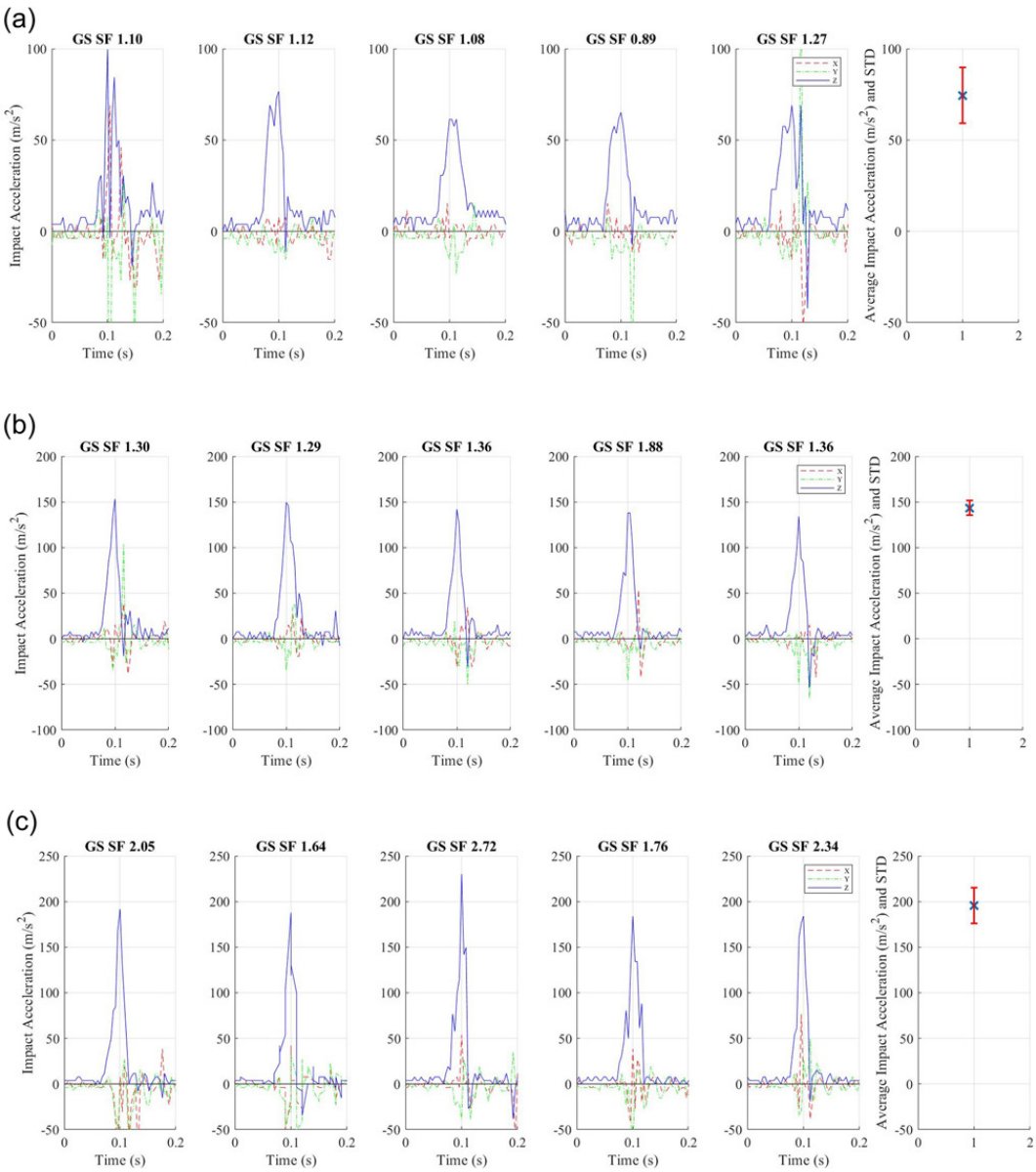

Figure 4.16: [5] **Impact acceleration of landing tests on grassy field: Peak, average, and standard deviations of impact accelerations of five tests with average vertical landing speed at** (**a**) 1.09, (**b**) 1.44, and (**c**) 2.10 m/s. GS: grassy field; SF: soft leg

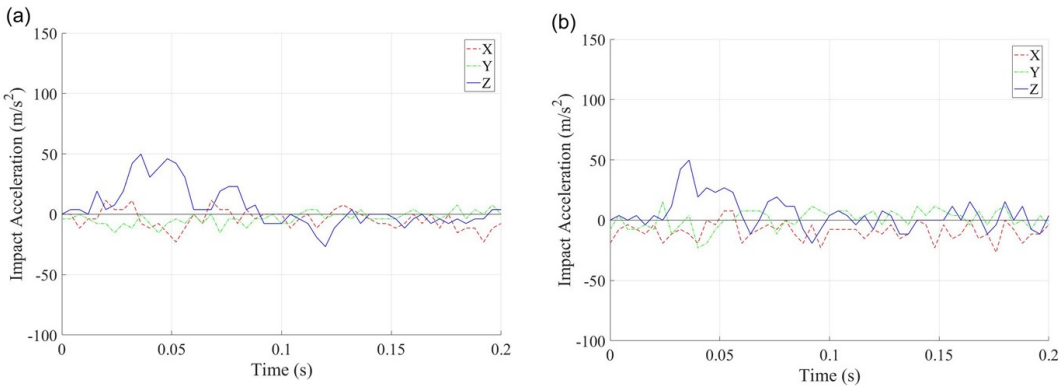

Figure 4.17: [5] **Outdoor tests on the moving target: Impact acceleration for 1 m/s velocity setpoint upon impact.** (**a**) landing test 1 and (**b**) landing test 2

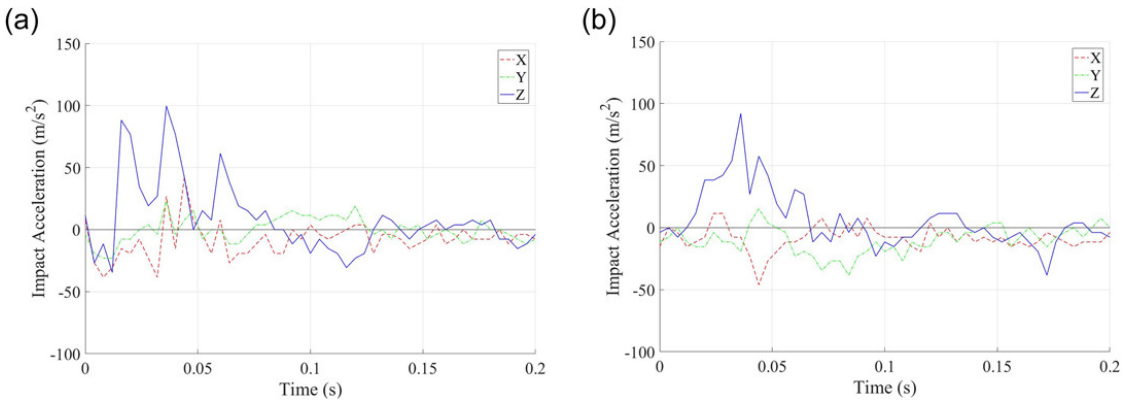

Figure 4.18: [5] **Outdoor tests on the moving target: Impact acceleration for 1.5 m/s velocity setpoint upon impact.** (**a**) landing test 1 and (**b**) landing test 2

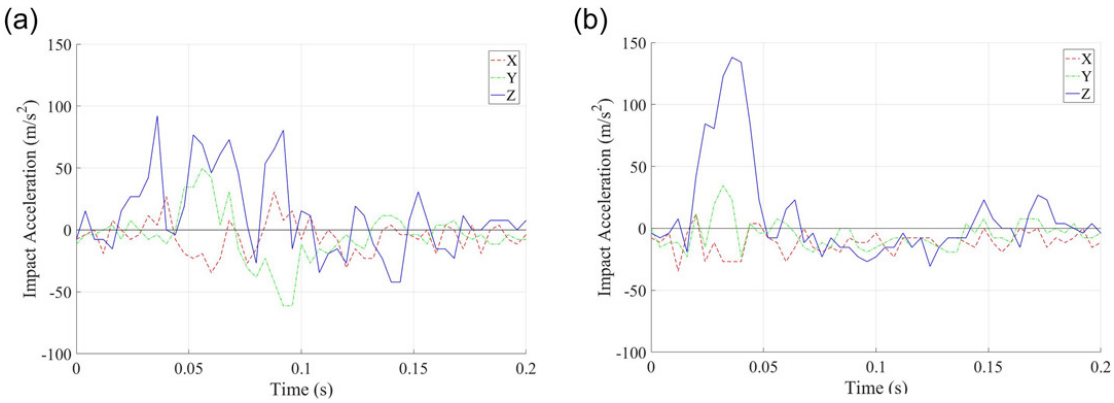

Figure 4.19: [5] **Outdoor tests on the moving target: Impact acceleration for 2 m/s velocity setpoint upon impact.** (**a**) landing test 1 and (**b**) landing test 2

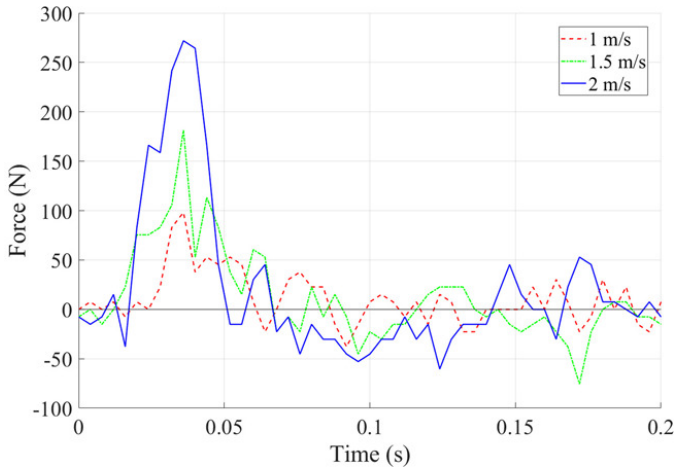

Figure 4.20: [5] The evolution over the time of the contact force occurring during dynamic landing on moving target

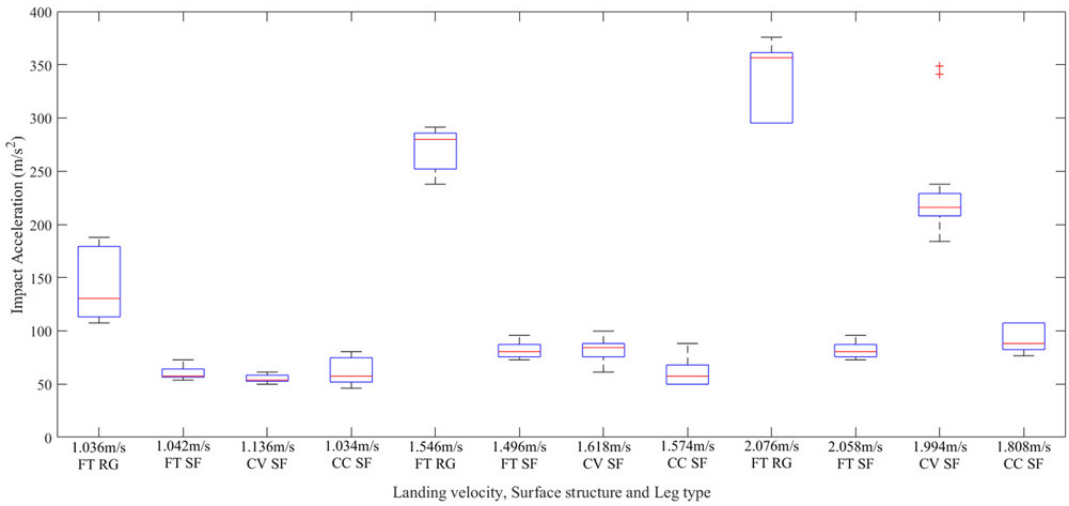

Figure 4.21: [5] Comparison of the peak impact accelerations of landing tests on varied surface structures with different landing speeds: the peak acceleration is reduced on average by 65, 200, and 270 m/s^2 with reference landing speeds at 1, 1.5, and 2.0 m/s. CC: concave surface; CV: convex surface; FT: flat surface; RG: rigid legs; SF: soft legs

4.5 Conclusion

The work in this paper explores bioinspired solutions in landing gear morphology of small aerial robots to achieve dynamic landing on varied surface structures as well as moving targets. Taking inspiration of animal flyers in nature, a landing strategy based on robust visual-inertial guidance and physical leg mechanism adaptability is adopted to safely land the aerial robot at a target position in real world applications. Built on the inspire-abstract-implement bioinspired design paradigm, a retractable leg system with a 1-DOF actuation mechanism was designed and realised for leg morphing in various flight modes of aerial robots mimicking the function of leg

extension in animal flyers. A morphable shell mechanism was designed as a compliant module of a new shock absorber based on the Sarrus linkage and shell structure-based living hinges were used in the design of a foldable landing pad. Both the morphing shell mechanism and the landing pad were then fabricated with advanced multimaterial additive manufacturing process and flexible thermoplastic filaments. This leads to inherent softness of the shock absorber and landing pad which provide two-level adaptivity of the landing system. The first level adapts locally to surface architectures and the second level damps the high impact energy in the final stage of dynamic landing. The design of the origami-inspired corrugated shell mechanism and the soft landing pad were analysed using FEA simulations and were evaluated with dynamic mechanical testing of 3D printed samples. The conceptual design of using 3D printable modules for dissipating impact energy during landing maneuvers of small aerial robots were verified with vertical landing tests on three types of static surface structures, including horizontal flat surface, convex and concave surface structures, and outdoor flight tests on grassy field and a moving target. The peak accelerations during these landing tests of the aerial robot with the proposed shock absorbers and landing pads were benchmarked against the conventional landing gears with a rigid structure. The test results revealed that the aerial robot with the 3D printed soft shock absorbers is capable of adapting to varied surface structures and vertical speeds up to 2 m/s without deterioration of performance. The total impact force that can be absorbed by the novel landing mechanism is up to 540N.

This study is an example of Aerial Biorobotics which bridges research on aerial robotics control and navigation with biologically inspired mechanical resilience and morphological adaptation, showing innovative solutions to challenges in aerial robotic engineering.

Compared to commercially available simple dampers with a similar size, the proposed Sarrus shock-absorber has a relatively larger stroke, while the soft materials used for printing the corrugated shell mechanism provide flexibility of bending for local adaptability to surface structure. Further, the 3D printable shock absorber can be customised and directly 3D printed according to needs of application. A comprehensive modeling with consideration of the additive manufacturing process and various filament materials will lead to better understanding of the design principles for 3D printable functional mechanical systems for aerial robots

This chapter will be concluded with key points of achievements and progress towards AAM.

- The challenge of dynamic landing of autonomous aerial robot flights has been investigated, and a potential solution has been proposed, characterised and demonstrated.
- Bioinspired landing system with soft shock absorbers for aerial robots is able to reduce impact energy upon dynamic landing, and its adaptive landing mechanism allows local adaptability to various structures and terrains.

- Current applications of UAVs may be mostly limited to flat landing surfaces, relatively low landing speeds and non–challenging environments, however, as UAV applications are becoming more advanced, dynamic landing and ability to land on various non–flat surfaces are predicted to be sought after.
- Current AAM demonstration shown in chapter 6 does not require this capability yet as it is carried on a tightly controlled working environment, however, the author expects this capability to useful for future aerial manufacturing with aerial robots.
- Future works
  - Better understanding in 3D printing materials characteristics and additive manufacturing process will significantly contribute to the ability to produce 3D printed components with desired properties.
  - Mechanical and electronic design can be modified and improved to suit required applications.

Chapter 5

Tensile Anchoring for Precise Operation in Windy Conditions

5.1 Introduction

The work in this chapter was previously published in *IEEE/RSJ International Conference on Intelligent Robots and Systems (IROS)* with the title "SpiderMAV: Perching and stabilizing micro aerial vehicles with bio-inspired tensile anchoring systems" [6]

Unmanned Aerial Vehicles (UAVs) have become an extensively developed part of the robotics landscape in the past few years [97]. However, the flight time of these aerial robots is severely limited to tens of minutes given current battery technology, and the maintenance of a stable position for precise operation is challenging, particularly in outdoor environment and partial failure conditions of the system. These main challenges [130] greatly reduce the efficacy of using UAVs to implement tasks requiring greater endurance and accuracy [30], such as close range aerial inspection and infrastructure reparation.

For the energy problem, perching has emerged as one of the most promising solutions, allowing aerial robots to operate in a low energy state between flights. A large number of concepts for perching UAVs have been presented, from both academic and commercial sources. This has included a variety of systems based on conventional pressure adhesives [131], spines and linkages for UAVs at smaller and larger scales respectively. Van der Waals dry adhesives [132, 133] employed in perching systems allow UAVs to stick to smooth vertical surfaces, while other systems employ spines to engage asperities on rough vertical wall surfaces [134]. Linkage based perching systems are capable of mimicking the agile perching behaviours of birds and allow both landing and take-off [135]. These systems all rely on a fixed attachment point, but the use multiple attach points with actuated tethers to allow a larger workspace within a movable

operating envelope has been demonstrated in mobile camera systems such as SpyderCam.

All these systems shown that aerial robots using limited sensing and computation have benefited from perching to fixed structures, relying on mechanical intelligence to make up computational deficits at the small scale [119]. It has also demonstrated that perching can help to enhance capabilities of multimodal robots moving in cluttered environments [136, 137].

Figure 5.1: [6] The SpiderMAV: bio-inspired aerial robotic system capable of prolonged endurance and stabilised operations.

In parallel with approaches relying on mechanical intelligence, both sensing hardware and software control methods have also been continuously explored to enhance stabilisation of UAVs in both manoeuvring and hovering. Complex estimation architectures with numerous embedded inertial sensors and cameras have proliferated for the purpose of stabilising system performance in various flight modes [138, 81], and novel algorithms have been explored based on various platforms. These developments have included the stability margin evaluation method [139], and the use of inertial optical flow in a nonlinear controller [140]. More recently, strategies for maintaining the controllability of quadrocopters under partial failure conditions have been investigated [89, 141, 142], leading to possible solutions for multicopter fault tolerant control design [143].

In nature, a spider is able to create large tensile structures between fixed attachments for predation and protection, and even passive flight (ballooning [144]). Taking inspiration [67] from this approach of using of tensile anchors for creating structures by the silk producing arachnids (Caerostris darwini), this paper proposes an innovative concept for developing multimodal aerial robotic systems with perching and stabilising capabilities, enabling solutions to

critical challenges in UAVs operation such as endurance and accurate station keeping.

This concept has been accepted for the final round of the UAE's Drones For Good competition in 2017, and it has since been further developed to improve its perching and stabilising capabilities for UAV applications, AAM included. Section 5.2 describes geometric and static design principles with screw theory and Grassmann line geometry. Section 5.3 presents the design of modularised perching and stabilising systems, that are able to launch multiple tensile anchors onto distant structures, and its control system. Section 5.4 discusses the results from the stabilisation tests . Finally, Section 5.5 concludes and discusses open questions and perspectives in this new trend of research.

5.2 Geometric and static principles for design and analysis

5.2.1 The SpiderMAV

The SpiderMAV proposed in this paper is an aerial robotic system inspired biologically by the web construction and locomotion capabilities of arachnids such as Darwins Bark spider who spins strands of silk to build bridge lines up to 25 meters. While the spiders spray silk strands which drift on air current, the artificial SpiderMAV shoots threaded anchors from launchers allowing the anchor to reach fixed structures (ground bases) from distance and attach to targeted positions. The other end of each thread is wound around a spool mounted onto the UAV and can be actively coiled and uncoiled by the actuated spool. With threads in tension, the UAV in the absence of rotor thrusts is a platform suspended by a number of threads and subjects to pure forces including tensile forces provided by threads and the passive gravity. By rotating spools and adjusting length of each threads, the suspended UAV changes its position and orientation and manoeuvres in the 3D space. This type of thread/cable suspended systems are also referred to as wire/tendon-driven parallel mechanisms [145, 146], with characteristics such as large workspace, high load transmission and dynamic capacities useful in various applications.

5.2.2 Geometric modelling

Without losing generality, a schematic diagram of the SpiderMAV in its station holding mode is illustrated in figure 5.2 where the system has n rotors and m threaded anchors attached to fixed structure. The point A_i denotes the target position where an anchor attached while the point Bi (i = 1,2,...,m) $B_i(i = 1, 2, \ldots, m)$ denotes the other end of each thread connected to the multicopter frame. Here we assuming attaching points Bi on the frame are located in a

single plane Pp which is perpendicular to rotational axes of rotors $R_j (j = 1, 2, \ldots, n)$ Taking principle of kinematics, these points on both fixed structure and multicopter frame connecting the thread are equivalents of spherical joints.

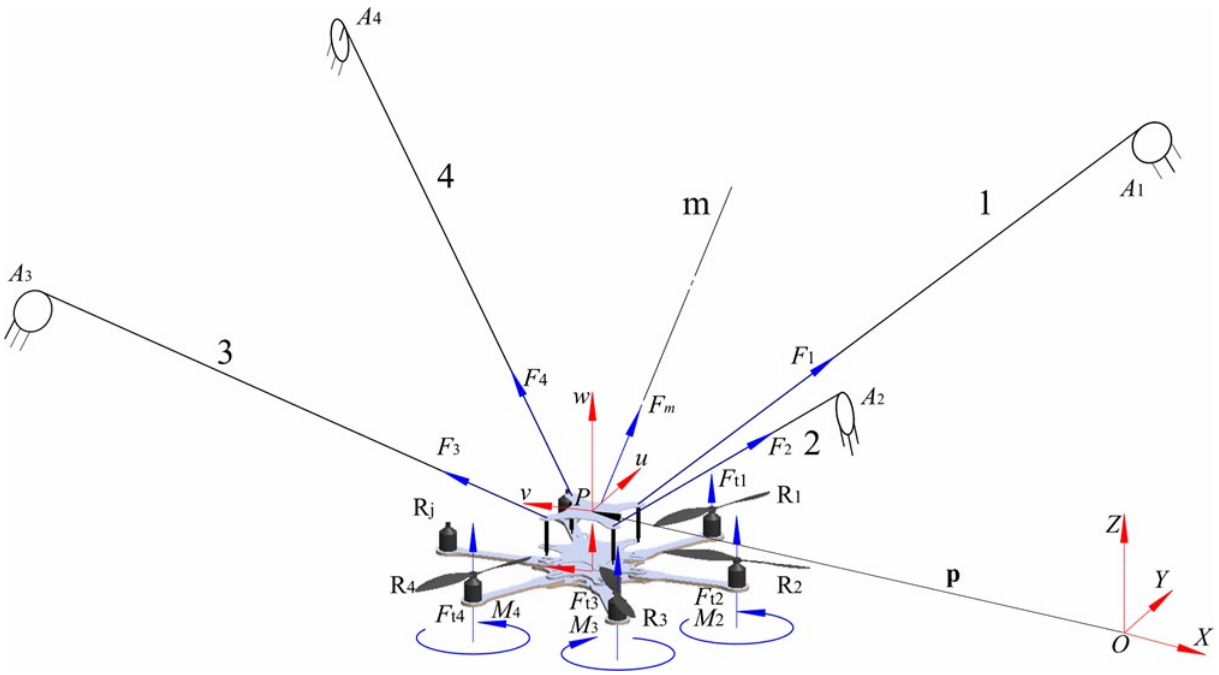

Figure 5.2: [6] Schematic representation of a station holding mode of the SpiderMAV.

An inertia reference frame O-XYZ is attached to the fixed structure. A moving reference frame P-uvw is attached to the frame with origin P located in the plane $\prod_p$ and the w-axis perpendicular to the plane. For each thread, a local coordinate frame B_i-$x_i y_i z_i$ is set up with its origin attached at point B_i by shifting reference frame P-uvw. Further, a local reference frame Q-$x'y'z'$ is attached to the mass center Q of the multicopter with z'-axis aligning to w-axis by shifting reference frame P-uvw. For each rotor, a local coordinate frame R_j-$x_j y_j z_j$ is set up by shifting reference frame Q-$x'y'z'$ and attaching the origin at point R_j.

In figure 5.2, position vectors of string attaching points B_i and rotor mounting points R_i expressed in the moving reference frame P-uvw are

$$\begin{cases} \mathbf{b}_i = \begin{bmatrix} x_i & y_i & 0 \end{bmatrix}^{\mathrm{T}} \\ \mathbf{r}_j = \begin{bmatrix} x_j & y_j & h \end{bmatrix}^{\mathrm{T}} \end{cases} \tag{5.1}$$

where geometric parameters x_i, y_i, x_j, y_j and h are constants for a certain design of the SpiderMAV since the threads attaching points and the rotors mounting points are relative invariant on the multicopter frame.

5.2.3 The wrench matrix of the system in a stabilised mode

When the strings are in tension, ith cable is considered as a line segment and the thread applies a pure force F_i along the vector pointing from point B_i to A_i. The pure force F_i expressed in the local reference frame B_i-$x_i y_i z_i$ is a zero pitch screw vector (representing a system in which only forces are being applied to the centre of mass and without any torque) which is defined as

$$\mathbf{F}_i = t_i \begin{bmatrix} a_i & b_i & c_i & 0 & 0 & 0 \end{bmatrix}^{\mathrm{T}} \tag{5.2}$$

where t_i is the magnitude of the tensile force F_i and $[a_i, b_i, c_i]^{\mathrm{T}}$ is the unit vector pointing from points B_i to A_i. For thrust forces generated by rotors, each of them expressed in local frames R_j-$x_j y_j z_j$ are expressed as

$$\mathbf{F}_{tj} = t_j \begin{bmatrix} 0 & 0 & 1 & 0 & 0 & 0 \end{bmatrix}^{\mathrm{T}} \tag{5.3}$$

in which vector $[0, 0, 1]^{\mathrm{T}}$ is the unit vector parallel to z'-axis which represents the common direction of thrust forces by rotors while moments denoted by M_j are around rotors themselves and position free. In the moving coordinate frame, the moments are expressed as

$$\mathbf{M}_j = t'_j \begin{bmatrix} 0 & 0 & 0 & 0 & 0 & 1 \end{bmatrix}^{\mathrm{T}} \tag{5.4}$$

in which t'_j is the magnitude of the moment. All the forces and moments applied to the integrated robotic system by threads and rotors expressed in the moving reference frame P-uvw are derived by shifting,

$$\mathbf{F}_{pk} = \mathbf{T}_{pk}\mathbf{F}_k \tag{5.5}$$

where $k = i$ for cable tension exerting at points B_i while $k = j$ for rotor thrust exerting at points R_i, and

$$\mathbf{T}_{pk} = \begin{bmatrix} \mathbf{I} & 0 \\ \Delta_{pk} & \mathbf{I} \end{bmatrix} \tag{5.6}$$

in which

$$\Delta_{pi} = \begin{bmatrix} 0 & 0 & y_i \\ 0 & 0 & -x_i \\ -y_i & x_i & 0 \end{bmatrix} \tag{5.7}$$

and

$$\Delta_{pj} = \begin{bmatrix} 0 & -h & y_j \\ h & 0 & -x_j \\ -y_j & x_j & 0 \end{bmatrix} \tag{5.8}$$

Hence, the total active wrench w_p applied at point P by the m threads and the n rotors is

$$\mathbf{w}_p = \begin{bmatrix} \mathbf{F}_{p1} & \mathbf{F}_{p2} & \dots & \mathbf{F}_{pk} & \mathbf{M}_1 & \dots & \mathbf{M}_j \end{bmatrix} \tag{5.9}$$

Apart from forces and moments applied by threads and rotors, the system is also subject to a gravity force pointing in the inverse direction of Z-axis. With the modelling of active wrench derived above, the disposition and number of threads in tension needed for mechanically stabilising a multicopter and avoiding singularity in the large workspace can be determined with consideration of the screw system in eq. 5.9. This wrench matrix is the basis to be used for determining the number and disposition of launchers in the design and system integration of a SpiderMAV in the following sections.

5.3 Design of modules for perching and stabilisation

Following the geometric modelling and static analysis of the proposed robotic system for multi-modal locomotion in the section above, this section presents the design of modularised mechanisms for perching and stabilisation with integrated anchor launchers. A common constraint for designing subsystems of UAVs is the limited payload, which means the perching and stabilising modules in this work has to be lightweight. While the other technical challenges include efficient mechanisms allowing the system to actively launch anchors in various environments and system integration avoiding restrictions which limit the mobility of the UAV in certain workspace.

To allow the robot to actively fire tethered anchors (rather than drifting on air current in the manner bark spiders), the anchor launcher has to be able to release and retrieve strings, and to control the deployed length of uncoiled thread. In this work, magnets are used to attach the anchors to metallic structures. Considering that the mass of the quadcopter is relatively small

(<2.5kg), the perching and stabilising modules are not required to sustain heavy loads but to counter disturbances and ensure stability of the SpiderMAV in conditions such as a windy environment.

In summary the proposed perching and stabilising modules need to have the following capabilities

- Reconfiguring their structure and adjusting launching angles for targeting possible locations where magnetic anchors can attach.
- Launching single/multiple threaded magnetic anchors for certain distances.
- Controlling extension and maintaining tension of threads when magnetic anchors successfully attach to targets.
- Retrieving threads in scenarios where the position and orientation of the system need to be reconfigured and the that magnetic anchor fails to attach to the target position.

Considering all constraints and functions required for perching and stabilising modules, a lightweight pneumatic system capable of using compressed gas to launch threaded magnetic anchors is designed.

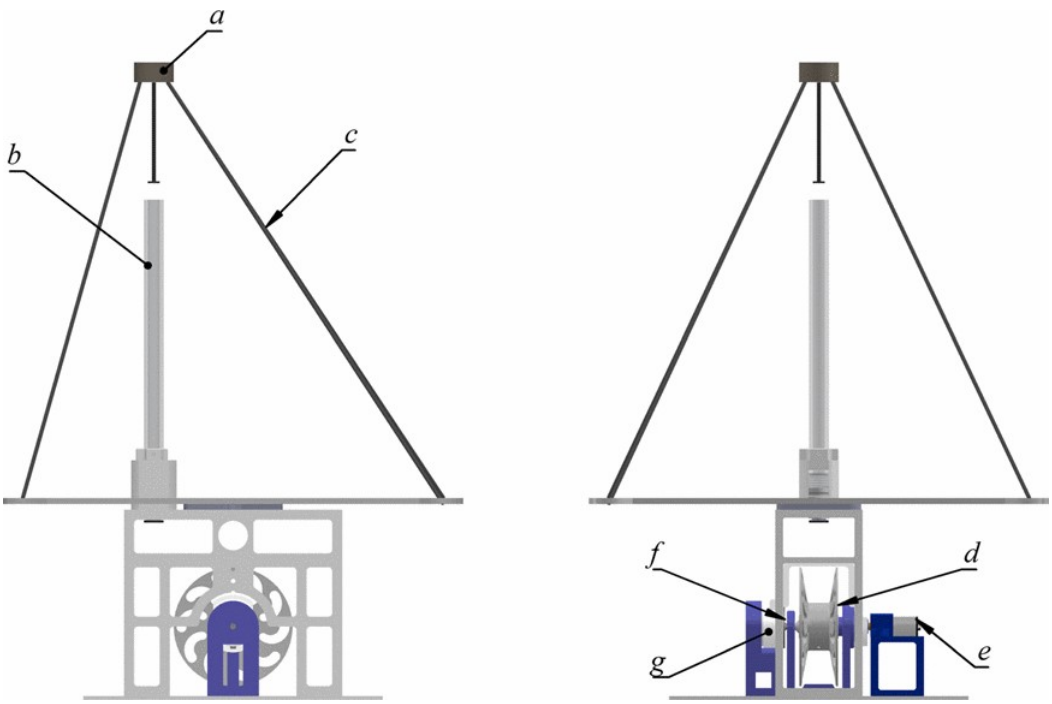

Figure 5.3: [6] The 3D model of perching module with a anchor launcher and string spooling system

5.3.1 The perching module

The perching module is to be mounted on the top of a quadcopter (DJI Matrice 100), allowing the integrated SpiderMAV to conduct Intelligence, Surveillance, and Reconnaissance (ISR) in a stationary holding mode with low energy consumption and prolonged endurance. The perching module consists of an anchor launcher and a spooling system shown in figure 5.3.

The anchor (a) is composed of a carbon fibre rod with 2mm diameter, a ring magnet fixed at the top end of the rod and plastic ring disc at the bottom end. The permanent ring magnet with 20mm outside diameter and 10mm thickness is made of neodymium (N42-NiCuNi) and capable of sustaining 9.4 kg pulling force axially. A polystyrene thread is tied to the magnetic ring. At the resting stage, the anchor is inserted into the aluminium barrel (b) of which the bore diameter matches the outside diameter of the ring disc. The tolerance between the disc and the bore of barrel allows sliding motion with lower friction during launching stage.

In the spooling system, a 3D printed spool (d) is coupled with a micro-metal gear-motor (e) and a ferrous shaft with a protruding circular section (f), where the motor shaft and the ferrous shaft are coaxial. At the resting stage, the main section of the thread is wound on the spool while the remaining section coiled on the barrel. This allows the anchor to move freely without significant drag from the thread at the beginning of the launching stage. When the anchor successfully attaches to a target position, the motor then rotates in reverse direction to retrieve the string and change the longitude. In order to maintain the tension in the thread, a braking subsystem using magnetic force is adopted in this design. As shown in figure 5.4, a miniature electromagnet (g) with a 20mm outside diameter is mounted next to the protruding circular section of the ferrous shaft with a gap of less than 1mm in the axial direction. When the electromagnet is powered, the motor is then turned off to avoid damage due to long period overloading. This electromagnet is capable of applying 2.5kg pulling force when it is fully powered and providing forces to maintain the SpiderMAV at a desired stationary holding mode.

To launch the anchor, a solenoid valve triggers a quick exhaust valve to allow instant release of compressed gas stored in a 16 gram canister for accelerating the magnetic anchor while the plastic disc is pushing forward inside the barrel by pressured gas. The thread is carried by the anchor which then attaches to target position of fixed structures.

5.3.2 The re-configurable anchor launcher for stabilising module

The 3D model of a reconfigurable anchor launcher employing a four-bar linkage for the stabilising module is shown in figure 5.4. It consists of three main subsystems including a anchor launcher, a spool actuation and braking system, and a planar crank-slider mechanism for adjusting the angle the launcher.

The anchor (a) in figure 5.4 is composed of a carbon fibre rod with 2mm diameter, a ring neodymium magnet (N42- NiCuNi) with 6mm outside diameter and 2mm diameter hole fixed at one end of the rod and a plastic disc at the other end of the rod. The ring magnet is capable of holding 1.3 Kg pulling force. The total weight of the anchor is 20 grams. By varying the number or diameters of ring magnets, the weight and capability of the pulling force of the anchor can be changed for different requirements. The customised barrel is connected to the gas canister with a pneumatic elbow tube adapter (c) capable of maximum operating pressure at 10 bar.

The reconfigurable anchor launcher uses same spool actuating and braking system for the perching module, of which the elements are denoted by (d), (e), (f) and (g).

The above two subsystems are integrated in a planar crank-slider mechanism where the slider is actuated with a customised linear screw drive system (h). The crank (i) is rotating around the coaxes of the motor and ferrous shaft at one end while the other end is jointed to a bracket mounted on the barrel (b). Coupler (j) is jointed to the bracket and linear screw drive system (h). With this one degree of freedom planar mechanism, anchor launching angle is changeable and provide extra flexibility for the stabilising module to aim at target position. The design parameters of the mechanism are customised to allow the barrel to change its direction with in a domain [0, 120]deg measured from axis of the linear screw drive system (h).

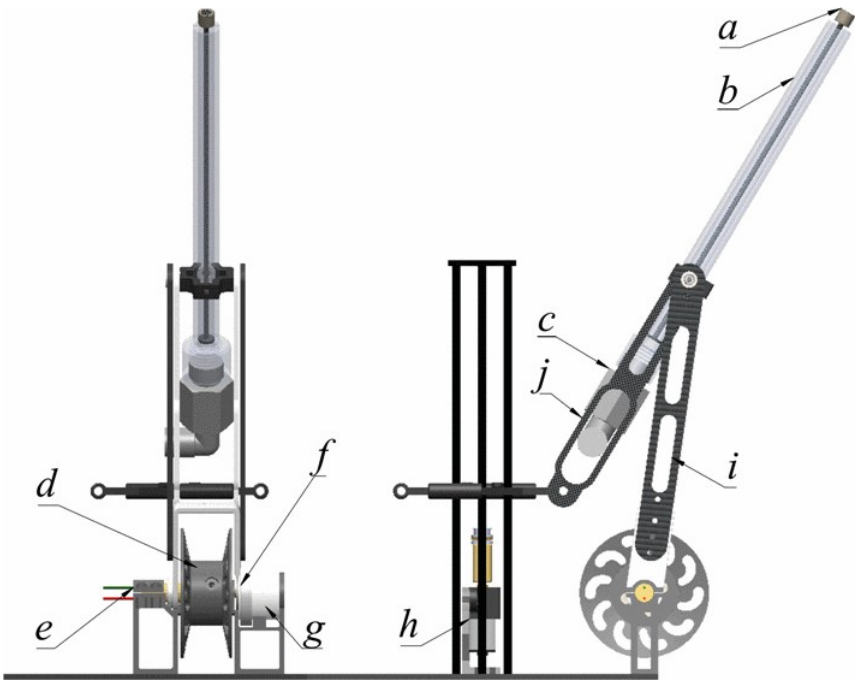

Figure 5.4: [6] Front and side views of 3D model of the four-bar linkage based reconfigurable anchor launcher

5.3.3 The integrated stabilising module

Stabilising modules with various number of anchor launchers can be configured following the principle in Section II, allowing all integrated planar mechanisms to be driven by one common linear screw drive system as shown in figure 5.5.

For a quadcopter in a hovering mode, the parallel thrust forces from each rotor form a screw system of order 3. Based on the Grassmann varieties, a SpiderMAV formed with a quadrotor needs at least three more independent forces from threads to achieve a fully constrained configuration for enhanced stabilisation in the workspace.

Following this, two prototypes were built for validating the design of the SpiderMAV proposed in this paper. One prototype with pure stabilising module composed of three anchor launchers and another prototype with one perching module on the top and one stabilising module composed of two anchor launchers at the bottom of the quadcopter as shown in figure 5.6, and the video attachment.

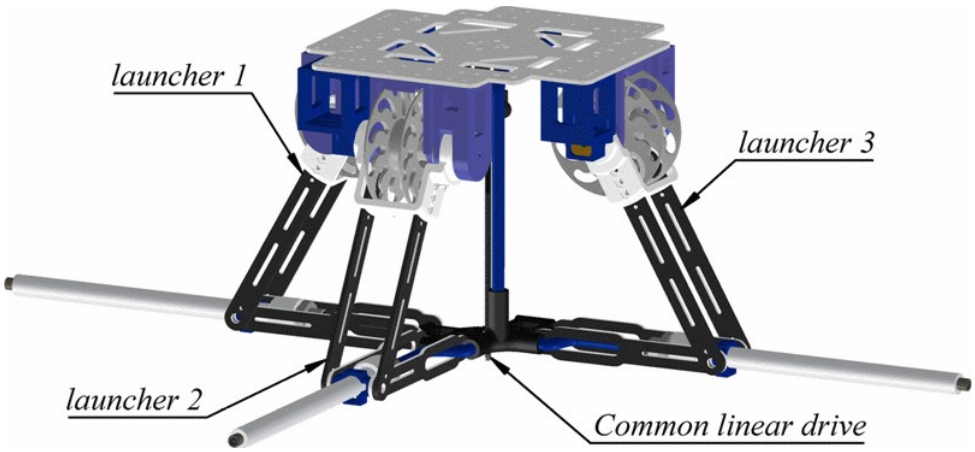

Figure 5.5: [6] An assembly of a stabilising module with three anchor launcher units sharing a common linear drive

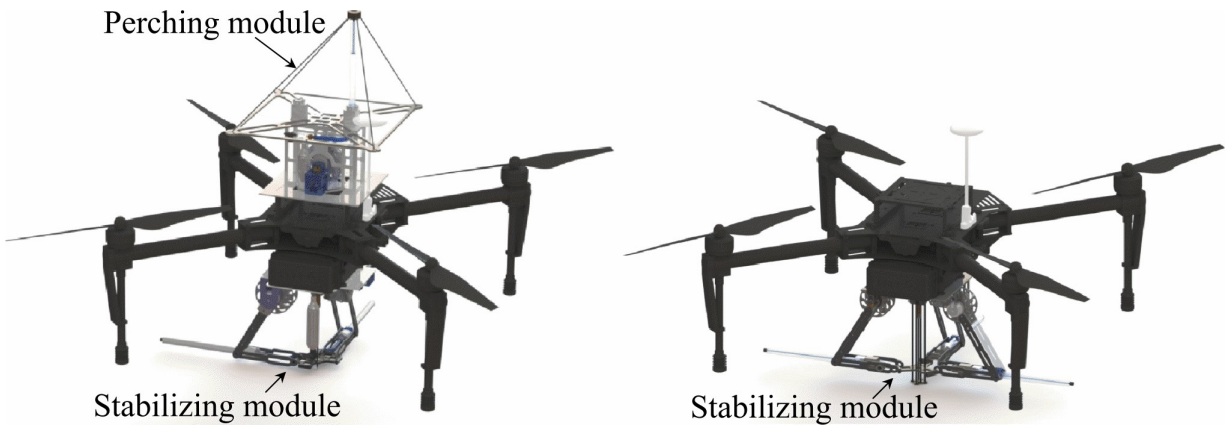

Figure 5.6: [6] The SpiderMAV: the 3D model of designs with both perching and stabilising modules (the left-hand side) and only stabilising module (the right-hand side)

5.3.4 Electronics and control

The control system of the perching and stabilising modules consists of 6 subsystems: power management, wireless communication, solenoid valve actuation system, linear drive, spooling motor control and electromagnetic braking system. For the processing unit, the Adafruit Feather M0 microcontroller is utilised to control all subsystems of the SpiderMAV. UART over Bluetooth has been chosen to be a communication protocol to actuate devices in each subsystem. Each electromagnet of the braking system is actuated by a separate MOSFET, leading to braking process for individual electromagnet or all at once. Both linear drive actuation system and spooling motor control employ bi-directional motor drivers, allowing robust control of the actuators in both directions. In the current setting, the Adafruit Fether M0 microcontroller is powered by a separate 1S lithium-polymer battery and all other devices are powered by the battery of the Matrice 100. The electronics diagram for the control system is illustrated in figure 5.7

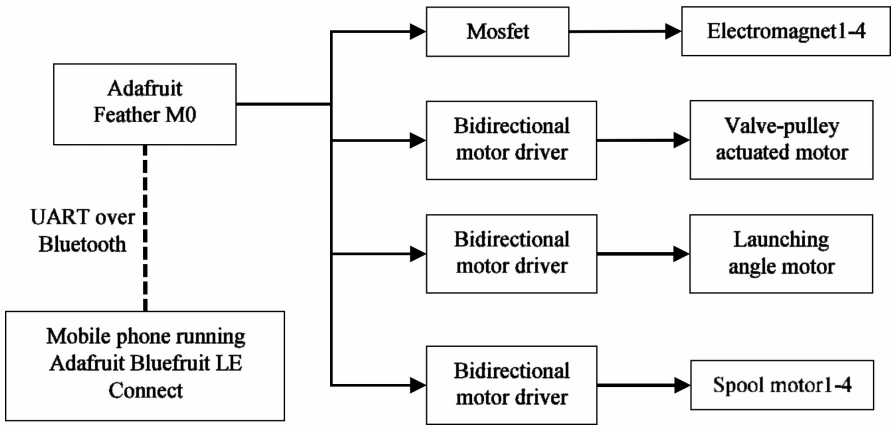

Figure 5.7: [6] The electronics diagram for the control system

5.4 Prototypes and experimental validation of enhanced stability

In this section, experiments for characterising the threaded anchor launcher as well as enhanced stability of the selected quadcopter, DJI Matrice 100, with a stabilising module are presented.

In order to obtain the horizontal barrel exit speed of the anchor, tests were implemented with a launcher powered by compressed gas at various pressures and horizontal barrel axis. The projection of the anchor is then captured with a fast speed video camera (FASTEC-TS5-386). The barrel exit velocities for gas pressures at the range of [4, 6] bar were then tracked in software using stack images captured in experiments. The results of barrel exit velocities in figure 5.8

guide settings of gas pressure for the anchoring system to allow the anchor to reach a target position which is 2.6 meter away from the barrel exit.

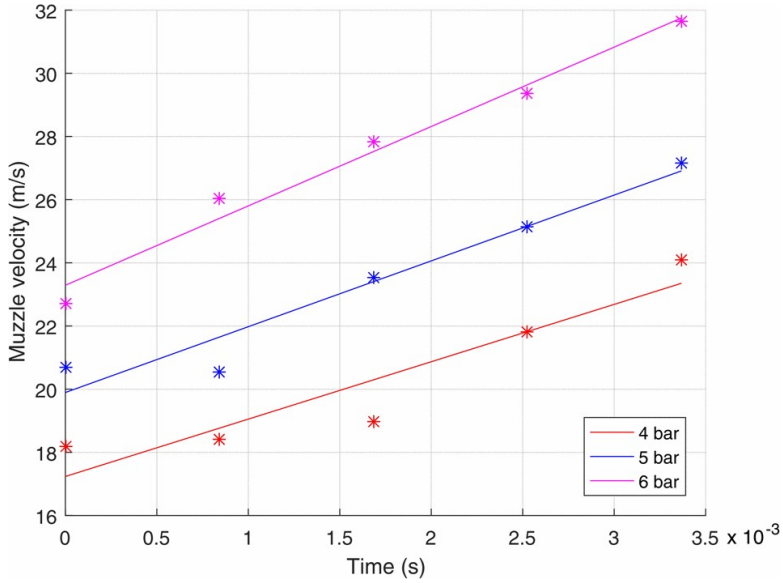

Figure 5.8: [6] Barrel exit speed of the anchor with various pressure applied to the launcher.

Tests were conducted to validate the performance of SpiderMAV prototypes. The first prototype with both perching and stabilising modules were tested in different environments with metallic surfaces at different corrosion states. As shown in the video attachment, the magnetic anchor launched by perching module was able to attach to the ceiling frame, thus allowing the robot to hold its position and orientation at high attitude and save onboard energy with rotors spinning in lower speed then switched off.

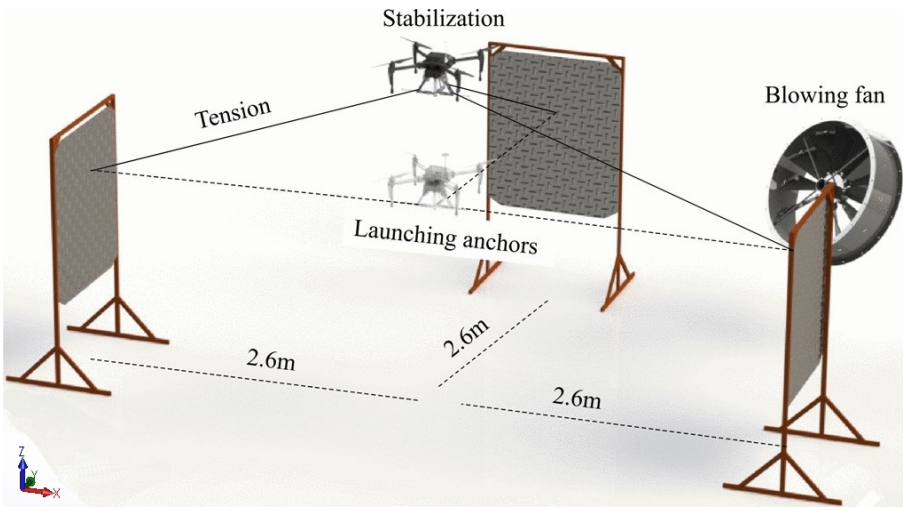

Figure 5.9: [6] Testing setup for validating enhanced stabilisation of the SpiderMAV in windy condition.

To evaluate the performance for enhanced stabilisation of the SpiderMAV, the second prototype with only stabilising module was tested in attitude-hold mode for hovering the UAV at the same position and orientation against an electric fan that was blowing and generating 5500 cubic feet per metre of air flow directly at the UAV as illustrated in figure 5.9. The anchors were then launched and attached to vertical metallic plates in three directions. With all the anchors successfully attached to the plates, the spooling system coiled the threads back to get them in tension and hence initiated the stabilising mechanism. Vicon motion capture system was used to log the position of the UAV to quantify and compare the drift in 3-dimensions space of the UAV with and without the stabilising module.

While attitude-hold mode control of the DJI M100 gave maximum deviation of 136, 386 and 106 mm in X, Y and Z direction respectively, test results showed that the stabilising module improved stability of the UAV in all 3-dimensions with maximum deviation of 47, 80 and 75 mm in X, Y and Z respectively as indicated in figure 5.10.

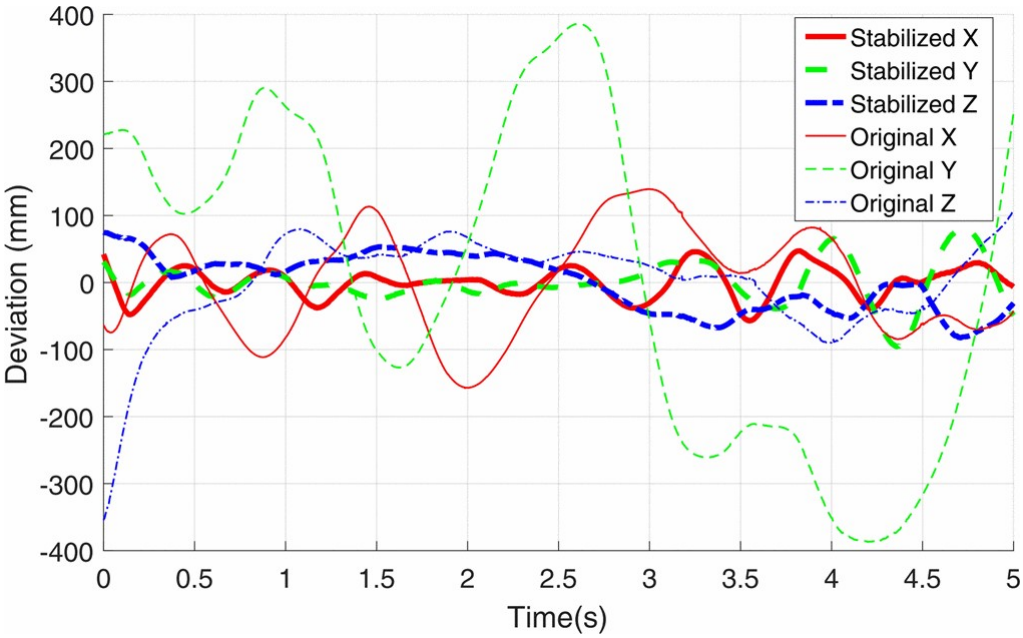

Figure 5.10: [6] Comparison of stability of the original DJI Matrice 100 and the SpiderMAV both in attitude-hold control mode.

5.5 Conclusion

The work presented in this paper tackles limited flight endurance and unexpected drift, which have been two of the main challenges for aerial robots by exploring biologically approaches in nature. Taking inspiration from the approach of using silk strands for creating large tensile structures by Darwins bark spider, this paper proposed an innovative concept for developing multi-modal aerial robotic systems with perching and stabilising capabilities, enabling solutions to critical challenges in UAVs operation such as endurance and accurate station keeping. With this bio-inspired concept, a tensile anchoring system was designed and employed in both perching and stabilising modules for low power station keeping and multi-modal operation. Using screw theory and Grassmann varieties, geometric and static principles of the aerial robotic system with both anchored tensile strings and thrusts generated by rotors were explored for modelling of the integrated system. The anchoring system powered by pressed gas has been characterised, allowing the anchor to reach target positions at certain distance with optimised pressure. The presented design concept for perching and stabilisation were then validated with experimental tests of prototypes developed, demonstrating the operation of the integrated SpiderMAV in a enhanced stable mode comparing to pure control based performance.

The proposed robotic system also opens up a new trend in the field of robotics on investigating string driven systems with an active moving platform. Analytical modelling of kinematics, statics and dynamics during locomotion are essential open problems for such an interesting system.

This chapter will be concluded with key points of achievements and progress towards AAM.

- This chapter tackles challenges of limited operation time and undesired positional drift of UAVs by developing multi-modal aerial robotic systems with perching and stabilising capabilities.
- With compressed gas magnetic anchor launching system, the stabilising module consisting of three anchor launchers is used in enhanced stability flight mode to help improve UAV stability under windy conditions within the certain physical setups.
- With the similar concept, the perching module consisting of two anchor launchers and one anchor perching unit allows low-power station keeping flight mode that extend UAV airborne operation time.
- Future works
  - Although these two operation modes are not entirely combined into one system, combining them would not be challenging, however, it would require decent design

and manufacturing work to make it happen with the nature of UAV system taken into design consideration.

- One possible future application of the work presented in this chapter towards AAM is to enable low-power tensile-aerial hybrid locomotion. Further investigation and more advanced prototypes regarding this matter are required before performance criteria of this concept can be evaluated. Starting points would be on the combined control system of flight, tensile force controller and new mechatronics designs of the system.
- Autonomous operation of tensile-flight locomotion is another research aspect worth investigating as relying on manual control required experienced human operator, thus preventing scalability.

Chapter 6

AAM: Free Form Monolithic Aerial Additive Manufacturing

6.1 Introduction

Chapter 2 demonstrates precise aerial material deposition in the form of aerial repair. The integrated delta manipulator can compensate for translational and rotational offset of the UAV between its current position and the desired position. However, for structural purposes, material deposition accuracy must be improved, suitable materials must be developed and a new system of aerial platform must be developed to better accommodate tasks required by AAM. This chapter discusses on the latest development towards AAM.

6.2 Aerial Additive Manufacturing (AAM) robotic system overview

The challenge of realising AAM is difficult due to the instability of the UAV platform flight, sensor drift, and self-induced and environmental turbulence. To achieve precise material depositions, we coupled a UAV platform with a continuous flow material extruding mechanism and a customized self-aligning Delta parallel manipulator engineered for material deposition operations at high accuracy of 5 mm in both lateral and vertical directions.

The robotic construction robots include BuildDrones and ScanDrones that can autonomously and collectively perform material deposition and post-printing scan tasks of AAM missions. The aerial robots are customized based on design requirements of the key features and specifications (Table.6.1). The BuildDrone platform (a wheelbase of 650 mm) has a kerb weight of 2.1 kg with a maximum take-off weight of 6.6 kg, and hovering flight time of 18 minutes with 2.5kg payload. This allows the robot to carry all required subsystems including high performance onboard computer, material extruder and the Delta parallel manipulator. The subsystems of the ScanDrone mainly include a onboard computer, a Gopro camera and a Intel Realsense. Considering the payload and flight time requirements of the ScanDrone, a UAV (DJI F450 frame) is adopted and developed for of post-printing scan. Both the BuildDrone and ScanDrone are equipped with a modular open-architecture for the electronic hardware. The Delta manipulator has a mass of 380 g with its base fixed to the UAV frame while the end-effector is capable of 3-DOF translations with respect to the UAV frame.

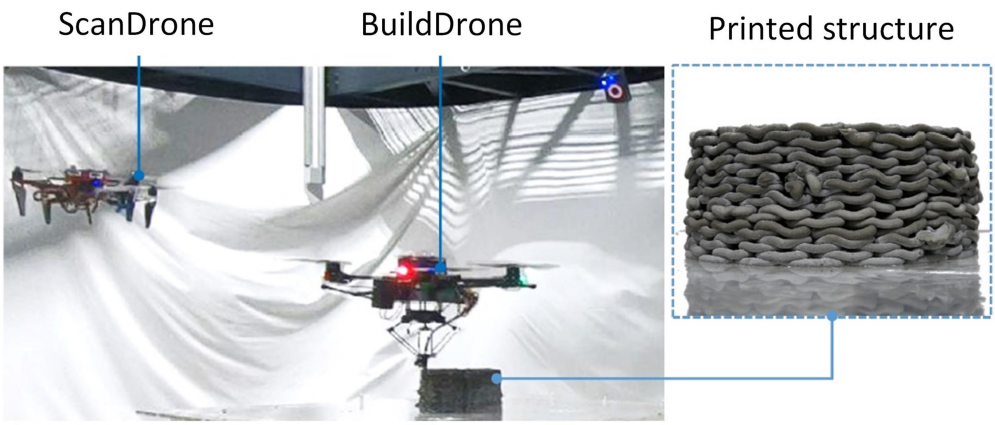

Figure 6.1: Aerial 3D printing process overview.

6.2.1 Material extrusion and flow control system

Enabling execution of the Aerial AM mission requires a reliable, low-mass and low-complexity method to transport materials between the material source and the construction site where the

robots build structures by adding layer-upon-layer of material. The material deposition process is realized with forward extrusion (a compressive deformation process) to achieve the inherent features of no surface cracking, better accuracy and surface finish and less wastage of material. To effectively control the continuous flow process of cementitious material and obtain precise and repeatable flow rates, we integrated the extrusion system (Figure 6.2a) with a control valve (Figure 6.2b) that uses a pinching effect to obstruct the material flow by forcing the tubing together and creating a seal . A one Degree-of-Freedom material cutter (Figure 6.2c) is introduced at the tip of the nozzle to precisely control the start and stop of material deposition.

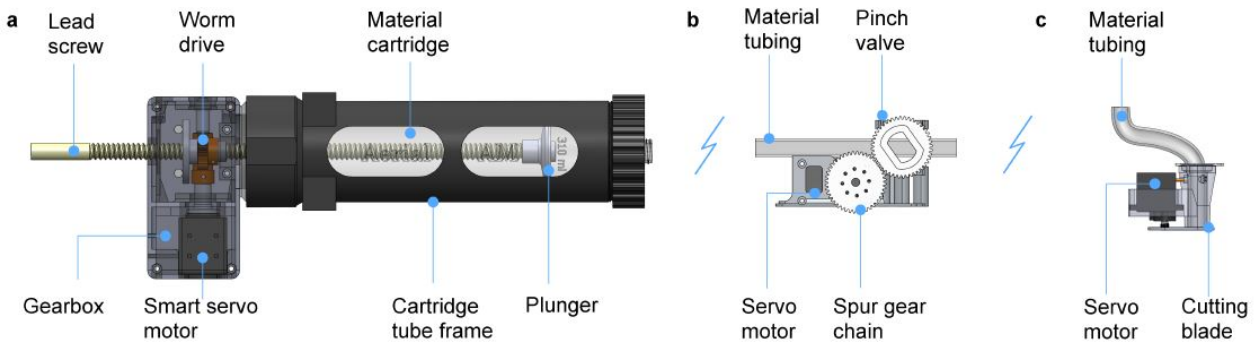

Figure 6.2: Modularised material extrusion and flow control system integrated in the Buildrone.
(**a**) Material extrusion system customized in terms of forward extrusion. The extrusion system is actuated by a servo motor, and a worm drive mechanism is chosen as a power transmission system, which can convert rotary motion into linear motion to push the material out of the orifice of the material cartridge.
(**b**) The material flow control system using a pinch valve actuated by a servo and a spur gear chain.
(**c**) A material flow cutter is attached to the lower platform of the Delta parallel manipulator and the tip of the nozzle. The cutting blade cuts and block material flow to avoid material drip at the print site.

6.2.2 Controller for the autonomous AAM robots

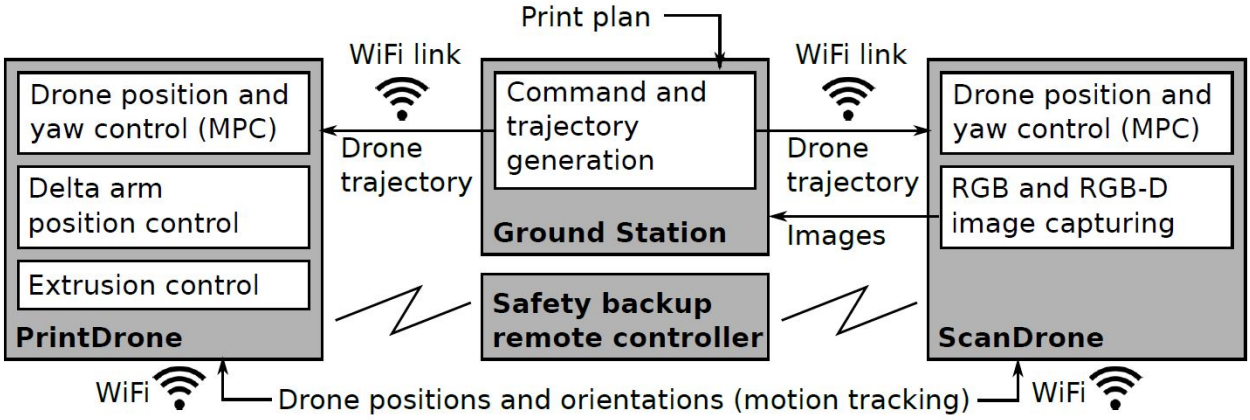

Figure 6.3: ROS based high-level control architecture of the AABM drones.

The control flow diagram of the aerial robot with integrated Delta manipulator is illustrated in Figure 6.3 and implemented in the Robot Operating System (ROS). The ROS package for the lightweight Delta manipulator controller uses real-time pose of the UAV and trajectory setpoints to compute inverse kinematics compensating the UAV's offset. We utilized the Dynamixel SDK system to establish the communication between onboard computer and Dynamixel servos used in the Delta manipulator. The controller for the Delta manipulator is running in parallel with an Model-Predictive-Control (MPC) controller for the UAV. The pose precision of the UAV was improved for slow (manufacturing) and high velocity (navigation) motion. The UAV is controlled via a classic cascaded architecture. We employ a Pixhawk attitude controller which we interface with our own position controller (3D position and yaw angle), where we initiated a finite-horizon MPC scheme. In order to interface the drone with higher-level task and motion planning, as well as with semi-automatic operation modes, a control and communication interface using ROS has been developed. We provide a high-level interface to the MPC to support task/trajectory planning, and semi-automatic control modes which are implemented using a task queue on top of ROS communication via WiFi, exposing the tasks in a full loop of operation.

Schematic drawing and Skeleton code for the compensation algorithm of the self-aligning Delta Manipulator can be viewed in Figure 6.5 and 6.6 respectively.

*The MPC controller for the UAV has been developed by Aerial ABM project collaborators as stated in the declaration. The content above is discussed here to give a broader view regarding enabling technologies for AAM.

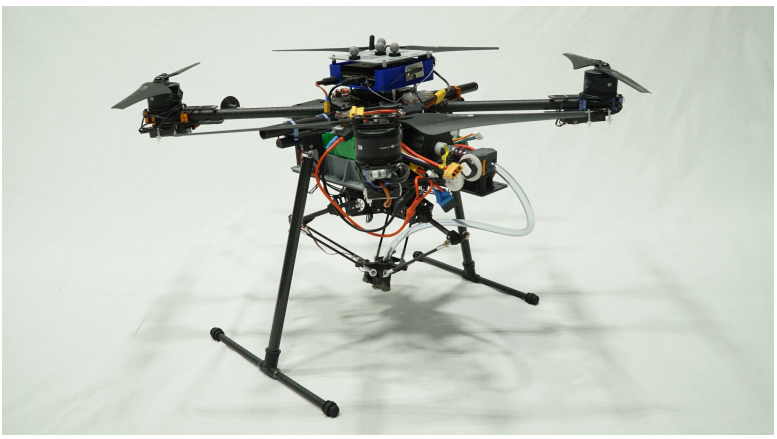

Figure 6.4: BuildDrone.

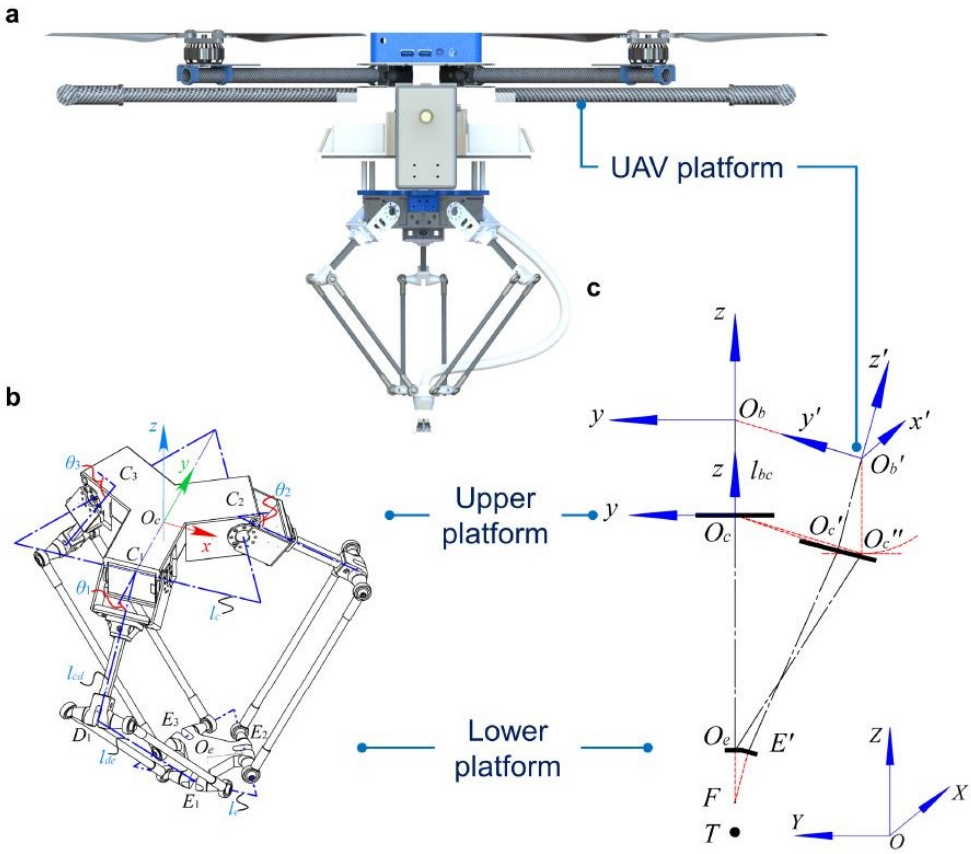

Figure 6.5: Compensating offset of UAV using an onboard dexterous 3-DOF Delta parallel manipulator.
(**a**), The setting of Buildrone with upper platform of Delta manipulator mounted underneath the UAV platform with a wheelbase of 650 mm.
(**b**), Model of a lightweight Delta parallel manipulator which has three limbs with identical kinematic structure. The lower platform with geometric centre O_e implements pure translational motion with respect to the upper platform with geometric centre O_c.
(**c**), Schematic drawing of the compensation principle: the nozzle tip F keeps at desired position though the UAV platform drift to the pose at O_b' away from the reference pose at O_b. This leads to accuracy for depositing the material at target position T.

Algorithm 1: Aerial Delta Manipulator Kinematic Compensation

```
Set up ROS command subscribers and publishers
Parameters initialization
if command callback is called then
    delta_on ← delta operational command status
    if delta_on is true then
        target_[x,y,z] ← Current UAV position target in inertial frame
        delta_target_nz_[x,y,z] ← [target_x, target_y, target_z-offset] %position target for the nozzle tip
        uav_position_[x,y,z] ← Latest UAV position in inertial frame
        uav_quat_[w,x,y,z] ← Latest UAV orientation in inertial frame
        inv_uav_quat_[w,x,y,z] ← inverse_quaternion(uav_quat_[w,x,y,z])
        TE ← [0, 0, nozzle_length]
        TE' ← TE rotated by a quaternion uav_quat_[w,x,y,z]
        delta_target_eff_[x,y,z] ← delta_target_nz_[x,y,z]+TE' %position target for the end effector
        O'A' ← [x_offset,y_offset,-drone_to_delta]
        O'A'' ← O'A' rotated by a quaternion uav_quat_[w,x,y,z]
        delta_base ← uav_position_[x,y,z]+O'A'' %current position of delta manipulator base
        A''E''_O ← delta_target_eff_[x,y,z]-uav_position_[x,y,z]-O'A'' %control vector in inertial frame
        A''E''_B ← A''E''_O rotated by a quaternion inv_uav_quat_[w,x,y,z]
         %to express the vector in body frame of the delta manipulator base
        computed_angles ← compute inverse kinematics from control vector A''E''_B
        if no solution then
            servo_command ← last_servo_command %stay at last angle
        else
            if servo angle exceed min_angle and max_angle then
                servo_command ← last_servo_command %exceed angle limit
            else
                servo_command ← computed_angles
            end
        end
        last_servo_command ← servo_command %record last command
    else
        servo_command ← home_angles %deactivate and go to home
    end
    publish servo_command to dynamixel low level controller
else
    wait for callback to be called
end
```

Figure 6.6: Skeleton code for self-aligning Delta manipulator

6.2.3 Cementitious material for AAM and structure performance

Cementitious materials are suitable for large-scale additive manufacturing due to its established suitability for large-scale construction, its high compressive strength and its relatively low embodied energy. Both cementitious and polymeric composite materials have been examined in this project. However, existing mixtures used in additive manufacturing are not suitable for AAM, which requires the miniaturisation of Additive Building Manufacturing techniques and it needs to be deposited with a lightweight deposition system. The developed AAM materials therefore need to be modified significantly from those utilised in traditional mortars and ground-based ME 3D concrete printing systems.

To match such requirements, a novel cementitious-based composite mixture has been developed specifically for AAM focusing upon polymeric Rheology Modifying Admixtures (RMA) being utilised to reduce fine aggregate requirements and facilitate successful deposition.

With the tailored mixtures, aerial 3D printing trajectory design for structures was informed by the parameters including: the lateral deposition accuracy of the BuildDrone during flight, material deflection while spanning voids in the previously deposited layer, and material settlement when under compressive loading from subsequently deposited layers.

Three designs, in which spans were kept to a minimum, were evaluated for constructing a tower structure. The designs include 1) Four adjacent concentric circles effectively forming a solid wall (Figure 6.7a). A Maze design, with alternate layers staggered in the circular centre-line plane (Figure 6.7b) A hybrid design consisting of three non-adjacent concentric circle layers alternating with an orthogonal Maze design (Figure 6.7c).

Comparing the three different trajectory designs, the Maze design has advantages in three aspects. First, it requires less material: 5.85 m printed length per two layers compared to 6.79 m for the ruffle design and 7.61 m for the solid wall design. Second, structural efficiency relative to amount of material used: Preliminary 7-day compressive strength tests were conducted on four layers of hand-printed wall arc-lengths for the three trajectory designs (Method Supplementary). Results indicated a mean 16.5 MPa for the Maze design, greater than 14.4 MPa recorded for the wall design. Third, it demonstrated lateral precision capabilities of BuildDrone extrusion and aesthetic qualities.

In combining with the trajectory design, the chosen mix was selected given the appropriate workability-buildability combination, more efficient manufacture due to the absence of fine aggregate and foam, high viscosity at rest, and passing through the deposition system comfortably within BuildDrone power capabilities, with a level of force about 500 N required during extrusion.

*The developed cementitious mixes and aerial 3D printing trajectories have been developed by Aerial ABM project collaborators as stated in the declaration. The content above is discussed here to give a broader view regarding enabling technologies for AAM. [147, 148, 149]

6.3 Multi-Agent Aerial Additive Manufacturing (Multi-AAM) framework

Large scale Aerial Additive Manufacturing would require multiple UAVs, supplied with a battery and material payload at a stationed position, making agile flights to and from varying deposition locations. A deposition sequence requires flight at slower velocities relative to the material and deposition hardware constraints described. To coordinate these actions, Multi-Agent Additive Manufacturing flight framework (Multi-AAM) has been developed to enable high-level motion planning and coordination of multiple aerial robots to undertake manufacturing using autonomous task determination and decision making; providing capabilities for live adaption, spatial collision awareness, system robustness and redundancy. The framework can import a geometry identified for manufacture which is then parametrically divided into several horizontal contour curve layers that represent discrete deposition trajectories and stored globally for each robot to access. As a structure is being built, the Multi-AAM also allows each robot to share their state, task and pose across a network to share knowledge of the deposition trajectories, the locations of other robots and already deposited material so that they can individually determine their next tasks and navigate autonomously, while avoiding obstacles and undertake path planning.

Each aerial robot agent is represented by a centre-point 3d (X,Y,Z) position, a deposition end-effector 3d point position, a collision radius that defines a sphere of space to be occupied solely by the robot, and a velocity vector heading. Operating in live flight demonstrations, this information can be updated at 100Hz by subscribing to ROS Topics of either Optitrack or Vicon IR motion-capture marker positions. Each robot agent calculates a vector heading at 100 Hz, which is sent as an instruction to the robot MPC when traveling to or from a deposition task, while an entire deposition trajectory is submitted to the MPC for deposition tasks where the MPC executes the high-precision flight path using different high-precision settings. It is worth noting that each robot agent can also over-ride the MPC at any moment where a change in task or state is determined. The framework monitors the states and tasks for each robot and was utilized to control both BuildDrone and ScanDrone robot platforms.

*A simpler implementation of high-level motion planning with single Buildrone has been used in the demonstration in this chapter. The Multi-AAM has been developed by Aerial ABM project collaborator as stated in the declaration. The content above is discussed here to give a broader view regarding enabling technologies for AAM.

6.4 Aerial Additive Manufacturing demonstration results and analysis

To demonstrate Aerial Additive Manufacturing with the novel cementitious-based composite mixture, we proposed a new type of vertical tower that is possible to manufacture by layered deposition without requiring temporary supports or form-work. To realise this structure within our laboratory constraints, we used Multi-AAM with the BuildDrone, with specification showed in table 6.1, with Delta parallel manipulator to demonstrate live additive 3D printing of a 180 mm high portion of 12 m tall pylon structure. The rest of the 3.2 m top section of the pylon structure was built using a virtual 3D light painting method (Figure 6.8b) to validate capabilities for continuous operation and building credentials that could be extended to large volumes. The actual 3D printed portion of the structure consisted of 28 horizontal layers (Figure 6.8c), using the Maze deposition trajectory. Each layer utilised a deposition length of 2.975 m, using the full material payload of the UAV, requiring a material refill between layers.

With data obtained during the printing experiments, we evaluated the accuracy of the UAV pose as well as the tip of the delta manipulator in both real and virtual printing. Figure 6.9 shows the reference UAV position, effective UAV position, and effective delta manipulator tip position employing the control schemes as introduced above. For quantitative evaluation of the printing accuracy, we logged the trajectories during the actual printing campaign. Respective Root-Mean-Square Errors (RMSE) per layer of printing are provided in the summary (Table 6.6) for both the UAV position and the delta manipulator tip position. For a more detailed analysis of the positioning accuracy, we studied the UAV position reference and effective position per axis (See Supplementary Methods). We also show the respective Error statistics in Figure 6.9.

Through these printing experiments, intuitively we found that the position accuracy of the delta manipulator tip should be at least as high as the UAV's performance. However, it is worth noting that the delta manipulator not only has to compensate for deviations of the drone position, but also incurred tip deviations due to altitude deviation as a function of the lever arm between the UAV centre of mass and the delta manipulator tip. The accuracy of the delta manipulator tip position is shown in Figure 6.9.

Additional statistics of the demonstration can be found in the following figures and tables.

Airframe	Diagonal wheelbase	650mm
	Weight with 6S battery	2.1kg
	Max takeoff weight	6.5kg
Propulsion system	Motor model	DJI 4126
	Propellers	DJI 1760 Foldable
	ESC	DJI E640S
Flight controller	Pixhawk	Model 1
Battery	LiPo 6S	16000mAh
Onboard computer	Intel NUC	i7-7567U
Performance	Hovering time	18 min
	Mixed flight	15.5 min
	Max speed	30 km/h
	Hovering accuracy (Vicon)	<10 mm

Table 6.1: Aerial ABM UAV features and design specifications.

Vessel internal diameter	47	mm
Vessel area	1735	mm^2
Vessel full height	213	mm
Vessel theoretical volume	310	ml
Vessel practical volume	202	ml
Circular nozzle diameter	8	mm
Tube length	560	mm
Tube area	50.3	mm^2
Tube volume	28.2	mm^3

Table 6.2: Dimensions of deposition device components.

Empty vessel	44.4	g
3D printed tapered component	19.5	g
Empty 560mm tube	29.6	g
Metal connecting components	46.2	g
Cable ties	0.3	g
Total	143	g

Table 6.3: Mass of deposition device components.

Printed length of material possible with vessel practical volume	4020	mm
UAV velocity, length of material per second	10	mms^{-1}
Length of printed trajectory per layer (including tails)	3000	mm
Time to continually print one layer	300	secs
Volume of material printed per second	0.5	mls^{-1}
Vessel flow velocity	0.294	mms^{-1}
Vessel volumetric flow rate Q	510	mm^3s^{-1}
Tube flow velocity	4.44	mms^{-1}
Tube volumetric flow rate Q	223	mm^3s^{-1}

Table 6.4: UAV powered deposition device printing velocities.

Printed line length of material per ml	19.9	$mmml^{-1}$
Volume of material required to print 1 layer of the 28-layer structure	151	ml
Material guide density	1.5	gml^{-1}
Mass of material required to print a layer	226	g
Volume of material within the 3D printed tapered component internal space	61.7	ml
Volume of the tube	28.2	ml
Volume of the metal connecting components and vessel nozzle	2.97	ml
Volume of material lost every vessel load	92.8	ml
Mass of material lost every vessel load	139	g
Volume of material required per layer (accounting for lost material)	244	ml
Mass of material required per layer (accounting for lost material)	365	g
Total mass of vessel fully loaded with material required for 1 layer	508	g
Total mass of vessel fully loaded with material provided for 1 layer	630	g
Mass of material provided for 1 layer	487	g
Total mass of vessel with remaining material *post extrusion*	414	g
Mass of material used per printed layer	216	g
Volume of material used per printed layer	144	ml
Mass of spare capacity material recoverable for the subsequent layer	132	g
Volume of spare capacity material recoverable for the subsequent layer	87.8	ml

Table 6.5: UAV controlled flight printing logistics.

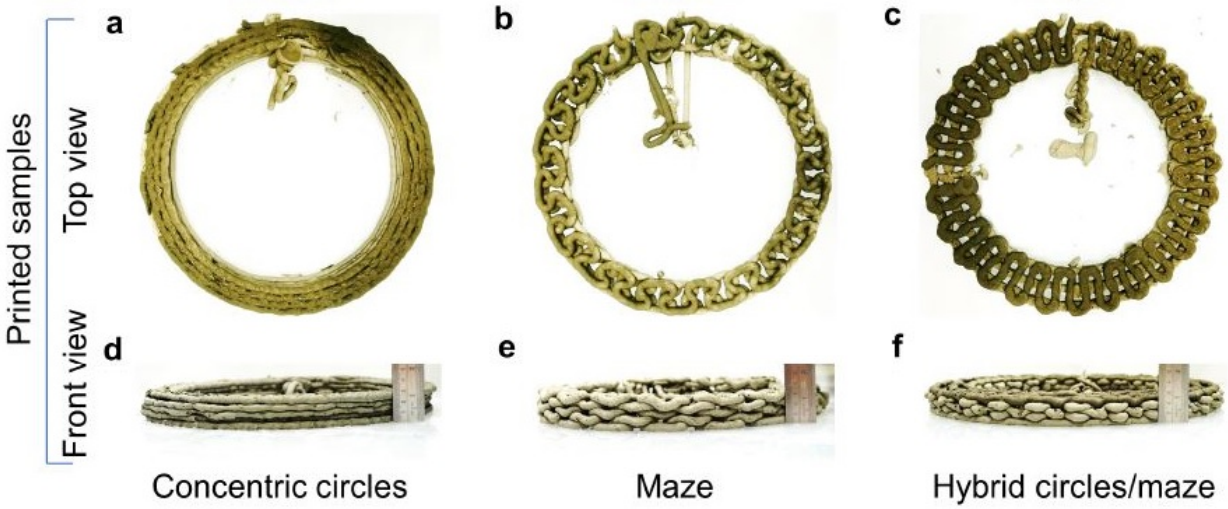

Figure 6.7: Various designs and printed structure of sample trajectories.
(a-c). The top layer of the printed samples with pure concentric circles, pure Maze pattern and hybrid maze and concentric circles.
(d-f). Front view of the printed samples, each of which is a five-layer structure with different layer patterns.

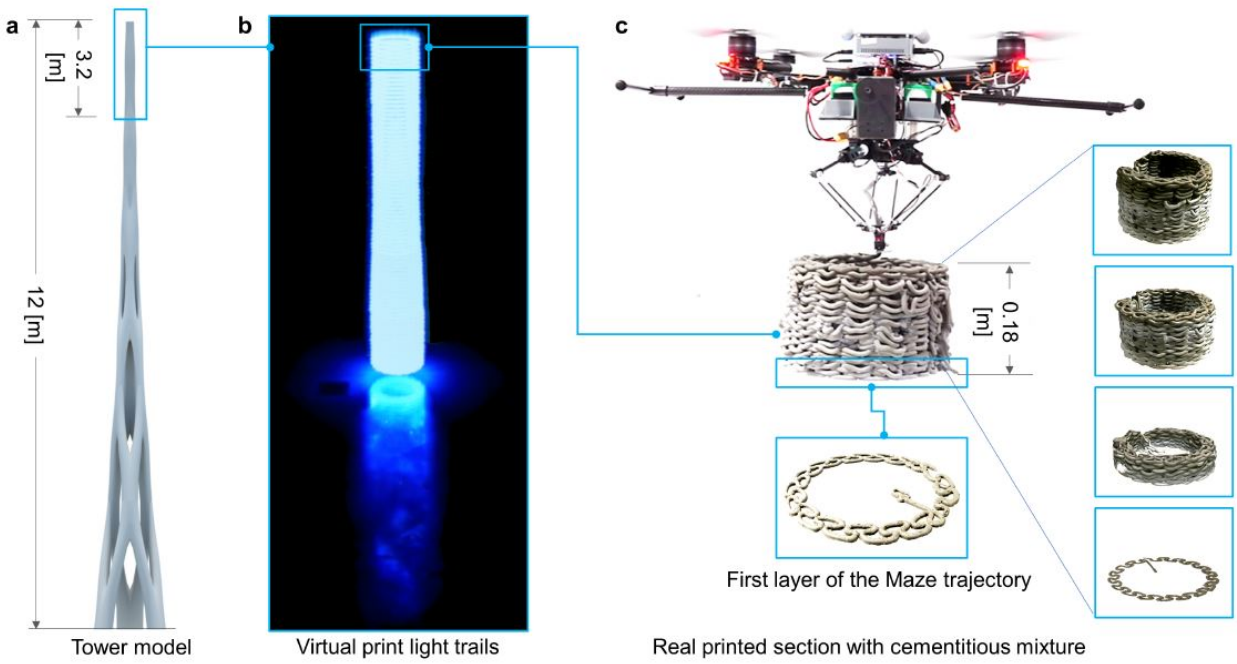

Figure 6.8: Virtual and actual printing of the sections at high altitude of the designed tower structure. Subfigure a. courtesy of Robert Stuart-Smith.
(a) Computer generated image of a 12 m high tower structure built by additive manufacturing based on numerical studies. (Courtesy to Robert Stuart-Smith and Vijay Pawar)
(b) The section at high altitude of the tower built in the virtual printing experimental tests. The virtual printing speed is 5 times faster than the actual printing, i.e. 50 mm/s while each layer is xx mm. This results in a 3.2 m high structure using light painting techniques.
(c) The structure built by depositing cementitious mix with the BuildDrones. The BuildDrone deposits the material at a speed of 10 mm/s. The thickness of each fresh layer is determined by both the circular nozzle orifice diameter (8 mm) and the minor stretching force while the nozzle tip moves along the printing trajectory. The final height of the minimal 28-layered structure is 180 mm after the material is settled.

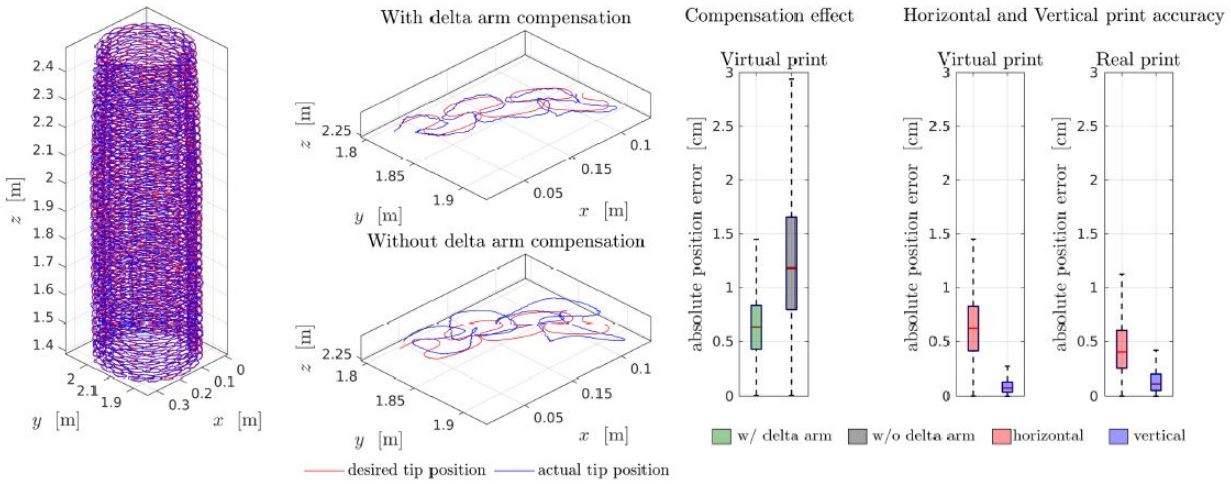

Figure 6.9: Evaluation of position accuracy of the BuildDrone and the end-effector of the integrated Delta parallel manipulator. Figure courtesy of Dimos Tzoumanikas.
(a) BuildDrone position reference (in red) and Delta parallel manipulator tip actual position (in blue) during the virtual printing of the high altitude section of the tower structure employing the Maze trajectory.
(b) The close-up view of the desired Maze trajectory and the actual tip position in the scenarios with compensation function from the Delta parallel manipulator and that without the compensation function. It intuitively illustrates the importance of the integrated Delta parallel manipulator for achieving higher accuracy at the tip of end-effector which is with certain distance away from the mass centre of the UAV.
(c) Quantitative evaluation of the accuracy of the Delta parallel manipulator tip position in both virtual print and real print. In the virtual print, the absolute position error in lateral direction is higher than 0.5 mm, which may caused by trajectory geometry with small curvatures but implementing a higher flight speed. In the actual print, the absolute position error is smaller than 0.5 mm which is proved acceptable for the printing nozzle with 8 mm diameter.

	RMSE [cm]					
Layer N°	MAV			delta manipulator		
	x	y	z	x	y	z
1	0.243	0.398	0.155	0.406	0.301	0.080
2	0.260	0.456	0.278	0.324	0.275	0.069
3	0.314	0.487	0.187	0.418	0.345	0.085
4	0.275	0.456	0.175	0.282	0.361	0.075
5	0.327	0.392	0.162	0.422	0.353	0.083
6	0.292	0.536	0.193	0.308	0.343	0.067
7	0.213	0.421	0.147	0.348	0.287	0.075
8	0.247	0.432	0.174	0.212	0.274	0.068
9	0.248	0.345	0.137	0.389	0.268	0.068
10	0.313	0.506	0.174	0.190	0.226	0.085

Table 6.6: RMSE per layer for UAV position and delta manipulator tip position.

6.5 Analysis of operation

6.5.1 Controller

The MPC used for this chapter displays better performance in terms of flight accuracy and reduces the amount of correction movement the integrated delta manipulator has to compensate, which directly contributes to the improvement of end effector positioning accuracy. The actuators used for this iteration of the delta manipulator are of higher quality, higher torque output and faster communication speed compared to the integrated delta manipulator in chapter 2, hence higher manipulation force and a faster manipulator control rate have been achieved.

Like in chapter 2, the theory behind this self-aligning delta manipulator remains the same even though multiple aspects, such as programming, electronic and mechanical, have been improved. The self-aligning delta manipulator controller still utilises only kinematic equations, ignoring the dynamics of the whole aerial robot system. The next step would be to take dynamics of the system into the controller's consideration; this should improve end effector positioning accuracy if done effectively.

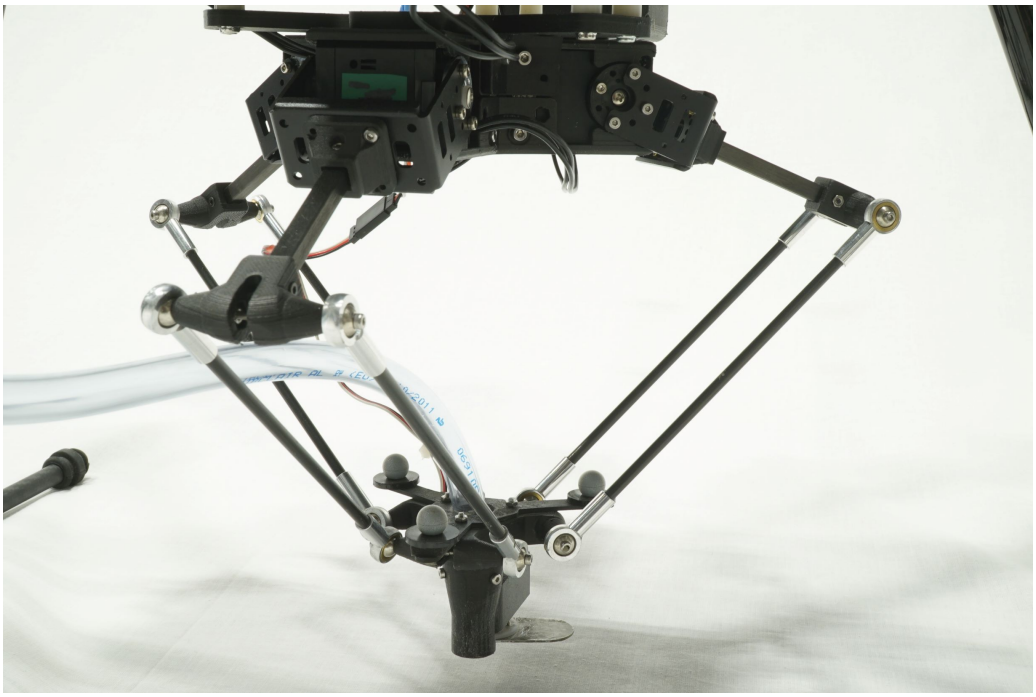

Figure 6.10: The integrated delta manipulator for precise aerial deposition

Unlike industrial robots that remain static and rely on encoders to easily compute the end effector position, UAVs need to use different localisation technologies, such as GPS, external motion capture systems, ultra-wideband positioning systems (UWB), and VI-sensors, which are relatively more difficult to implement. For external motion capture systems, the Vicon motion

tracker system, with localisation accuracy of sub-millimetre level, has been used to provide absolute position data to the controllers. However, this type of system relies on infrared light and reflective markers (active infrared LED can also be used) to track a motion of an object, which makes it unsuitable for environments with too much ambient infrared radiation, such as outdoor locations under direct sunlight. The system also has limited tracking workspace as it needs tracking cameras to completely cover the whole object tracking field. Ultra-wideband positioning system is an emerging technology that relies on ultra-wideband wave to localise objects. Although this technology has potential for improvement, the achievable accuracy, currently at centimetre-level, is not enough for AAM [150]. VI-sensor-based SLAM framework [56] has been implemented in chapter 2 with satisfactory level of accuracy for aerial repair tasks, but AAM would require much better accuracy. Therefore, AAM has been achieved only with Vicon motion tracking system and not with other means of localisation. It is noteworthy that Aerial ABM is currently focusing on a localisation algorithm based on data fusion between VI-sensor-based SLAM framework and RTK-GPS for outdoor positioning.

6.5.2 Aerial Additive Manufacturing logistics

A Buildrone uses two LiPo 6S batteries, with a combined capacity of 16Ah. This provides around 930 seconds of flight time. With 300 seconds required for one-layer continuous printing of the selected trajectory, excluding trajectory back and forth from the starting point to the printing location, one set of fully charged batteries can accommodate maximum aerial printing of two layers. This may not be convincing in terms of energy efficiency, but several improvements are possible. First, the printing speed is constrained by two factors: the maximum mechanical power output from the extruder actuator and the workability of the cementitious material used by the extrusion mechanism.

The more workability of the material, the easier for the extrusion mechanism to extrude it, though increasing its workability will reduce its buildability, hence making it less structural viable and potentially counterproductive to further reduce the workability from the current level. Instead, using a more powerful extruder actuator that can provide significantly more mechanical output should be considered for future design iterations. Yet a more powerful actuator may be heavier, take up more space and require more power to operate. The mechanical structure of the extrusion mechanism can also experience higher internal stress from a higher level of force produced by the actuator, which could lead to its mechanical failure.

With relatively limited material payload per flight, a Buildrone will have to be frequently refilled with a new set of material by the manual refilling process, which requires operators to prepare new cartridges of material to replace with the depleted cartridge onboard the UAV. This is a tedious process that depends on the operators not making mistakes. A solution would

be to automate the refilling process and at the same time increase the payload capacity of the UAV to accommodate more material, though refilling process automation requires further investigation and increasing UAV payload capacity may come with undesirable side effects such as an increase in UAV's size that makes it more difficult and risky to operate.

6.5.3 Extrusion process

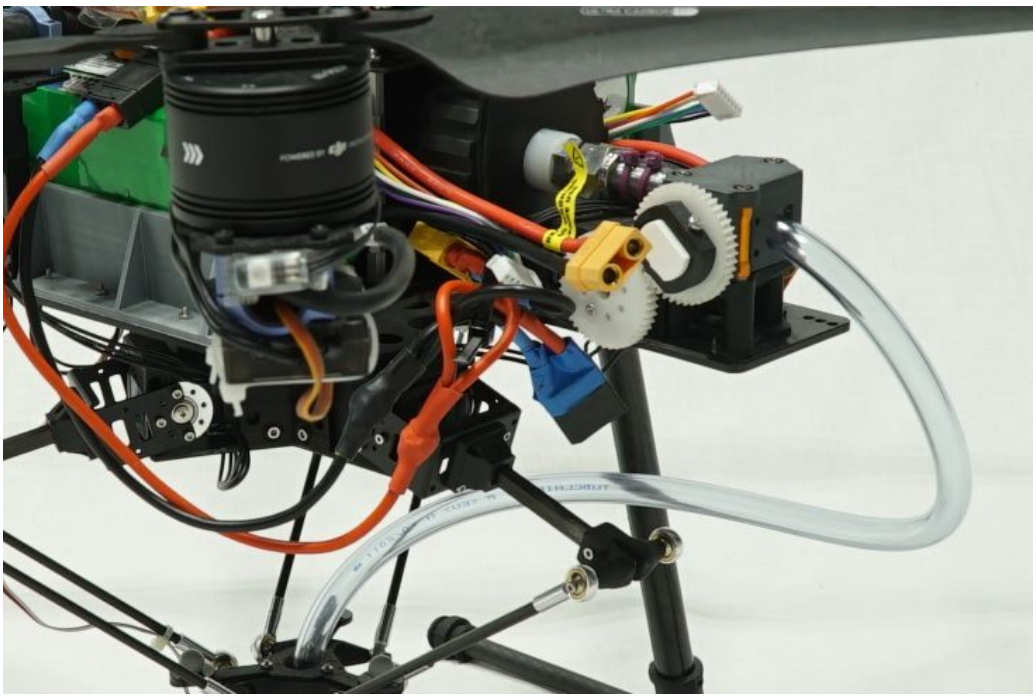

Figure 6.11: The extrusion mechanism and the material delivery tube

Frequently changing material cartridges has another undesirable side effect; the aerial 3D printing process has to be stopped and must be resumed at the exactly the same location. This requires exact timing of material flow control, which is not as straightforward as it may sound due to timing uncertainties involved in the extrusion.

The extrusion process is divided into three sub-processes: the initial compression process, the tube extrusion process and the continuous extrusion process.

- The initial compression process starts when the extrusion mechanism begin to compress the material in the cartridge, leading to a pressure build-up of the material, and ends when the material starts flowing into the delivery tube after being pushed out by the build-up pressure in the cartridge.
- Next, the tube extrusion process directly starts when the material flows into the delivery tube, continues as the material travels along the full length of the delivery tube and ends

when the material reaches the end of the printing nozzle.

- Finally, the continuous extrusion process is, as the name suggested, a continuous extrusion of the material starting after the tube extrusion process and lasting until the material has been used up or the controller has been given a command to stop. Two significant problems have been observed during the demonstrations.

First of all, the times it took to finish the initial compression process are inconsistent. The reasons behind this are expected to be from inconsistent amounts of material being stored in a cartridge and also from different initial positions of the plunger inside the cartridge. Second problem existence of air bubbles inside the material cartridge, which can disrupt the timing during the extrusion process. In particular, large air bubbles reaching the printing nozzle as the material are being deposited will leave significant gaps in the printed structure if the aerial 3D printing process has not been stopped to wait for the material flow to continue.

6.5.4 Material flow control

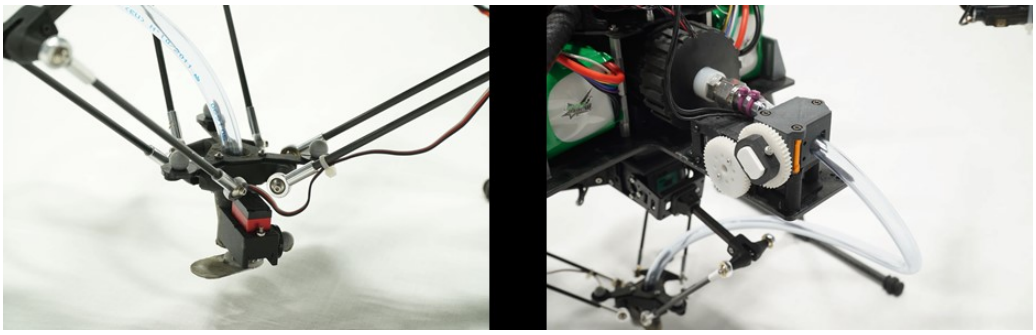

Figure 6.12: Material flow cutter (left) and pinch valve (right)

For the current design, two material flow control components have been used: a pinch valve and a material flow cutter. A pinch valve has been used to block material flow at the beginning of the delivery tube, preventing additional material from entering the tube and also maintaining the build-up pressure inside the cartridge. The material inside delivery tube, however, will still be at a high pressure and continue to flow out of the printing nozzle. As a countermeasure, a cutter valve has been used to split the flow of material into two parts, separating the deposited part from the on-going flow inside the delivery tube. This solution, even though is effective, requires experienced personnel conducting visual observation of the state of material flow to execute the flow control method at the right timing. A better solution must be developed to reduce dependency on human operators and to avoid any error arising from that.

6.5.5 Demonstration

The demonstration is carried out by 2 personnel dealing with material refilling and 3 personnel dealing with Aerial ABM UAV operation. Further research and development are required to reduce the number of personnel needed to operate and supervise the AAM processes.

When the 28th layer was being printed, the BuildDrone control system had a latency in the wireless communication system, which is used to relay current position data of the Buildrone from external motion capture system, exceeding a maximum timeout setting in the flight controller for receiving localisation data. This caused the BuildDrone to start an emergency landing sequence and crashed on the structure that has been previously printed, damaging it in the process. This exposes the underlying risk involved with utilising aerial robots for AM as they strictly require constant propulsion and correct manoeuvre to stay aloft at the right place and at the right time. Further research is required to improve on these aspects: robustness and reliability of the operation.

6.6 Conclusion

Through virtual and actual printing, we demonstrate the aerial additive manufacturing system towards autonomous robotic construction. The distributed aerial system provides a scalable and flexible approach capable of collective multi-agent manufacturing suitable for large-scale construction projects with geometrically constrained and inaccessible locations. It can complement conventional ground based construction methods.

The coupling of a self-aligning Delta parallel manipulator and a UAV allow us to realize autonomous operation of material deposition at high accuracy of 5 mm in both lateral and vertical directions. Through the proposed scalable approach, we both constructed the virtual light painting of the section of 3.2 m from top of a 12 m tall pylon structure and the 28-layered portion of the structure in a way of sequentially coordinating a team of two BuildDrones and one ScanDrone.

The actual aerial 3D printing of the 28-layered structure with a trajectory length of 83.3 m proved that aerial robots carrying lightweight deposition devices are capable of extruding a pseudoplastic, structurally viable cementitious polymeric composite material with densities 1600 kg/m^3. The virtual light painting was completed at a speed 5 times faster than the actual 3D printing. This indicates that the printing speed of individual aerial robot is scalable in accordance with the accuracy of the BuildDrone at various flight speed and the material properties.

The 28-layered structure is a minimal portion designed to demonstrate our integrated structure design and autonomous manufacturing system using a coordinated team of aerial robots, which may serve as a foundation for realizing automated construction using collective multi-agent manufacturing system.

Chapter 7

Conclusion

7.1 Summary of Thesis Achievements

Towards realising precise aerial deposition for AAM, the aerial robot with integrated Delta manipulator has been developed to demonstrate predefined autonomous aerial repair tasks with amorphous repair material with the end effector positioning accuracy requirements satisfied in both external motion capture environment and onboard VI odometry-aided navigation. However, due to the nature of the chosen amorphous repair material, LD40, and the aerial repair application itself, the required material deposition accuracy is easier to attain when compared to the accuracy required for direct extrusion of cementitious materials for the structure application. The same concept of an aerial robot with an integrated Delta manipulator has been developed towards more precise aerial material deposition. The second iteration of the platform is designed not only to have a higher payload to accommodate a much heavier extrusion mechanism and a large quantity of onboard building material but also to be able to achieve higher end effector positioning accuracy. The 28-layered structure with trajectory length of 83.3 m has been 3D printed with aerial robots using an integrated Delta manipulator by extruding a shear-thinning, structurally viable cementitious material to demonstrate the capability of the system using an external motion tracking environment. Apart from aerial robots with an integrated Delta manipulator, which is the main contribution towards the primary challenges from the author, other relevant enabling technologies include cementitious material technologies that manages the trade-offs between buildability and workability to make AAM possible within the constraints of aerial robotic platform, high-level planning and coordination algorithm for robotic construction agents and, finally, exploratory research of interlink between suitable printed structures and deposition trajectory for the robotic construction agents are discussed.

Apart from the primary challenges, secondary challenges that limit UAV utilisation in AAM and other real-world applications are also investigated. For environment, chapter 3 discusses

the Rotorigami project that explores a concept of physical protection against impact with the environments. Rotorigami has shown to reduce the collision force experienced by test aerial platform during impact and decouple the yawing moment arising from impacts. The current prototype has been designed for small UAVs as a first proof of concept towards origami-based aerial robots that can perform contact-based flight and manufacturing tasks. Even though the impact protection capability has been validated, more detailed dynamic and aerodynamic studies are needed for further development and evaluation of this concept. Further development of UAVs protection concepts could utilise this finding and build upon it to achieve better protection strategies for UAVs in different applications.

Chapter 4 discusses bioinspired landing system for aerial robots focusing on impact protection from dynamic landing. It utilises a bioinspired adaptive landing mechanism that allows compliant morphing to various examples of structures and terrains. Demonstrations show successful dynamic landings on diverse static terrains. The tests clearly demonstrate reduced impact forces experienced by the UAV test platform.

Chapter 5 discusses tensile-based perching and stabilising system which has been developed as an enabling technology towards improving UAVs endurance and low power aerial positioning. Two operation modes have been developed with the first being the stationary holding mode that allows extended operation time with the perching module and the second being the enhanced stability mode that can improves aerial stabilisation using tensile elements.

7.2 Technological Assessment

AAM has been demonstrated with aerial robots, but rather than being the only solution for enabling technology for automation in construction industry, it is more beneficial to place it as a part of a bigger robotic ecosystem for construction. This is because ground robots, in general, are more energy efficient in manipulating a given payload compared to aerial robots. Aerial robots should be used only in applications where they offer clear-cut extra advantages, such as in scenarios that require a large building envelope, in both horizontal and vertical directions. Such a system could also provide access to previously inaccessible locations if only ground-based agents are used alone. In other scenarios, such as construction projects with unrestricted and easily accessible road, rail and maritime shipping networks, off-site prefabrication methods may be more suitable. However, quantitative analysis should be performed to select appropriate construction methods, not just from anecdotal evidence. Many performance criteria have been suggested in the literature, but they can be categorised into seven dimensions: long term cost, constructability, quality, first cost, impact on health and community, architectural impact and environmental impact [151]. To my best knowledge, studies on performance criteria comparison of additive manufacturing techniques and other construction methods has yet to be published in the research community.

Nevertheless, AAM has been achieved for the first time and contributed to the field of aerial manufacturing. Setting aside the achievements, multiple technical issues has been observed from the AAM demonstration. External motion tracking system, which is not suitable for outdoor applications, is the only method that can provide localisation data with adequate accuracy, and therefore poses constraints on the size of the build envelope and environmental conditions. To this end, a new controller that relies on a combined system of VI-sensor-based SLAM framework and RTK-GPS for localisation is being developed by Aerial ABM members.

Another key performance criteria for AAM is the printing speed of the aerial construction agent but there are various factors that come into play, such as workability of the cementitious material, extrusion force of the extrusion mechanism and payload capacity of the aerial robot. A capability to print at higher speed is desirable but blindly increasing the printing speed may lead to a reduction of printing accuracy and higher stress in the mechanical structure of the extrusion mechanism. It may also involve the need to use to a much more powerful and possibly much heavier extrusion actuator that will reduce the flight time of the aerial construction agent.

In terms of logistics of the process, printable material quantity per flight is low, and frequent material cartridge swapping is inescapable. Refilling process is complex and susceptible to human error. Only a proof of concept with humans in the loop for supervision and intervention duty has been demonstrated so far.

Regarding other primary challenges, high-level planning and coordination algorithm has been

designed but has yet to be implemented with multiple robotic construction agents, however, the simpler version of that planning and coordination algorithm has been used with a single robotic construction agent as an early stage system verification test. Material technology has been developed in accordance to capabilities of the current design of Aerial ABM UAV platform, but further research is needed to gain more understanding between the material technology and the associated constraints.

Future aerial ABM UAV design iterations can be designed based on issues encountered in this project, such as buildability-workability trade-off and material extrusion timing control, to accommodate application requirements more effectively. For the structure and design challenge, further research should focus on what is the best way to effectively utilise the capabilities of the aerial construction agents and material behaviour for various requirements.

Apart from cementitious materials, expanding PU foam could be a suitable amorphous construction and repair material, with four possible usages anticipated: traditional insulation material, aerial repair sealing material, structural material and formwork material. Its characteristics as an aerial repair sealing material have been discussed in chapter 2, and its suitability for structural and formwork purposes has been suggested in the literature [149, 7].

Several concepts are investigated as part of secondary challenges in AAM. Rotorigami shows promising results and capabilities, but more research and development are required before utilising this concept on aerial construction agents or other UAVs.

Bioinspired landing system has potential to benefit general UAV applications and AAM. Ability to land and attach on various structure can be of particular interest when high fidelity flight control is not possible. However, this requires the landing mechanism to be part of the payload, which can shorten the flight time. Better designs that are optimised for specific applications can be more beneficial.

SpiderMAV can be further developed to enable low power tensile-flight hybrid locomotion which could tremendously benefit AAM in terms of energy efficiency, but the risk involved from combining tensile structure with rotating propellers must be accounted for in future design iterations.

7.3 Future Pathways

Considering achievements so far, the author suggests the following research plan for future development.

- The material refilling process, which is both tedious and error-prone, should be automated to eliminate this bottleneck in the AAM operation.
- The newly developed Multi-AAM, currently utilising only aerial robots, should be able to cope with multi-domain robot teams, especially with ground-based construction agents. Such a capacity will enable more effective construction processes.
- Although work has begun on real-time immersive virtual reality for construction progress monitoring and visualisation by Aerial ABM, it is necessary to stress its crucial role here. As the whole process becoming more autonomous and less independent on human operators, the planning algorithm must precisely know the up-to-date, or even real-time, construction progress in order to issue commands effectively. Failing to do so will possibly prevent large scale implementations to be effective.
- Precise outdoor localisation for aerial robots remains an important challenge, not just for AAM, but for any other applications that require such a high precision. A challenge would involve a localisation system thats accurate enough, not too heavy to carry on robots and not too computationally expensive.
- It appears that enabling technologies for AAM can influence and pose constraints on one another. Effort should be put in material technology and structural design research so that it can react quick enough to rapidly changing technological demands.
- A UAV platform is inherently power hungry because it requires constant propulsion to stay aloft. Together with the current low energy density battery technology, it only leads to unsatisfactory flight time and energy efficiency. There will not be a panacea for this problem, but there are a few possible mitigation measures. Concept behind SpiderMAV has potential to enable low-power tensile-aerial hybrid locomotion that aerial construction agents can utilise in some suitable scenarios. Bioinspired landing system enables adaptive landing mechanism that can morph and land on various structures, allowing aerial construction agents to effectively complete required tasks. In a way, adapting UAV platform to its working environments may offer competitive advantages over traditional commercial UAVs in some scenarios.
- Safety is an important concern with a UAV platform. This thesis focuses on the development of Rotorigami as an impact protection structure, however, there are many

unexplored approaches that could benefit differently for different applications. A more goal-oriented approach for protection system design would be more effective for real-world applications. Rather than aiming to be a solution for a general problem, such a process would start with the specific environmental requirements and directly tackle them with relevant design information.

- As the technologies move towards real-world implementations, any system deployments must be thoroughly evaluated in various dimensions - safety, reliability, cost and environmental impacts to name a few. Standardised tests and evaluation schemes should be developed, agreed and adopted by researchers and authorities alike.

With the above research plan, future demonstrations are expected to complete tasks that provide further insights into its feasibility and practicality. AAM with precise outdoor localisation and multiple construction agents should be targeted for the next demonstrations to prove its functionality in outdoor environments. Collaboration with ground-based construction agents should follow to demonstrate abilities to incorporate and utilise multi-domain robots. Suitable performance criteria should be evaluated to help in further development and in determining its appropriateness for real-world system deployment.

7.3.1 Summary of author's contribution

The development of precise aerial construction revolves around several enabling technologies and their implementation into practical robotic systems:

1. Aerial robotic stabilisation mechanisms for precise additive manufacturing.
2. Origami-based structural elements for aerial robotic navigation in challenging environments.
3. Tensile anchoring methods for aerial robots low-power operation.

To realise these enabling technologies, several innovations have been made:

1. UAV platform mechatronics design and development for AAM and aerial repair.
2. Self-aligning algorithm of the integrated aerial delta manipulator for AAM and aerial repair.
3. Software framework design and implementation in ROS which enable low latency communication and tasks execution for AAM and aerial repair.
4. Mechatronics design and development of aerial-based extrusion mechanisms.
5. Mechanical protection structure design and development for Rotorigami.
6. Onboard sensor and datalogging system design and development for Rotorigami collision test setup.
7. Mechatronics design and development for SpiderMAV.
8. Controller design and development for SpiderMAV.
9. Mechatronics design and development for bioinspired landing mechanisms.
10. Controller design and development for bioinspired landing mechanisms.
11. Onboard sensor and datalogging system design and development for bioinspired landing mechanisms.

The development of such technologies offers insights into multidisciplinary research required for aerial additive manufacturing, its challenges further ahead and various approaches towards future aerial robotic technology.

Bibliography

[1] P. Chermprayong, K. Zhang, F. Xiao, and M. Kovac, "An integrated delta manipulator for aerial repair: A new aerial robotic system," *IEEE Robotics Automation Magazine*, vol. 26, pp. 54–66, Mar 2019.

[2] P. Sareh, P. Chermprayong, M. Emmanuelli, H. Nadeem, and M. Kovac, "Rotorigami: A rotary origami protective system for robotic rotorcraft," *Science Robotics*, vol. 3, p. eaah5228, Sep 26, 2018.

[3] P. Sareh, P. Chermprayong, M. Emmanuelli, H. Nadeem, and M. Kovac, "The spinning cyclic miura-oring for mechanical collision-resilience," (Oxford, UK), pp. 981–994, 5 to 7 September 2018.

[4] P. Sareh and M. Kovac, "Aerial devices capable of controlled flight."

[5] K. Zhang, P. Chermprayong, D. Tzoumanikas, W. Li, M. Grimm, M. Smentoch, S. Leutenegger, and M. Kovac, "Bioinspired design of a landing system with soft shock absorbers for autonomous aerial robots," *Journal of Field Robotics*, vol. 36, pp. 230–251, Jan 2019.

[6] K. Zhang, P. Chermprayong, T. M. Alhinai, R. Siddall, and M. Kovac, "Spidermav: Perching and stabilizing micro aerial vehicles with bio-inspired tensile anchoring systems," pp. 6849–6854, IEEE, Sep 2017.

[7] S. J. Keating, J. C. Leland, L. Cai, and N. Oxman, "Toward site-specific and self-sufficient robotic fabrication on architectural scales," *Science Robotics*, vol. 2, no. 5, p. eaam8986, 2017.

[8] "Reinventing construction: A route to higher productivity," tech. rep., February 2017.

[9] S. Lim, R. A. Buswell, T. T. Le, S. A. Austin, A. G. F. Gibb, and T. Thorpe, "Developments in construction-scale additive manufacturing processes," *Automation in Construction*, vol. 21, pp. 262–268, 2012.

[10] D. D. Camacho, P. Clayton, W. O'Brien, R. Ferron, and S. Salamone, *Applications of additive manufacturing in the construction industry A forward-looking review*, vol. 89. 2018.

[11] P. Wu, J. Wang, and X. Wang, "A critical review of the use of 3-d printing in the construction industry," 2016. ID: 271427.

[12] I. Gibson, D. Rosen, and B. Stucker, *Additive manufacturing technologies*. New York, NY [u.a.]: Springer, 2. ed. ed., 2015.

[13] S. K. Joosten, "Printing a stainless steel bridge: An exploration of structural properties of stainless steel additive manufactures for civil engineering purposes," tech. rep., 2015.

[14] B. Khoshnevis, D. Hwang, K. T. Yao, and Z. Yeh, "Mega-scale fabrication by contour crafting," *International Journal of Industrial and Systems Engineering*, vol. 1, no. 3, p. 301, 2006.

[15] L. L. C. D-Shape Enterprises, "D-shape."

[16] Apis-Cor, "Apis-cor."

[17] L. Feng and L. yuhong, "Study on the status quo and problems of 3d printed buildings in china," *Global Journal of HUMAN-SOCIAL SCIENCE: H Interdisciplinary*, no. 5.

[18] "Totalkustom."

[19] F. Bos, R. Wolfs, Z. Ahmed, and T. Salet, "Additive manufacturing of concrete in construction: potentials and challenges of 3d concrete printing," *Virtual and Physical Prototyping*, vol. 11, pp. 209–225, Jul 2, 2016.

[20] C. Gosselin, R. Duballet, P. Roux, N. Gaudillire, J. Dirrenberger, and P. Morel, "Large-scale 3d printing of ultra-high performance concrete a new processing route for architects and builders," *Materials Design*, vol. 100, pp. 102–109, Jun 15, 2016.

[21] L. J. Love, "Utility of big area additive manufacturing (baam) for the rapid manufacture of customized electric vehicles," tech. rep., 2014.

[22] "Kamermaker."

[23] J. B. Gardiner, S. Janssen, and N. Kirchner, "A realisation of a construction scale robotic system for 3d printing of complex formwork," vol. 33, (Waterloo), p. 1, IAARC Publications, Jan 1, 2016.

[24] "Cybe."

[25] "Wasp."

[26] "Minibuilders."

[27] X. Zhang, M. Li, J. H. Lim, Y. Weng, Y. W. D. Tay, H. Pham, and Q.-C. Pham, "Large-scale 3d printing by a team of mobile robots," *Automation in Construction*, vol. 95, pp. 98–106, Nov 2018.

[28] A. Bicchi and W. Burgard, *Robotics Research : Volume 1*, vol. 2. Cham: Springer, Jul 25, 2017.

[29] "Watch brick-carrying drones build a tower together."

[30] G. Hunt, F. Mitzalis, T. Alhinai, P. A. Hooper, and M. Kovac, "3d printing with flying robots," in *Robotics and Automation (ICRA), 2014 IEEE International Conference on*, pp. 4493–4499, IEEE, 2014.

[31] D. D. Ekaso, *ACCURACY ASSESSMENT OF REAL-TIME KINEMATICS(RTK) MEASUREMENT ON UNMANNED AERIAL VEHICLES (UAV) FOR DIRECT GEO-REFERENCING*. PhD thesis.

[32] K. H. Petersen, N. Napp, R. Stuart-Smith, D. Rus, and M. Kovac, "A review of collective robotic construction," *Science Robotics*, vol. 4, p. eaau8479, Mar 13, 2019.

[33] D. Axinte, X. Dong, D. Palmer, A. Rushworth, S. C. Guzman, A. Olarra, I. Arizaga, E. Gomez-Acedo, K. Txoperena, K. Pfeiffer, *et al.*, "Mirorminiaturized robotic systems for holistic in-situ repair and maintenance works in restrained and hazardous environments," *IEEE/ASME Transactions on Mechatronics*, vol. 23, no. 2, pp. 978–981, 2018.

[34] M. Orsag, C. Korpela, and P. Oh, "Modeling and control of mm-uav: Mobile manipulating unmanned aerial vehicle," *Journal of Intelligent & Robotic Systems*, pp. 1–14, 2013.

[35] F. Ruggiero, M. A. Trujillo, R. Cano, H. Ascorbe, A. Viguria, C. Peréz, V. Lippiello, A. Ollero, and B. Siciliano, "A multilayer control for multirotor uavs equipped with a servo robot arm," in *Robotics and Automation (ICRA), 2015 IEEE International Conference on*, pp. 4014–4020, IEEE, 2015.

[36] S. Moe, G. Antonelli, A. R. Teel, K. Y. Pettersen, and J. Schrimpf, "Set-based tasks within the singularity-robust multiple task-priority inverse kinematics framework: General formulation, stability analysis, and experimental results," *Frontiers in Robotics and AI*, vol. 3, p. 16, 2016.

[37] G. Muscio, F. Pierri, M. A. Trujillo, E. Cataldi, G. Antonelli, F. Caccavale, A. Viguria, S. Chiaverini, and A. Ollero, "Coordinated control of aerial robotic manipulators: Theory and experiments," *IEEE Transactions on Control Systems Technology*, pp. 1–8, 2017.

[38] D. Mellinger, Q. Lindsey, M. Shomin, and V. Kumar, "Design, modeling, estimation and control for aerial grasping and manipulation," in *2011 IEEE/RSJ International Conference on Intelligent Robots and Systems*, pp. 2668–2673, IEEE, 2011.

[39] P. E. I. Pounds, D. R. Bersak, and A. M. Dollar, "The yale aerial manipulator: Grasping in flight," in *2011 IEEE International Conference on Robotics and Automation*, pp. 2974–2975, 2011.

[40] J. Thomas, G. Loianno, J. Polin, K. Sreenath, and V. Kumar, "Toward autonomous avian-inspired grasping for micro aerial vehicles," *Bioinspiration & biomimetics*, vol. 9, no. 2, p. 025010, 2014.

[41] D. Mellinger, M. Shomin, N. Michael, and V. Kumar, "Cooperative grasping and transport using multiple quadrotors," in *Distributed autonomous robotic systems*, pp. 545–558, Springer, 2013.

[42] K. Baizid, G. Giglio, F. Pierri, M. A. Trujillo, G. Antonelli, F. Caccavale, A. Viguria, S. Chiaverini, and A. Ollero, "Experiments on behavioral coordinated control of an unmanned aerial vehicle manipulator system," in *Robotics and Automation (ICRA), 2015 IEEE International Conference on*, pp. 4680–4685, IEEE, 2015.

[43] M. Orsag, C. Korpela, S. Bogdan, and P. Oh, "Valve turning using a dual-arm aerial manipulator," in *Unmanned Aircraft Systems (ICUAS), 2014 International Conference on*, pp. 836–841, IEEE, 2014.

[44] S. Kim, S. Choi, and H. J. Kim, "Aerial manipulation using a quadrotor with a two dof robotic arm," in *Intelligent Robots and Systems (IROS), 2013 IEEE/RSJ International Conference on*, pp. 4990–4995, IEEE, 2013.

[45] C. Gosselin and J. Angeles, "The optimum kinematic design of a spherical three-degree-of-freedom parallel manipulator," *Journal of mechanisms, transmissions, and automation in design*, vol. 111, no. 2, pp. 202–207, 1989.

[46] J.-P. Merlet, *Parallel robots*, vol. 128. Springer Science & Business Media, 2006.

[47] A. Hernández, O. Altuzarra, O. Salgado, C. Pinto, and V. Petuya, "Designing parallel manipulators: from specifications to a real prototype," *Industrial Robot: An International Journal*, vol. 39, no. 5, pp. 500–512, 2012.

[48] R. Cano, C. Pérez, F. Pruano, A. Ollero, and G. Heredia, "Mechanical design of a 6-dof aerial manipulator for assembling bar structures using uavs," in *2nd RED-UAS 2013 workshop on research, education and development of unmanned aerial systems*, 2013.

[49] "Drones that fix pipeline leaks win international acclaim." https://www.imperial.ac.uk/news/170806/drones-that-pipeline-leaks-international-acclaim/. Accessed: 2018-02-10.

[50] F. Pierrot, C. Reynaud, and A. Fournier, "Delta: a simple and efficient parallel robot," *Robotica*, vol. 8, no. 2, pp. 105–109, 1990.

[51] S. Staicu and D. C. Carp-Ciocardia, "Dynamic analysis of clavel's delta parallel robot," in *2003 IEEE International Conference on Robotics and Automation (Cat. No.03CH37422)*, vol. 3, pp. 4116–4121, Sept 2003.

[52] X. Yang, Z. Feng, C. Liu, and X. Ren, "A geometric method for kinematics of delta robot and its path tracking control," in *Control, Automation and Systems (ICCAS), 2014 14th International Conference on*, pp. 509–514, IEEE, 2014.

[53] "Delta robot kinematics." http://hypertriangle.com/ alex/delta-robot-tutorial/. Accessed: 2017-09-10.

[54] I. Sa, M. Kamel, R. Khanna, M. Popovic, J. Nieto, and R. Siegwart, "Dynamic system identification, and control for a cost effective open-source vtol mav," *arXiv preprint arXiv:1701.08623*, 2017.

[55] S. Lynen, M. Achtelik, S. Weiss, M. Chli, and R. Siegwart, "A robust and modular multi-sensor fusion approach applied to mav navigation," in *Proc. of the IEEE/RSJ Conference on Intelligent Robots and Systems (IROS)*, 2013.

[56] T. Schneider, M. T. Dymczyk, M. Fehr, K. Egger, S. Lynen, I. Gilitschenski, and R. Siegwart, "maplab: An open framework for research in visual-inertial mapping and localization," *IEEE Robotics and Automation Letters*, 2018.

[57] "ar_track_alvar - ROS Wiki."

[58] "Robotis git." https://github.com/ROBOTIS-GIT/. Accessed: 2018-02-10.

[59] "Ld40 polyurethane - hard foam." http://www.mbfg.co.uk/foam-materials/foam-hard.html/. Accessed: 2018-02-10.

[60] J. Alonso-Mora, T. Naegeli, R. Siegwart, and P. Beardsley, "Collision avoidance for aerial vehicles in multi-agent scenarios," *Autonomous Robots*, vol. 39, no. 1, pp. 101–121, 2015. ID: Alonso-Mora2015.

[61] X. Wang, V. Yadav, and S. N. Balakrishnan, "Cooperative uav formation flying with obstacle/collision avoidance," *IEEE Transactions on Control Systems Technology*, vol. 15, no. 4, pp. 672–679, 2007. ID: 1.

[62] H. Durrant-Whyte, N. Roy, and P. Abbeel, *Unmanned Aircraft Collision Avoidance Using Continuous-State POMDPs*. 2012. ID: 1.

[63] M. D. T., "Issues concerning integration of unmanned aerial vehicles in civil airspacenbsp;," tech. rep., November 2014.

[64] S. Temizer, M. Kochenderfer, L. Kaelbling, T. Lozano-Perez, and J. Kuchar, *Collision Avoidance for Unmanned Aircraft using Markov Decision Processes**. AIAA Guidance, Navigation, and Control Conference, American Institute of Aeronautics and Astronautics, 2010. 14; M1: 0; doi:10.2514/6.2010-8040.

[65] A. Briod, A. Klaptocz, J. Zufferey, and D. Floreano, "The airburr: A flying robot that can exploit collisions," in *2012 ICME International Conference on Complex Medical Engineering (CME)*, pp. 569–574, 2012. ID: 1.

[66] M. Kovac, M. Schlegel, J. Zufferey, and D. Floreano, "A miniature jumping robot with self-recovery capabilities," in *2009 IEEE/RSJ International Conference on Intelligent Robots and Systems*, pp. 583–588, 2009. ID: 1.

[67] M. Kovač, "The bioinspiration design paradigm: A perspective for soft robotics," *Soft Robotics*, vol. 1, no. 1, pp. 28–37, 2014.

[68] T. Bartelds, A. Capra, S. Hamaza, S. Stramigioli, and M. Fumagalli, "Compliant aerial manipulators: Toward a new generation of aerial robotic workers," *IEEE Robotics and Automation Letters*, vol. 1, no. 1, pp. 477–483, 2016. ID: 1.

[69] Y. Mulgaonkar, T. Kientz, M. Whitzer, and V. Kumar, "Design and fabrication of safe, light-weight, flying robots; international design engineering technical conferences and computers and information in engineering conference," 2015. 10.1115/DETC2015-47864.

[70] P. M. Kornatowski, S. Mintchev, and D. Floreano, "An origami-inspired cargo drone," in *2017 IEEE/RSJ International Conference on Intelligent Robots and Systems (IROS)*, pp. 6855–6862, 2017. ID: 1.

[71] J. Stowers, M. Hayes, and A. Bainbridge-Smith, "Biologically inspired uav obstacle avoidance and control using monocular optical flow divergence templates," in *The 5th International Conference on Automation, Robotics and Applications*, pp. 378–383, 2011. ID: 1.

[72] C. M. Paul, D.-J. Lee, and R. W. Beard, "Obstacle avoidance for unmanned air vehicles using optical flow probability distributions," vol. 5609, 12/29 2004.

[73] W. E. Green and P. Y. Oh, "Optic-flow-based collision avoidance," *IEEE Robotics Automation Magazine*, vol. 15, no. 1, pp. 96–103, 2008. ID: 1.

[74] Y. K. Kwag and C. H. Chung, "Uav based collision avoidance radar sensor," in *2007 IEEE International Geoscience and Remote Sensing Symposium*, pp. 639–642, 2007. ID: 1.

[75] R. J. Fontana, E. A. Richley, A. J. Marzullo, L. C. Beard, R. W. T. Mulloy, and E. J. Knight, "An ultra wideband radar for micro air vehicle applications," in *2002 IEEE Conference on Ultra Wideband Systems and Technologies (IEEE Cat. No.02EX580)*, pp. 187–191, 2002. ID: 1.

[76] R. Sabatini, M. A. Richardson, and E. Roviaro, "Development and flight test of an avionics lidar for helicopter and uav low-level flight," 2013.

[77] S. Weiss, D. Scaramuzza, and R. Siegwart, "Monocular-slambased navigation for autonomous micro helicopters in gps-denied environments," *Journal of Field Robotics*, vol. 28, no. 6, pp. 854–874, 2011. doi: 10.1002/rob.20412; 14.

[78] M. W. Achtelik, S. Lynen, S. Weiss, L. Kneip, M. Chli, and R. Siegwart, "Visual-inertial slam for a small helicopter in large outdoor environments," in *2012 IEEE/RSJ International Conference on Intelligent Robots and Systems*, pp. 2651–2652, 2012. ID: 1.

[79] S. Leutenegger, S. Lynen, M. Bosse, R. Siegwart, and P. Furgale, "Keyframe-based visual–inertial odometry using nonlinear optimization," *The International Journal of Robotics Research*, p. 0278364914554813, 2014.

[80] "Phantom 4 series propeller guards."

[81] T. Krajnk, V. Vonsek, D. Fier, and J. Faigl, "Ar-drone as a platform for robotic research and education," in *Research and Education in Robotics - EUROBOT 2011* (D. Obdrlek and A. Gottscheber, eds.), (Berlin, Heidelberg), pp. 172–186, Springer Berlin Heidelberg, 2011. ID: 10.1007/978-3-642-21975-$7_1$6.

[82] L. J. Gibson and M. F. Ashby, *Cellular solids.* Cambridge [u.a.]: Cambridge Univ. Press, 2. ed., 1. paperback ed. (with corr.) ed., 1999.

[83] S. Mcvicker, "Shear wall basics."

[84] C. Lv, D. Krishnaraju, G. Konjevod, H. Yu, and H. Jiang, "Origami based mechanical metamaterials," *Scientific Reports*, vol. 4, p. 5979, 2014.

[85] J. T. B. Overvelde, T. A. de Jong, Y. Shevchenko, S. A. Becerra, G. M. Whitesides, J. C. Weaver, C. Hoberman, and K. Bertoldi, "A three-dimensional actuated origami-inspired transformable metamaterial with multiple degrees of freedom," *Nature Communications*, vol. 7, p. 10929, 2016.

[86] J. Song, Y. Chen, and G. Lu, "Axial crushing of thin-walled structures with origami patterns," 2012. ID: 271493.

[87] C. C. Min and H. Suzuki, "Geometrical properties of paper spring," in *Manufacturing Systems and Technologies for the New Frontier* (M. Mitsuishi, K. Ueda, and F. Kimura, eds.), (London), pp. 159–162, Springer London, 2008. ID: 10.1007/978-1-84800-267-$8_3$2.

[88] J. Ma and Z. You, "Energy absorption of thin-walled square tubes with a prefolded origami patternpart i: geometry and numerical simulation," *Journal of Applied Mechanics*, vol. 81, no. 1, p. 011003, 2014.

[89] M. Ranjbaran and K. Khorasani, "Fault recovery of an under-actuated quadrotor aerial vehicle," in *49th IEEE Conference on Decision and Control (CDC)*, pp. 4385–4392, 2010. ID: 1.

[90] P. Sareh, P. Chermprayong, M. Emmanuelli, H. Nadeem, and M. Kovac, "The spinning cyclic miura-oring for mechanical collision-resilience," (Oxford, UK), pp. 981–994, 5 to 7 September 2018.

[91] K. Miura, *Map fold a La Miura style, its physical characteristics and application to the space science.* R. Takaki, Ed., 1994.

[92] K. Miura, "The science of miura-ori: A review," pp. 87–99, Pasadena, CA, USA, 8-10 September 2006 September 2006.

[93] P. Sareh, *Symmetric Descendants of the Miura-ori.* PhD thesis, 2014.

[94] K. Miura, "Method of packaging and deployment of large membranes in space," *The Institute of Space and Astronautical Science report*, vol. 618, pp. 1–9, Dec 1, 1985.

[95] "Lsm6 library for arduino."

[96] "Arduino fat16/fat32 library."

[97] D. Floreano and R. J. Wood, "Science, technology and the future of small autonomous drones," *Nature*, vol. 521, no. 7553, pp. 460–466, 2015.

[98] A. Kalantari and M. Spenko, "Modeling and performance assessment of the hytaq, a hybrid terrestrial/aerial quadrotor," *IEEE Transactions on Robotics*, vol. 30, no. 5, pp. 1278–1285, 2014.

[99] K. Low, T. Hu, S. Mohammed, J. Tangorra, and M. Kovac, "Perspectives on biologically inspired hybrid and multi-modal locomotion," *Bioinspiration & biomimetics*, vol. 10, no. 2, p. 020301, 2015.

[100] A. Vidyasagar, J.-C. Zufferey, D. Floreano, and M. Kovač, "Performance analysis of jump-gliding locomotion for miniature robotics," *Bioinspiration & biomimetics*, vol. 10, no. 2, p. 025006, 2015.

[101] M. Kovač, M. Schlegel, J.-C. Zufferey, and D. Floreano, "Steerable miniature jumping robot," *Autonomous Robots*, vol. 28, no. 3, pp. 295–306, 2010.

[102] M. T. Pope, C. W. Kimes, H. Jiang, E. W. Hawkes, M. A. Estrada, C. F. Kerst, W. R. Roderick, A. K. Han, D. L. Christensen, and M. R. Cutkosky, "A multimodal robot for perching and climbing on vertical outdoor surfaces," *IEEE Transactions on Robotics*, vol. 33, no. 1, pp. 38–48, 2017.

[103] M. A. Estrada, E. W. Hawkes, D. L. Christensen, and M. R. Cutkosky, "Perching and vertical climbing: Design of a multimodal robot," in *Robotics and Automation (ICRA), 2014 IEEE International Conference on*, pp. 4215–4221, IEEE, 2014.

[104] J. D. Dickson and J. E. Clark, "Design of a multimodal climbing and gliding robotic platform," *IEEE/ASME Transactions On Mechatronics*, vol. 18, no. 2, pp. 494–505, 2013.

[105] L. Daler, J. Lecoeur, P. B. Hählen, and D. Floreano, "A flying robot with adaptive morphology for multi-modal locomotion," in *Intelligent Robots and Systems (IROS), 2013 IEEE/RSJ International Conference on*, pp. 1361–1366, IEEE, 2013.

[106] 2015. URL: https://www.dji.com/matrice100/features.

[107] E. Culler, G. Thomas, and C. Lee, "A perching landing gear for a quadcopter," in *53rd AIAA/ASME/ASCE/AHS/ASC Structures, Structural Dynamics and Materials Conference*, p. 1722, 2012.

[108] C. E. Doyle, J. J. Bird, T. A. Isom, J. C. Kallman, D. F. Bareiss, D. J. Dunlop, R. J. King, J. J. Abbott, and M. A. Minor, "An avian-inspired passive mechanism for quadrotor perching," *IEEE/ASME Transactions on Mechatronics*, vol. 18, no. 2, pp. 506–517, 2013.

[109] M. Tieu, D. M. Michael, J. B. Pflueger, M. S. Sethi, K. N. Shimazu, T. M. Anthony, and C. L. Lee, "Demonstrations of bio-inspired perching landing gear for uavs," in *Bioinspiration, Biomimetics, and Bioreplication 2016*, vol. 9797, p. 97970X, International Society for Optics and Photonics, 2016.

[110] M. L. Burroughs, K. B. Freckleton, J. J. Abbott, and M. A. Minor, "A sarrus-based passive mechanism for rotorcraft perching," *Journal of Mechanisms and Robotics*, vol. 8, no. 1, p. 011010, 2016.

[111] C. Luo, X. Li, Y. Li, and Q. Dai, "Biomimetic design for unmanned aerial vehicle safe landing in hazardous terrain," *IEEE/ASME Transactions on Mechatronics*, vol. 21, no. 1, pp. 531–541, 2016.

[112] S. S. Tolman, I. L. Delimont, L. L. Howell, and D. T. Fullwood, "Material selection for elastic energy absorption in origami-inspired compliant corrugations," *Smart Materials and Structures*, vol. 23, no. 9, p. 094010, 2014.

[113] J. Ma, D. Hou, Y. Chen, and Z. You, "Quasi-static axial crushing of thin-walled tubes with a kite-shape rigid origami pattern: Numerical simulation," *Thin-Walled Structures*, vol. 100, pp. 38–47, 2016.

[114] J. Song, Y. Chen, and G. Lu, "Axial crushing of thin-walled structures with origami patterns," *Thin-Walled Structures*, vol. 54, pp. 65–71, 2012.

[115] A. M. Dollar, K.-J. Cho, R. S. Fearing, and Y.-L. Park, "Special issue: Fabrication of fully integrated robotic mechanisms," *Journal of Mechanisms and Robotics*, vol. 7, no. 2, p. 020201, 2015.

[116] K. Kuribayashi, K. Tsuchiya, Z. You, D. Tomus, M. Umemoto, T. Ito, and M. Sasaki, "Self-deployable origami stent grafts as a biomedical application of ni-rich tini shape memory alloy foil," *Materials Science and Engineering: A*, vol. 419, no. 1, pp. 131–137, 2006.

[117] K. Zhang, C. Qiu, and J. S. Dai, "Helical kirigami-enabled centimeter-scale worm robot with shape-memory-alloy linear actuators," *Journal of Mechanisms and Robotics*, vol. 7, no. 2, p. 021014, 2015.

[118] B. Bhushan, "Biomimetics: lessons from nature–an overview," 2009.

[119] M. Kovač, "Learning from nature how to land aerial robots," *Science*, vol. 352, no. 6288, pp. 895–896, 2016.

[120] R. J. Manzanera and S. Smith, "Flight in nature ii: How animal flyers land," *The Aeronautical Journal*, vol. 119, no. 1213, pp. 281–299, 2015.

[121] H. Liu, S. Ravi, D. Kolomenskiy, and H. Tanaka, "Biomechanics and biomimetics in insect-inspired flight systems," *Phil. Trans. R. Soc. B*, vol. 371, no. 1704, p. 20150390, 2016.

[122] W. R. Roderick, M. R. Cutkosky, and D. Lentink, "Touchdown to take-off: at the interface of flight and surface locomotion," *Interface focus*, vol. 7, no. 1, p. 20160094, 2017.

[123] 2017. URL: https://www.mbzirc.com/.

[124] R. MacCurdy, J. Lipton, S. Li, and D. Rus, "Printable programmable viscoelastic materials for robots," in *Intelligent Robots and Systems (IROS), 2016 IEEE/RSJ International Conference on*, pp. 2628–2635, IEEE, 2016.

[125] R. MacCurdy, R. Katzschmann, Y. Kim, and D. Rus, "Printable hydraulics: a method for fabricating robots by 3d co-printing solids and liquids," in *Robotics and Automation (ICRA), 2016 IEEE International Conference On*, pp. 3878–3885, IEEE, 2016.

[126] 2016. URL: https://markforged.com/materials/.

[127] 2017. URL: https://ultimaker.com/en/products/materials/tpu-95a.

[128] R. Mur-Artal and J. D. Tardós, "Orb-slam2: An open-source slam system for monocular, stereo, and rgb-d cameras," *IEEE Transactions on Robotics*, 2017.

[129] A. Briod, P. Kornatowski, J.-C. Zufferey, and D. Floreano, "A collision-resilient flying robot," *Journal of Field Robotics*, vol. 31, no. 4, pp. 496–509, 2014.

[130] M. Kovac, "Learning from nature how to land aerial robots," *Science*, vol. 352, no. 6288, pp. 895–896, 2016.

[131] M. Anderson, *The Sticky-Pad Plane and Other Innovative Concepts for Perching UAVs*. 47th AIAA Aerospace Sciences Meeting including The New Horizons Forum and Aerospace Exposition, American Institute of Aeronautics and Astronautics, 2009. 14; M1: 0; doi:10.2514/6.2009-40.

[132] A. Kalantari, K. Mahajan, D. Ruffatto, and M. Spenko, "Autonomous perching and take-off on vertical walls for a quadrotor micro air vehicle," in *2015 IEEE International Conference on Robotics and Automation (ICRA)*, pp. 4669–4674, 2015. ID: 1.

[133] E. W. Hawkes, H. Jiang, and M. R. Cutkosky, "Three-dimensional dynamic surface grasping with dry adhesion," *The International Journal of Robotics Research*, vol. 35, no. 8, pp. 943–958, 2016. doi: 10.1177/0278364915584645; 14.

[134] A. L. Desbiens, A. T. Asbeck, and M. R. Cutkosky, "Landing, perching and taking off from vertical surfaces," *The International Journal of Robotics Research*, vol. 30, no. 3, pp. 355–370, 2011. doi: 10.1177/0278364910393286; 14.

[135] P. Xie, O. Ma, and Z. Zhang, "A bio-inspired approach for uav landing and perching," in *Proc. AIAA GNC*, vol. 13, 2013.

[136] M. Kova, J. Germann, C. Hrzeler, R. Y. Siegwart, and D. Floreano, "A perching mechanism for micro aerial vehicles," *Journal of Micro-Nano Mechatronics*, vol. 5, no. 3, pp. 77–91, 2009. ID: Kova2009.

[137] M. Kovac, Wassim-Hraiz, O. Fauria, J. Zufferey, and D. Floreano, "The locomotion capabilities of the epfl jumpglider: A hybrid jumping and gliding robot," in *2011 IEEE International Conference on Robotics and Biomimetics*, pp. 2249–2250, 2011. ID: 1.

[138] P.-J. Bristeau, F. Callou, D. Vissire, and N. Petit, "The navigation and control technology inside the ar.drone micro uav," 2011. ID: 314898.

[139] V. MUKHOPADHYAY and J. R. NEWSOM, "A multiloop system stability margin study using matrix singular values," *Journal of Guidance, Control, and Dynamics*, vol. 7, no. 5, pp. 582–587, 1984. doi: 10.2514/3.19898; 14.

[140] B. Herisse, F. Russotto, T. Hamel, and R. Mahony, "Hovering flight and vertical landing control of a vtol unmanned aerial vehicle using optical flow," in *2008 IEEE/RSJ International Conference on Intelligent Robots and Systems*, pp. 801–806, 2008. ID: 1.

[141] H. A. Izadi, Y. Zhang, and B. W. Gordon, "Fault tolerant model predictive control of quad-rotor helicopters with actuator fault estimation," 2011. ID: 314898.

[142] A. Freddi, A. Lanzon, and S. Longhi, "A feedback linearization approach to fault tolerance in quadrotor vehicles," 2011. ID: 314898.

[143] M. W. Mueller and R. D'Andrea, "Stability and control of a quadrocopter despite the complete loss of one, two, or three propellers," in *2014 IEEE International Conference on Robotics and Automation (ICRA)*, pp. 45–52, 2014. ID: 1.

[144] J. A. C. Humphrey, "Fluid mechanic constraints on spider ballooning," *Oecologia*, vol. 73, no. 3, pp. 469–477, 1987. ID: Humphrey1987.

[145] T. Bruckmann and A. Pott, *Cable-driven parallel robots*, vol. 112. Heidelberg ; New York ; Dordrecht ; London: Springer, 2013.

[146] C. GOSSELIN, "Cable-driven parallel mechanisms: state of the art and perspectives," *Mechanical Engineering Reviews*, vol. 1, no. 1, p. DSM0004, 2014. TI:.

[147] B. Dams, S. Sareh, K. Zhang, P. Shepherd, M. Kovac, and R. Ball, "Aerial additive building manufacturing: three-dimensional printing of polymer structures using drones," Jun 13, 2017.

[148] B. Dams, Y. Wu, P. Shepherd, and R. Ball, "Aerial additive building manufacturing of 3d printed cementitious structures," Sep 12, 2017.

[149] B. Dams, J. Peng, P. Shepherd, and R. Ball, "Cementitious mortars and polyurethane foams for additive building manufacturing," Apr 9, 2018.

[150] A. Alarifi, A. Al-Salman, M. Alsaleh, A. Alnafessah, S. Al-Hadhrami, M. A. Al-Ammar, and H. S. Al-Khalifa, "Ultra wideband indoor positioning technologies: Analysis and recent advances," *Sensors (Basel, Switzerland)*, vol. 16, p. 707, May 16, 2016.

[151] Y. Chen, G. E. Okudan, and D. R. Riley, "Sustainable performance criteria for construction method selection in concrete buildings," *Automation in Construction*, vol. 19, no. 2, pp. 235–244, 2010.